Tracking phytoplankton from space in a changing Southern Ocean

Dissertation zur Erlangung des akademischen Grades
Doktor der Naturwissenschaften (Dr. rer. nat.)

vorgelegt dem Fachbereich 1 Physik der Universität Bremen

Erstgutachter: Prof. Dr. Astrid Bracher
Zweitgutachter: Prof. Dr. Reiner Schlitzer
Datum der Abgabe: 26.05.2015

Mariana Altenburg Soppa
geb. in Blumenau
2015

1st Reviewer: Prof. Dr. Astrid Bracher,
Institute of Environmental Physics, Universität Bremen,
Bremen and Alfred-Wegener-Institute for Polar and Marine
Research, Bremerhaven

2nd Reviewer: Prof. Dr. Reiner Schlitzer,
Alfred-Wegener-Institute for Polar and Marine Research,
Bremerhaven

Anlage zur Dissertation

Eidesstattliche Erklärung
(Erklärung gemäß § 5 Abs. 2 Nr.3 und § 7 Abs. 1 Nr. 2)

Hiermit versichere ich, dass ich
    1) die vorliegende Arbeit ohne unerlaubte, fremde Hilfe angefertigt habe
    2) keine anderen, als die von mir im Text angegebenen Quellen und Hilfsmittel benutzt habe
    3) die den benutzen Werken wörtlich oder inhaltlich entnommenen Stellen als solche
    kenntlich gemacht habe.

Bremen, 26.05.2015

_____
Mariana Altenburg Soppa

Valeu a pena? Tudo vale a pena se a alma não é pequena.

Was it worth it? Everything is worthy If the soul is not small.

Fernando Pessoa, Portuguese Sea, 1934

Acknowledgments

Table of Contents

Abstract

Changes in the Southern Ocean (SO) have global consequences. The SO region is responsible for about half of the global annual uptake of anthropogenic carbon dioxide (CO_2) from the atmosphere. As part of the atmospheric CO_2 uptake is driven by phytoplankton primary production, a significant impact on the feedback of phytoplankton is expected under climate change. Indeed, changes in the atmospheric and ocean temperature, wind patterns and sea ice concentration have already been documented in the SO region. However, our understanding on how phytoplankton respond to ongoing and future environmental changes strongly depends on consistent large scale and long term observations.

As a remote region, substantial time and costs are required to obtain a comprehensive dataset for the SO. The use of satellite remote sensing is a cost-effective alternative and has led to important insights into the current knowledge of phytoplankton dynamics in this region. However, this technique does not come without limitations. Ocean colour remote sensing at high latitudes has to deal with different issues as for example high cloudiness and the limited number of *in situ* observations for development and calibration/validation of algorithms. Consequently, there is a strong need to assess the performance of ocean colour derived-products in the SO.

Ocean colour remote sensing can be used to estimate net primary production (NPP), abundance of phytoplankton functional types (PFT), as well as their spatial and temporal dynamic. Although accurate information on NPP is fundamental, large differences have been observed among models hitherto applied in the SO. Apart from that, different PFTs play specific roles in the oceanic biogeochemical cycle and this information is of key importance on quantifying oceanic NPP. Diatoms, for instance, are the main primary producers in the region. Furthermore, additional insights into their variability due to environmental changes can be gained by studying the phenology of diatom blooms. The underlying aim of this thesis is to shed light into the above mentioned topics with a focus on the SO.

Four main objectives have been pursued: 1) to evaluate the satellite retrievals of euphotic depth (Z_{eu}) and how they influence NPP satellite retrievals; 2) to evaluate and improve the satellite retrievals of diatom abundance; 3) to investigate the mean patterns and interannual variability of diatom bloom phenology and 4) to examine the potential of ocean colour products to access environmental changes in the SO.

The first study analyses satellite retrievals of Z_{eu}, which is the lower limit of the euphotic zone and where most of the primary production takes place. Although the Z_{eu} is a key parameter in modelling oceanic NPP from satellite data, assessments of the uncertainties of satellite Z_{eu} products are scarce. This study investigated existing approaches and sensors to evaluate how different Z_{eu} products might affect the estimation of NPP in the SO. Z_{eu} was derived from MODIS and SeaWiFS products of (i) surface chlorophyll-a (Z_{eu}-Chla) and (ii) inherent optical properties (Z_{eu}-IOP). After comparison with *in situ* measurements, both approaches have shown robust results of Z_{eu} retrievals, but spatial differences were of up to 30% over specific regions. Differences between the sensors were less evident. It was also shown that differences larger than 30% are expected in NPP, depending on the method used to estimate Z_{eu}.

In the second study, focus is given to the major marine primary producer - the diatoms - and to

the importance of the SO in developing a global algorithm for the retrieval of diatom abundance using the Abundance Based Approach (ABA). A large global *in situ* dataset of phytoplankton pigments was compiled, particularly with more samples collected in the SO. The ABA was revised to account for the penetration depth (Z_{pd}) and to improve the relationship between diatoms and total chlorophyll-a (TChla). The results showed a distinct relationship between diatoms and TChla in the SO and a new global model (ABA_{Zpd}) was suggested to improve the estimation of diatoms abundance, which improved the uncertainties by 28% in the SO compared with the original ABA model. In addition, a regional model for the SO was developed which further improved the retrieval of diatoms by 17% compared with the global ABA_{Zpd} model. The main finding of this study is that diatom may be more abundant in the SO than previously thought.

In the third study, the new regional model was used to examine the mean pattern and the interannual variability of the diatom bloom phenology from 1997 to 2012. Ten phenological indices were used to describe the timing, duration and magnitude of the diatom blooms. The results show that the mean spatial patterns are generally associated to the position of the Southern Antarctic Circumpolar Current Front and of the maximum sea ice extent. Furthermore, in several areas of the SO the interannual variability of the anomalies of the phenological indices is found to be correlated with the large scale climate oscillations El Niño Southern Oscillation (ENSO) and Southern Annular Mode (SAM). The composite maps of the anomalies revealed distinct spatial patterns and opposite events of ENSO and SAM have similar effects in the diatom phenology. For example, in the Ross Sea region, later start of the bloom and lower biomass were observed associated with El Niño and negative SAM events; likely influenced by an increase in sea ice concentration during these events. These results confirm that climate variability and diatom blooms in the SO are closely linked through environmental changes and these processes can be accessed using ocean colour remote sensing.

List of Publications

This thesis is comprised of the following manuscripts:

Soppa, M. A., Dinter, T., Taylor, B., Bracher, A. (2013). Satellite derived euphotic depth in the Southern Ocean: implication for primary production modeling. *Remote Sensing of Environment*, 137, 198-211. doi:10.1016/j.rse.2013.06.017.

Soppa, M. A., Hirata, T., Silva, B., Dinter, T., Peeken, I., Wiegmann S., Bracher, A. (2014). Global retrieval of diatoms abundance based on phytoplankton pigments and satellite data. Remote Sensing. *Remote Sensing*, 6 (10), 10089-10106. doi:10.3390/rs61010089.

Soppa, M. A., Völker, C., Bracher, A. Mean and interannual variability of diatom blooms phenology in the Southern Ocean. To be submitted.

Other peer-reviewed manuscripts not included in the thesis:

Sadeghi, A., Dinter, T., Vountas, M., Taylor, B., Peeken, I., **Soppa**, M. A. and Bracher, A. (2012). Improvements to the PhytoDOAS method for identification of coccolithophores using hyperspectral satellite data. *Ocean Sciences*, 8 (6), 1055-1070.

Sadeghi, A., Dinter, T., Vountas, M., Taylor, B., **Soppa**, M. A. and Bracher, A. (2012). Remote sensing of coccolithophore blooms in selected oceanic regions using the PhytoDOAS method applied to hyper-spectral satellite data. *Biogeosciences*, 9 (6), pp. 2127-2143.

Brandt, A., Vanreusel, A., Bracher, A., Hoppe, C., Lins, L., Meyer-Löbbecke, A., **Soppa**, M. A., Würzberg, L. (2014). Are boundary conditions in surface productivity at the Southern Polar Front are reflected in benthic activity? *Deep-Sea Research Part II-Topical Studies in Oceanography*, 108, 51-59.

Hoppe, C. J. M., Ossebaar, S., **Soppa**, M. A., Cheah, W., Klaas, C., Rost, B., Wolf-Gladrow, D., Hoppema, M., Bracher, A., Strass, V., de Baar, H. J. W., Trimborn, S. Controls of primary production in two different phytoplankton blooms in the Antarctic Circumpolar Current. Submitted to *Deep-Sea Research Part II-Topical Studies in Oceanography*, May 2015.

List of Abbreviations

a	total absorption coefficient
a_{ph}	absorption coefficient of phytoplankton
a_w	absorption coefficient of pure seawater
b_b	total backscattering coefficient
b_{bw}	backscattering coefficient of pure seawater
AAIW	Antarctic Intermediate Water
AAO	Antarctic Oscillation index
ABA	Absorption Based Approach
ABA*	Original model of Hirata et al. (2011) parameterized with a new dataset
ABA**	Original model and fitting parameters of Hirata *et al.* (2011)
ABA_{Zpd}	Modified ABA model
ABPM	Absorption Based Primary Production Model
ACC	Antarctic Circumpolar Current
Allo	Alloxanthin
AOP	Apparent Optical Properties
AZ	Antarctic Zone
BD	Bloom Duration
BDD	Bloom Decline Duration
BED	Bloom End Date
BGD	Bloom Growth Duration
BSD	Bloom Start Date
Butfuco	19'-butanoyloxyfucoxanthin
CA	Dia-Chla Amplitude
CAV	Dia-Chla averaged over BGD
CCI	Climate Change Initiative
CDOM	Colored dissolved organic matter
Chla	Monovinyl chlorophyll-a plus chlorophyllid-a, allomers and epimers
Chlb	Monovinyl chlorophyll-b
Chlc	Monovinyl chlorophyll-c
CI	Dia-Chla integrated over BGD
CM	Dia-Chla Maximum
CMD	Date of Dia-Chla Maximum
Dia	Diatom
DOAS	Differential optical absorption spectroscopy method
DP	Concentration of the diagnostic pigments
DPA	Diagnostic Pigment Analysis
E	Average absolute percentage of error
Ed	Downwelling irradiance
ENSO	El Niño Southern Oscillation
ESA	European Space Agency

f-PFT	fraction of TChla attributed to a specific PFT
Fuco	Fucoxanthin
Hexfuco	19'-hexanoyloxyfucoxanthin
HNLC	High nutrient low chlorophyll
HPLC	High Performance Liquid Chromatography
IDW	Indian Deep Water
IOP	Inherent Optical Properties
ITF	Indonesian Throughflow
Kd	Attenuation coefficient
L	Radiance
LCDW	Lower Circumpolar Deep Water
MAE	Mean Absolute Error
MEI	Multivariate El Niño Southern Oscillation index
MERIS	Medium Resolution Imaging Spectrometer
MOC	Meridional overturning circulation
MODIS	Moderate Resolution Imaging Spectroradiometer
N	Number of data points/samples
NADW	North Atlantic Deep Water
NASA	National Aeronautics and Space Administration
nL_w	Normalized water leaving radiance
NPP	Net primary production
NSIDC	National Snow and Ice Data Center
OC	Ocean Colour
PAR	Photosynthetic Available Radiation
PC	Photosynthetic carotenoids
PDW	Pacific Deep Water
Perid	Peridinin
PF	Polar Front
PFT	Phytoplankton Functional Type
PFZ	Polar Front Zone
PIG	Quality controlled HPLC pigment dataset
PPC	Photoprotective carotenoids
PSC	Phytoplankton Size Classes
QAA	Quasi Analytical Algorithm
Ra	Radiance anomaly
R_{rs}	Remote sensing reflectance
RMSE	Root-mean-square error
SACCF	Southern Antarctic Circumpolar Front
SAF	Subantarctic Front
SAM	Southern Annular Mode
SAMW	Subantarctic Mode Water
SAZ	Subantarctic Zone
SeaWiFS	Sea-viewing Wide Field-of-view Sensor

SCIAMACHY Scanning Imaging Absorption Spectrometer for Atmospheric Chartography
SNR   Signal-to-noise ratio
SO   Southern Ocean
SOM   Self-Organizing Maps
SST   Sea surface temperature
STF   Subtropical Front
TACC   Sum of all accessory pigments
TChla   Total Chlorophyll-a (Chla plus divinyl chlorophyll-a)
TChlb   Monovinyl chlorophyll-b plus divinyl chlorophyll-b
UCDW   Upper Circumpolar Deep Water
UV   Ultraviolet
VIS   Visible
VRS   Vibrational Raman Scattering
Zea   Zeaxanthin
Z_{eu} Euphotic depth
Z_{pd} Penetration depth

List of Figures

15

List of Tables

Chapter 1

Introduction

1   Introduction

1.1 Motivation

Phytoplankton are microscopic unicellular algae and bacteria (cyanobacteria) living in freshwater and marine ecosystems. Perhaps the most important aspect of phytoplankton is the fact that they are autotroph photosynthetic active organisms and primary producers of organic compounds. During photosynthesis they absorb light to break water molecules and assimilate carbon dioxide (CO_2) by transforming the dissolved inorganic carbon into organic carbon. Subtracting respiratory and non-respiratory carbon release gives the net primary production (NPP), which is the main food supply of the aquatic ecosystem and a key component of the global carbon cycle.

What makes marine phytoplankton unique is that although their biomass represents less than 1% of the global photosynthetic biomass, they are responsible for about half of the total NPP of the earth (Falkowski et al. 1998; Falkowski et al. 2004; Field et al. 1998). Estimates of marine NPP vary from 39 (Rousseaux and Gregg 2014) to 50 PgC yr^{-1} (Carr et al. 2006), similar to the magnitude of terrestrial NPP ($\sim$ 56 PgC yr^{-1}) (Ito 2011). However, the turnover time of marine phytoplankton is short, about one week, ultimately higher than terrestrial plants (Falkowski et al. 1998), which makes marine NPP more efficient than terrestrial NPP. Microalgae, seagrasses and other marine primary producers are responsible for other $\sim$ 5 PgC yr^{-1} (Duarte and Cebrian 1996).

The current number of marine phytoplankton species in the global oceans is not clear. In the early 1990's the estimate was of ca. 4000 species (Sournia et al. 1991), but nowadays, with the advances in technology and sampling effort over the last decades, this number is likely to be underestimated. Generally, phytoplankton can be categorized into major groups according to their size or biogeochemical function (Nair et al. 2008). There are three main phytoplankton size classes (PSC): microplankton (> 20 μm), nanoplankton (2-20 μm) and picoplankton (< 2 μm), and four main phytoplankton functional types (PFT): calcifiers (e.g. coccolithophores), silicifiers (e.g. diatoms, chrysophytes), nitrogen fixers (e.g. cyanobacteria) and dimethyl sulphide producers (e.g. dinoflagellates, haptophytes) (Figure 1.1 upper panel). From a biogeochemical perspective, the classification of phytoplankton based on their functionality is preferred to size-based since the same PSC may contain phytoplankton with common biogeochemical function (Nair et al. 2008).

Different PFTs occupy different niches and functionality in the biogeochemical cycle of the ocean. For example, diatoms are the major silicifiers in the ocean with frustules made of dissolved silicic acid, influencing the cycle of silica in the oceans. Coccolithophores build their external plates (coccolith) from calcium carbonate, altering the seawater alkalinity by the release of CO_2 and, in turn, influencing the marine carbon cycle. In the marine carbon cycle, the size of phytoplankton is associated with sinking rates. Overall, larger and denser cells have higher sinking rates and hence increased export of carbon to the deeper ocean whereas compared to smaller cells. Smaller cells tend to sink more slowly, remaining for longer period in the mixed layer and increasing their chance to be grazed (IOCCG 2014).

The fixed organic carbon in the upper ocean is transformed by several pathways in the water column. These include zooplankton grazing and excretion, particle aggregation and bacteria

decomposition (Siegel et al. 2014) (Figure 1b). These processes are part of the ocean's biological carbon pump. Although most of the organic particles are recycled in the upper ocean (Henson et al. 2011), the sinking of organic particles from the euphotic zone exports approximately 6 - 11 PgC yr^{-1} to the deeper ocean (Siegel et al. 2014; Yao and Schlitzer 2013).
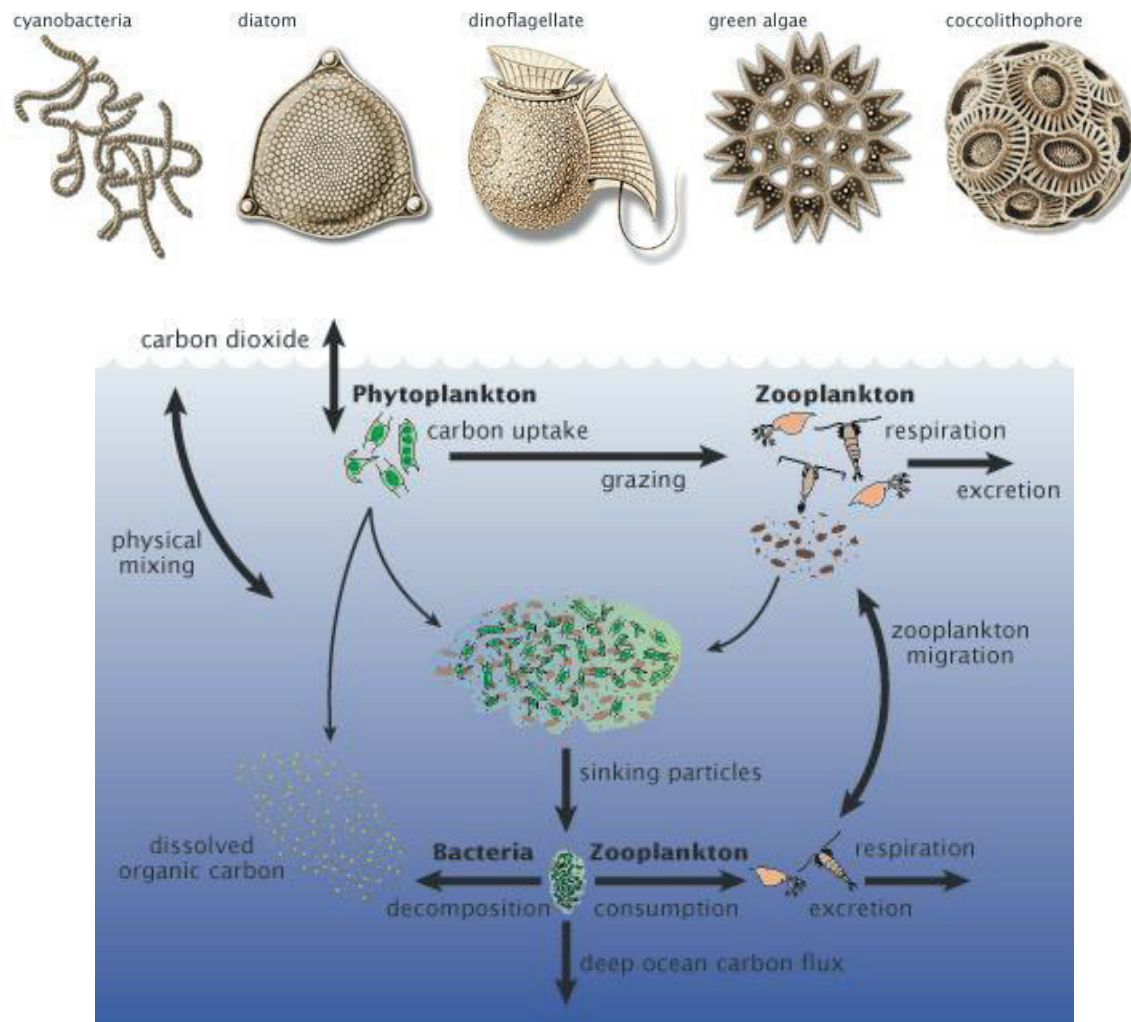
Figure 1.1. On the top: illustration of the major phytoplankton functional types living in the global ocean. On the bottom: simplified scheme of biological carbon pump. Adapted from http://earthobservatory.nasa.gov/.

In the recent years, the interest on quantitative estimation of the abundance and dynamics of different phytoplankton types has increased under the eminent climate change. To what extent the PFTs and primary production will respond to changes in the climate is still unknown. One potential effect is the acidification of the oceans. Ocean acidity increases positively with increase of anthropogenic CO_2 emissions, threating calcifying organisms. In addition, there is mounting evidence that the increase in the sea surface temperature will result in a more stratified ocean and changes in phytoplankton composition, favoring smaller phytoplankton due to reduced nutrient supply (Bopp et al. 2005; Finkel et al. 2010).

Among the Earth's oceans, the Southern Ocean (SO) is responsible for about half of the annual

global anthropogenic atmospheric CO_2 uptake, around 1 PgC (Takahashi et al. 2012). Within this region, the major sink occurs between 30°S and 50°S due to biological and physical mechanisms; biological utilization of CO_2 in summer and the cooling of surface waters in winter (Takahashi et al. 2012). In the marginal ice zone, phytoplankton blooms, elevate phytoplankton biomass (Behrenfeld and Boss 2014), develop with the retreat of sea ice in springtime and summer, which turns surface waters into a strong sink of CO_2 (Takahashi et al. 2009; Takahashi et al. 2012).

Because of the complex spatial and temporal dynamics of phytoplankton, investigations usually rely on satellite remote sensing observations. For several years, ocean colour remote sensing was regarded as the study of the chlorophyll-a concentration (Chla), the main photosynthetic pigment present in phytoplankton and a proxy of their biomass (Martin 2004). During the last four decades since the launch of the first ocean colour sensor, the Coastal Zone Colour Scanner (1978-1986), many sensors have been launched leading to the development of several satellite products (e.g. NPP, PFTs) and significant improvement of our understanding on phytoplankton. However, uncertainties still remain.

Current NPP models differ in terms of complexity and despite the efforts to accurately retrieve NPP from ocean colour, large differences among estimates have been observed for the SO (Campbell et al. 2002; Carr et al. 2006; Saba et al. 2011). These differences can result from uncertainties in the input variables of the models or because the models do not properly represent the "reality" (Milutinovic and Bertino 2011). For example, Saba et al. (2011) investigated how the skill of twenty one ocean color models are affected by the uncertainties in the input variables (e.g. Chla, sea surface temperature) and found that the skills of the models are improved if the errors in the input variables are considered.

Of major interest in studying the oceanic biogeochemical cycle is to know which PFTs are present, their abundance and distribution. Within this context, one PFT of special interest includes the diatoms, which are the major contributors to the oceanic primary production (Rousseaux and Gregg 2014), carbon export and cycling of silica (Smetacek 1999), and together with dinoflagellates, the most diverse PFT (Armbrust 2009; Leblanc et al. 2012). Diatoms are also one of the largest PFTs in terms of size, ranging from micrometers to a few millimeters (Armbrust 2009). Given the biogeochemical and ecological importance of diatoms, several methods based on satellite remote sensing data have been developed to retrieve their global abundance or dominance (Alvain et al. 2005; Bracher et al. 2009; Hirata et al. 2011). Since most of the methods are built on empirical relationships and rely on *in situ* data for model development and validation, refinement is needed when additional data are available to improve the retrieval of diatoms for both global and under-sampled oceans.

Furthermore, much of the primary production occurs during phytoplankton bloom events. The term "phenology" is used to describe periodic events and their relation to environmental conditions (Schwartz 2013). In the case of phytoplankton it refers to blooms. The number of studies on phytoplankton phenology has increased in the recent years since changes in the phytoplankton phenology (e.g. start, duration) can have a large effect on the marine ecosystem (Edwards and Richardson 2004) and are indicators of environmental changes (Racault et al. 2012). Moreover, studies have suggested that the phytoplankton phenology is influenced by climate oscillations (e.g. Southern Annual Mode – SAM, El Niño Southern Oscillation - ENSO). Arrigo and van Dijken (2004) observed a later development of the bloom in the Ross Sea caused

by increased sea ice cover during the El Niño of 1997–1998. Alvain et al. (2013) observed an increase in the dominance of diatoms in the SO during a positive SAM phase, possibly induced by stronger winds which lead to increased mixing and nutrient supply. In spite of these findings, none of the studies investigated in detail the mean patterns and the interannual variability of the different characteristics and stages of blooms (e.g. start date, end date, duration of the growth and decline phases, maximum biomass), their relationship with climate oscillations, neither focused on the abundance of diatoms. In the SO, diatom contribution to primary production was estimated from the NASA Ocean Biogeochemical Model to represent 89% of the total NPP (Rousseaux and Gregg 2014). In addition to that, iron fertilization studies have demonstrated the potential of diatoms as major contributors for the biological drawdown of atmospheric CO_2 and for the export of carbon from the surface to the deep ocean (Smetacek 1999; Smetacek et al. 2012).

Considering the knowledge gaps addressed in the previous paragraphs, this work aims to complement and extend existing studies on ocean colour in the SO. Four main objectives have been pursued:

1) to evaluate the uncertainties of satellite retrievals of euphotic depth (Z_{eu}) and how different Z_{eu} retrievals influence the NPP estimated from satellite;

2) to evaluate and improve the satellite retrievals of diatoms abundance;

3) to investigate the mean pattern and interannual variability of diatom bloom phenology;

4) to examine the potential of ocean colour products to access environmental changes in the Southern Ocean.

1.2 Outline of the thesis

Chapter 2 introduces the specific topics of the three main studies developed in this research work. It starts by introducing satellite algorithms, moves to the SO and briefly explores the dynamics of phytoplankton blooms. In addition, it gives an overview on two important climate oscillations which influence the SO, ENSO and SAM. The next three chapters refer to the three studies.

Chapter 3 addresses the uncertainties of the satellite derived euphotic depth (Z_{eu}), which is a common variable among different ocean colour NPP models. It examines retrievals from two different methods (Chla and inherent optical properties of the water) and sensors (Sea-viewing Wide Field-of-view Sensor - SeaWiFS and Moderate Resolution Imaging Spectroradiometer - MODIS). It shows how the Z_{eu} product can affect the retrievals of NPP. Furthermore, the NPP model used in the study requires the knowledge of the phytoplankton absorption. For this reason, the uncertainty of the satellite-derived phytoplankton absorption is also investigated. This chapter was published in *Remote Sensing of Environment* (Soppa et al. 2013).

Chapter 4 is focused on the satellite retrieval of diatoms abundance. Most investigations have been confined to global oceans. In this study, we highlight the importance of the SO in developing a global algorithm for diatom using the Abundance Based Approach (ABA) of Hirata et al. (2011). A large global *in situ* dataset of phytoplankton pigments is compiled, particularly with more samples collected in the SO. A revision of the ABA is accomplished to take account of the information on the penetration depth and to improve the relationship between diatoms and TChla[1].

As result, the revised global model has improved the retrievals in the SO. Moreover, a regional model, which further improves the retrievals of diatom abundance for the SO, is now available. These findings were published in *Remote Sensing* (Soppa et al. 2014).

Chapter 5 investigates the diatom phenology in the SO applying the regional model to retrieve the abundance of diatoms developed in the previous chapter. Using a novel merged satellite Chla product applied to the regional algorithm, details are given to the diatom bloom phenology during 1997–2012. The different characteristics of the phenology (e.g. start, duration, biomass) are investigated, as well as the interannual variability and trends. Finally, deep insights are given to how the interannual variability of diatom bloom phenology could be modulated by the large scale climate oscillations ENSO and SAM.

Chapter 6, the concluding chapter, draws together the main findings of the thesis and provides an outlook for future research.

---

[1]We refer to Chla (monovinyl chlorophyll-a plus chlorophyllid-a, allomers and epimers) as TChla (Chla plus divinyl chlorophyll-a) since *Prochlorococcus* (which contain divinyl chlorophyll-a) is uncommon in the Southern Ocean south of 40°S. In chapter 4 we explicit refer to TChla because we consider the global distribution of phytoplankton.

Chapter 2

Scientific background

2   Scientific background

2.1   Ocean colour retrievals – an overview

The principle of ocean colour remote sensing is that the information of the radiance in the UV-VIS (ultraviolet-visible) part of the spectrum can be used to infer the water optical properties. The total radiance (L_T, W m^{-2} sr^{-1}) measured by the satellite sensor has different origins, but is the water leaving radiance (L_w), originated from the in-water scattering, which contains the information needed for the retrieval of the water properties (Figure 2.1). Within the water, the solar radiation is absorbed and scattered by water molecules and water constituents. These constituents, such as the phytoplankton, suspended non-algal particles and colored dissolved organic matter (CDOM or *gelbstoff*), absorb and scatter the radiation at specific wavelengths and with different intensities. The different spectral signatures and the fraction of each dissolved and particulate constituents, together with the water molecules, control the backscattered radiation that leaves the water and which carries information on the optical active constituents.
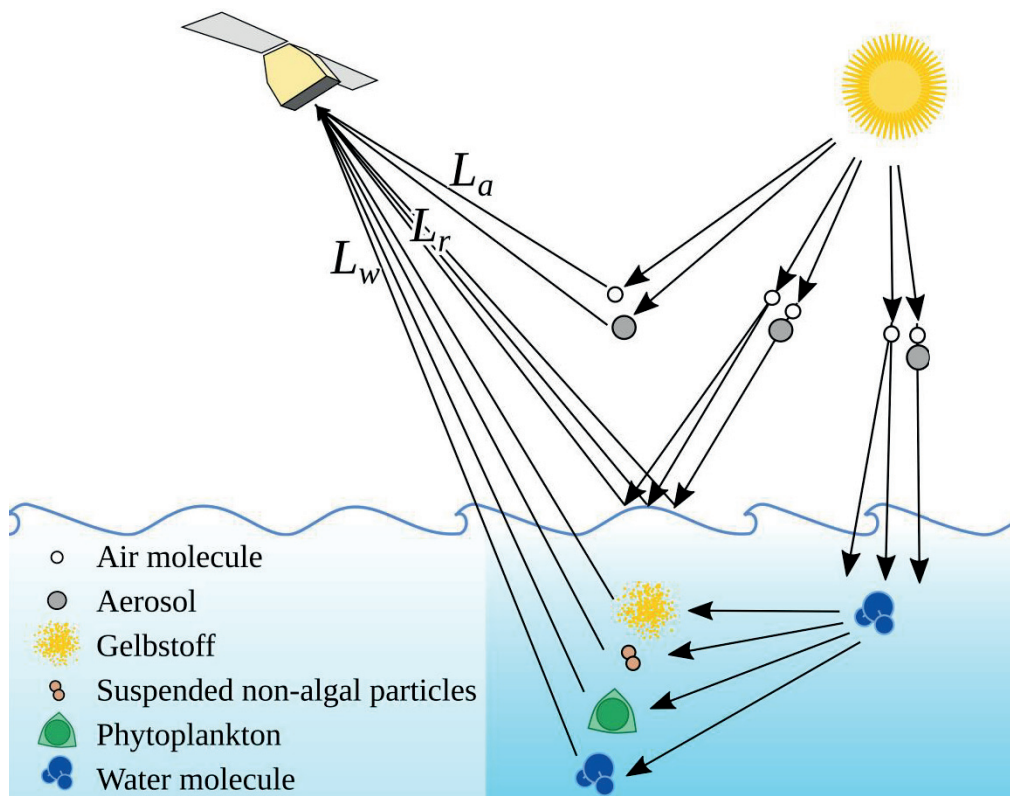
Figure 2.1. A schematic showing the components of the total upwelling radiance at the sensor: water leaving radiance (L_w), atmospheric radiance (L_a) and surface-reflected radiance (L_r). Based on Martin (2004).

The L_w represents up to 10% of the total upwelling radiance measured by the satellite sensor (average for the visible spectrum, Kirk 2011). The other 90% originates from the scattering within

the atmosphere (L_a – atmosphere radiance, e.g. gases, aerosols, clouds) and the reflection at the ocean/water surface (L_r – reflected radiance, e.g. sun glint, foam), but those contributions can be mostly separated from the L_w by atmospheric correction algorithms (Kirk 2011). The L_T can be expressed as the sum of the different radiances (omitting the angular dependencies here and further on):

$$L_T(\lambda) = L_a(\lambda) + tL_w(\lambda) + L_r(\lambda) \tag{2.1}$$

where λ is the wavelength and t is an atmospheric transmittance factor to account for the attenuation of L_w from the surface to the satellite. However, it is the reflected (ρ) upwelling radiation from the ocean and passing through the atmosphere that is derived from ocean colour sensors and that that is directly related to the water optical constituents (Kirk 2011). The ρ is preferred to L because it can be more accurately estimated. Thus, Equation 2.1 can be re-written as:

$$\rho_T(\lambda) = \rho_a(\lambda) + t\rho_w(\lambda) + \rho_r(\lambda) \tag{2.2}$$

The reflectance of the ocean ρ_w (adimensional) can be expressed as:

$$\rho_w(\lambda) = \frac{\pi L_w(\lambda)}{F_0(\lambda)\cos\theta} \tag{2.3}$$

where F_0 is the extraterrestrial solar irradiance (top of atmosphere radiance, W m^{-2}), θ is the solar zenith angle and π converts the solar irradiance to units of radiance.

Rearranging the equation 2.3, L_w can be obtained as:

$$L_w(\lambda) = \frac{F_0(\lambda)\cos\theta}{\pi}\rho_w(\lambda) \tag{2.4}$$

The L_w is often converted to normalized L_w (nL_w, W m^{-2} sr^{-1}) to remove the effects of the atmosphere attenuation and solar orientation (Kirk 2011). The nL_w is obtained as:

$$nL_w(\lambda) = \frac{L_w(\lambda)}{\varepsilon_c\cos\theta\, t_D(\theta_0,\lambda)} \tag{2.5}$$

where ε_c is a correction factor accounting for changes in the Earth-Sun distance and t_D the irradiance transmittance factor.

The nL_w is often expressed as remote sensing reflectance (R_{rs}, sr^{-1}) or radiance reflectance. The R_{rs} is the standard input of many ocean colour algorithms, including the derivation of the Chla concentration, obtained as:

$$R_{rs}(\lambda) = \frac{nL_w(\lambda)}{F_0(\lambda)} \tag{2.6}$$

The satellite signal is related to the optical properties of the water and before more details on satellite algorithms are introduced, it is worth to define the two classifications of the optical properties of the water, which are widely used in ocean optics: (i) the inherent optical properties (IOPs) and the apparent optical properties (AOPs). Absorption and scattering of solar radiation are IOPs. Their magnitude depends only on the concentration and type of the substance and not on the illumination geometry or light distribution in the water (Kirk 2011). The AOPs (e.g. R_{rs}), on the other hand, depend on the IOPs, as well as on the geometrical structure of the light field.

Thus, the magnitude and the spectral characteristics of the R_{rs} can be related to IOPs and can be expressed as a function of absorption and backscattering coefficients as result of radiative transfer models (Gordon et al. 1988):

$$R_{rs}(\lambda) = \left(\frac{f(\lambda)}{Q(\lambda)}\right)\left(\frac{t}{n^2}\right)\left(\frac{b_b(\lambda)}{a(\lambda)+b_b(\lambda)}\right) \qquad (2.7)$$

where f is an empirical factor that depends on the IOPs, incoming distribution of radiance and λ (Reynolds et al. 2001) and Q is the ratio of the upwelling irradiance (E_u) to radiance (L_u). f/Q is also specified as a shape factor describing the angular structure of the light field (Morel et al. 2002; Zaneveld 1995). t is the transmittance factor of the air-water interface, n is the real part of the refractive index of the water, a is the total absorption coefficient, b_b is the total backscattering coefficient. The term "total" refers to the sum of the absorption coefficients of water, dissolved matter and suspended particles (non-algal and algal particles). Likewise, b_b is the sum of the backscattering coefficients of the water and suspended particles; assuming no significant b_b for dissolved matter. In the next sections, the dependence on wavelength is further omitted for simplicity. Most semi-analytical algorithms (e.g. Garver-Siegel-Maritorena Model, Quasi-Analytical Algorithm) used to retrieve Chla and IOPs are based on the relationship between R_{rs} and IOPs.

2.1.1 Chlorophyll-a concentration

Phytoplankton contain several photosynthetic pigments which absorb light in different parts of the spectrum from 400 to 700 nm. The spectral absorption characteristics of phytoplankton are modulated by their pigment composition with different pigments exhibiting distinct absorption features (IOCCG 2014). These pigments are one of the absorbers of the light in the water; together with the coloured dissolved organic matter, non-algal particles and the water molecule itself. The Chla is the major photosynthetic pigment present and shared by different phytoplankton groups (except for *Prochloroccocus sp.*). For this reason, it is commonly used as indicator of the biomass of phytoplankton.

The Chla has a distinct spectral characteristic in the visible spectrum, strongly absorbing at blue and red bands, and less in the green region (Mobley 1994, Figure 2.2a). This spectral signature makes the retrieval of Chla from satellite sensors possible and those were developed with bands to exploit the information in the blue (443, 490, 510 nm) and green (550 or 555 nm) regions. The standard SeaWiFS (OC4v.6) and MODIS (OC3M) Chla algorithms are empirically

derived from a large global dataset of *in situ* measurements of Chla concentration (hereafter referred to as Chla) and the ratio of R_{rs} in different bands. The Chla is determined from a polynomial function that relates the maximum band ratio (X) to the Chla, defined as:

$$log_{10}(Chla) = c_0 + c_1X + c_2X^2 + c_3X^3 + c_4X^4 \qquad (2.8)$$

where for SeaWiFS,

$$X = log_{10}\left[\max\left(\frac{(R_{rs}(443),R_{rs}(490),R_{rs}(510))}{R_{rs}(555)}\right)\right] \qquad (2.9)$$

For MODIS two band ratios are used to replace the three band ratios in the SeaWiFS algorithm: $R_{rs}(443)/R_{rs}(550)$ and $R_{rs}(490)/R_{rs}(550)$. The coefficients c_0, c_1, c_2, c_3 and c_4 are 0.3272, -2.9940, 2.7218, -1.2259 and -0.5683 for SeaWiFS and 0.283, -2.753, +1.457, +0.659 and -1.403 for MODIS (Feldman and McClain 2012; O'Reilly et al. 2000). The band ratio is used instead of individual R_{rs} to reduce the uncertainties due to light propagation through the interface water-air while the switch of R_{rs}-ratios preserves a high signal-to-noise ratio (SNR) (Martin 2004; O'Reilly et al. 2000).

As Chla increases, the shape and magnitude of the reflectance spectrum changes (see Figure 2.2b). The region in the spectrum with higher R_{rs} shifts to higher wavelengths and the magnitude decreases. In low Chla waters the SNR is higher at 443 than at 490 and 510 nm bands, but at higher Chla the SNR is lower at 443 nm due to the stronger absorption (lower reflectance) in the blue region and thus the other bands are used instead (Dierssen 2010; O'Reilly et al. 2000).
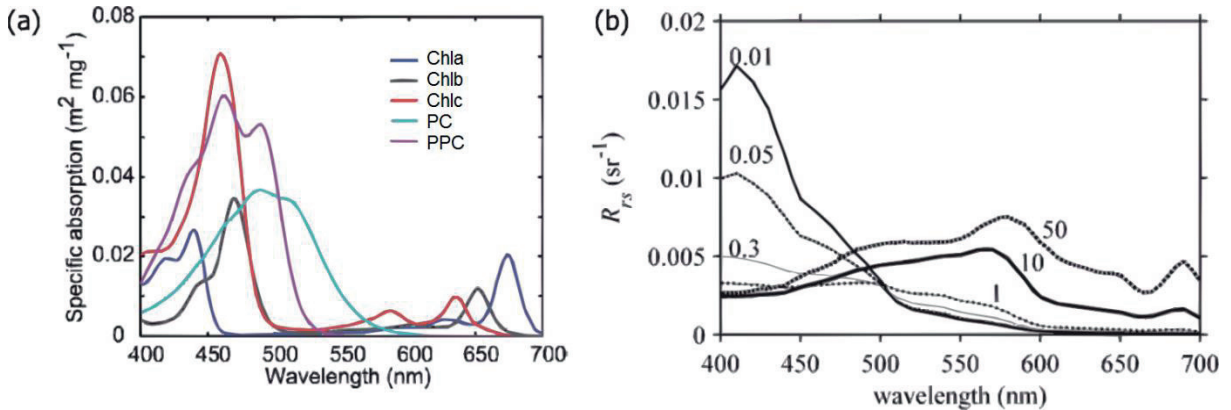
Figure 2.2. **(a)** Specific pigment absorption spectra for major phytoplankton pigments: chlorophyll-a (Chla), chlorophyll-b (Chlb), chlorophyll-c (Chlc), photosynthetic carotenoids (PC) and photoprotective carotenoids (PPC). Adapted from IOCCG (2014); originally from Bidigare et al. (1990). **(b)** Spectral changes in the R_{rs} with respect to changes in Chla. Numbers above the lines indicates the Chla concentration in mg m^{-3}. Adapted from Dierssen (2010).

Nevertheless, these algorithms were developed considering that the optical properties of the water are determined primarily by phytoplankton (case 1 waters), assuming that all other non-water constituents vary closely with Chla (IOCCG 2006). Thus, when the optical properties of the

water are dominated by other constituents (case 2 waters), such as non-algal particles or CDOM, the algorithms show higher uncertainties.

In situ measurements of Chla use mostly either fluorometric or the High Performance Liquid Chromatography (HPLC) techniques. The advantages of fluorometric measurements are the lower costs and it is less time consuming than HPLC. However, it is less accurate than HPLC due to the spectral overlap of the fluorescence of other chlorophyll pigments. For example, when chlorophyll-b is present in the sample, it leads to an underestimation of Chla (Arar and Collins 1997). Nowadays HPLC is the standard method to determine Chla concentration used to develop and validate satellite Chla algorithms (IOCCG 2014). In the former days, fluorometric Chla data were used for this purpose. Another advantage of the HLPC technique is that it enables the simultaneous identification of a whole set of pigments.

2.1.2   Phytoplankton absorption

Chla is not the only pigment present in phytoplankton. There are other pigments that more efficiently absorb the light at different wavelengths and with either photosynthetic or photoprotective function (Kirk 2011). These pigments are also called accessory pigments. For example: chlorophylls (chlorophyll-b), carotenoids and phycobiliproteins (phycocyanin). The phytoplankton absorption spectrum results from the combination of the pigments present in the phytoplankton. Thus, the spectral signature of the phytoplankton absorption (a_{ph}) varies with the pigment composition, but also with pigment packaging.

Similarly to Chla, the phytoplankton absorption can also be derived from R_{rs} using semi-analytical algorithms, such as the Quasi-Analytical Algorithm (QAA). The difference to band ratio algorithms is that semi-analytical algorithms are based on theoretical models to relate R_{rs} to IOPs, together with empirical models to describe the relationship between IOPs and the water optical constituents (Martin 2004). Briefly, the QAA is an inversion algorithm that derives the IOPs (absorption and backscattering coefficients at different wavelengths) from the R_{rs} using empirical, analytical and semi-analytical approximations (Hirawake et al. 2011; Lee et al. 2009; Lee et al. 2002). First, the total absorption coefficient (a) is calculated at a reference wavelength (λ_0, 555 nm for SeaWiFS and 550 nm for MODIS):

$$a(\lambda_0) = a_w(\lambda_0) + 10^{-1.146-1.366X-0.469X^2} \tag{2.10}$$

where $a_w(\lambda_o)$ is the absorption coefficient of pure seawater from Pope and Fry (1997) and,

$$X = log_{10}\left[\frac{r_{rs}(443)+r_{rs}(490)}{r_{rs}(\lambda_0)+5\frac{r_{rs}(667)}{r_{rs}(490)}r_{rs}(667)}\right] \tag{2.11}$$

where r_{rs} is the R_{rs} just below the surface expressed as:

$$r_{rs}(\lambda) = \frac{R_{rs}(\lambda)}{(0.52+1.7R_{rs}(\lambda))} \tag{2.12}$$

The r_{rs} can be modeled as a function of the $\frac{b_b}{a+b_b}$ (represented by u):

$$u(\lambda) - \frac{b_b(\lambda)}{a(\lambda)+b_b(\lambda)} = \frac{-0.0895+\sqrt{0.008+0.499 r_{rs}(\lambda)}}{0.249} \qquad (2.13)$$

Knowing $a(\lambda_o)$ and $u(\lambda_o)$, the particulate backscattering coefficient (b_{bp}) at λ_o can be derived by:

$$b_{bp}(\lambda_0) = \frac{u(\lambda_0)a(\lambda_0)}{(1-u(\lambda_0))} - b_{bw}(\lambda_0) \qquad (2.14)$$

where b_{bw} is the backscattering coefficient of pure seawater from Morel (1974) at the λ_o. Subsequently, the calculation is propagated to other wavelengths by:

$$b_b(\lambda) = b_{bw}(\lambda) + b_{bp}(\lambda_0)\left(\frac{\lambda_0}{\lambda}\right)^Y \qquad (2.15)$$

where Y defines the spectral shape of $b_b(\lambda)$ and is defined as:

$$Y = 2\left(1 - 1.2exp\left(-0.9\frac{r_{rs}(443)}{r_{rs}(555)}\right)\right) \qquad (2.16)$$

Then the total absorption a can be derived for the other wavelengths as:

$$a(\lambda) = \frac{(1-u(\lambda))b_b(\lambda)}{u(\lambda)} \qquad (2.17)$$

Knowing $a(\lambda)$, the $a_{ph}(\lambda)$ can be calculated by the following steps:

$$\zeta - \frac{a_{ph}(412)}{a_{ph}(443)} = 0.74 + \frac{0.2}{0.8+\frac{r_{rs}(443)}{r_{rs}(\lambda_0)}} \qquad (2.18)$$

$$\delta - \frac{a_g(412)}{a_g(443)} = -\exp(S(443-412)) \qquad (2.19)$$

S is a parameter to describe the spectral shape of the absorption of gelbstoff and non-algal particles (a_g) calculated as:

$$S = 0.015 + \frac{0.002}{0.6+\frac{r_{rs}(443)}{r_{rs}(\lambda_0)}} \qquad (2.20)$$

$a_g(443)$ is determined as:

$$a_g(443) = \frac{a(412) - \zeta a(443)}{\delta - \zeta} - \frac{a_w(412) - \zeta a_w(443)}{\delta - \zeta} \tag{2.21}$$

For the other λ, a_g is calculated as:

$$a_g(\lambda) = a_g(443) \exp(-S(\lambda - 443)) \tag{2.22}$$

When the values of $a(\lambda)$, $a_w(\lambda)$ and $a_g(\lambda)$ are known, $a_{ph}(\lambda)$ can be derived as:

$$a_{ph}(\lambda) = a(\lambda) - a_g(\lambda) - a_w(\lambda) \tag{2.23}$$

The standard *in situ* measurements of a_{ph} are carried out using the filter-pad method. In short, water samples are filtered and placed in spectrophotometer which measures the light transmitted through the filter. This process yields to the particulate absorption. To obtain the a_{ph}, the filter is bleached with methanol to remove the pigments and the optical density is measured another time. The a_{ph} is calculated as the difference between the measurements before and after the pigments were removed. A detailed technical description can be found in Tassan and Ferrari (1995).

2.1.3 *Euphotic Depth*

Photosynthesis only occurs if light is available. The part of the water column with sufficient light for supporting photosynthesis and thus NPP is called euphotic zone, or euphotic depth (Z_{eu}) (Falkowski and Raven, 2007; Kirk 2011). In biological terms, Z_{eu} is the bottom of the euphotic zone. In physical terms, Z_{eu} is the depth where the downward photosynthetic available radiation (PAR, E_dPAR), the radiation in the spectral range of $400 - 700$ nm, is reduced to 1% of its value at surface (E_dPAR(0)) (Morel and Berthon 1989).

In ocean colour remote sensing, Z_{eu} is mostly estimated (i) empirically from the surface chlorophyll-a concentration (Chla, Z_{eu}-Chla) and (ii) semi-analytically from the inherent optical properties of the water (IOPs, Z_{eu}-IOP). The main difference between the two approaches is that the derivation of Z_{eu} from Chla assumes that the waters are classified as case 1. On the other hand, the IOP approach determines the vertical distribution of light in the water from the IOPs and therefore Z_{eu} can be retrieved in optically complex waters as well, as shown by Lee et al. (2007) and Shang et al. (2011b).

The relationship between Chla and Z_{eu} can be expressed as (Morel, in Lee et al. 2007):

$$Z_{eu} = 34(Chla)^{-0.39} \tag{2.24}$$

From IOPs, the diffuse attenuation coefficient of PAR, K_{PAR} can be parameterized as a function of $a(490)$ and $b_b(490)$, which in turn are determined using the QAA as described in the previous section (section 2.1.2). The vertical distribution of $K_{PAR}(z)$ is expressed as (Lee et al. 2005; Lee et al. 2007):

$$K_{PAR}(z) = K_1 + \frac{K_2}{(1+z)^{0.5}} \tag{2.25}$$

where z is the depth and the coefficients K_1 and K_2 determined as,

$$K_1 = [\chi_0 + \chi_1(a(490))^{0.5} + \chi_2 b_b(490)](1 + \alpha_0 \sin(\theta)) \tag{2.26}$$

where χ_0, χ_1, χ_2 and α_0 have values of -0.057, 0.482, 4.221 and 0.090, respectively, and,

$$K_2 = [\chi_3 + \chi_4 a(490) + \chi_5 b_b(490)](\alpha_1 + \alpha_2 \cos(\theta)) \tag{2.27}$$

where $\chi_3, \chi_4, \chi_5, \alpha_1$ and α_2 have values of 0.183, 0.702, -2.567, 1.465 and -0.667, respectively (Lee et al. 2005).

As mentioned above, Z_{eu} is the depth where $E_d PAR(z)$ is 1% of $E_d PAR$ at surface. The downward irradiance decreases exponentially with depth according to:

$$E_d PAR(z) = E_d PAR(0) e^{-K_{PAR}(z).z} \tag{2.28}$$

Thus, Z_{eu} can be determined as:

$$K_{PAR}(z) \, Z_{eu} = 4.605 \tag{2.29}$$

In situ Z_{eu} can be determined from vertical profiles of PAR measured with radiometers. The sensors are mounted in a frame and lowered in the water avoiding the shadow of the ship. The measurements have to be corrected for a series of uncertainties such as the self-shading, variation of the incident sunlight during the deployment, bubbles and waves.

2.1.4 *Phytoplankton functional types*

As mentioned in Chapter 1, the intensity of the biological pump strongly depends on the size and composition of phytoplankton cells, in addition to the structure of the trophic community. For this reason it is important to distinguish the phytoplankton functional types (PFTs). Estimates of PFTs from satellite can be also applied to support biogeochemical models in parameter estimation and validating simulations for example (Robinson 2010). From satellite remote sensing PFTs can be detected using different methods. In the following, satellite remote sensing algorithms that are able to globally retrieve diatoms are introduced. We split them into abundance based and spectral based approaches.

2.1.4.1 Abundance based approach

Abundance based approaches (ABA) are often used to retrieve global maps of phytoplankton community (PFTs) and size structure. These algorithms are based on the concept that the phytoplankton community structure changes with Chla. The Hirata et al. (2011) ABA method uses satellite-derived Chla together with empirical relationships between Chla and PFTs (diatoms, dinoflagellates, green algae, haptophytes, prokaryotes, pico-eukaryotes and *Prochlorococcus* sp.) and is tuned using *in situ* phytoplankton pigment measurements. The ABA methods, that are tuned using phytoplankton pigment data, are based on the assumption that different PFTs contain different types of pigments, and that usually one major pigment (or several depending on the PFT) can be attributed to a specific PFT (also called diagnostic pigment - DP, Table 2.1).

Table 2.1. Phytoplankton functional types and their respective diagnostic pigments (Hirata et al. 2011; IOCCG 2014; Vidussi et al. 2001).

Phytoplankton Functional Types	Phytoplankton pigments / Diagnostic Pigments
Diatoms	Fucoxantin (Fuco)
Dinoflagellates	Peridinin (Perid)
Cryptophytes	Alloxanthin (Allo)
Prymensiophytes and chrysophytes	19'-hexanoyloxyfucoxanthin (Hexfuco)
Prymensiophytes	19'-butanoyloxyfucoxanthin (Butfuco)
Cryptophytes	Alloxanthin (Allo)
Green algae	Monovinyl chlorophyll-b
Prochlorophytes	Divinyl chlorophyll-b
Cyanobacteria and prochlorophytes	Zeaxanthin (Zea)

The ABA starts by calculating the fraction (*f*) of Chla attributed to a specific PFT or PSC using concentrations of DP from a large *in situ* database of phytoplankton pigment data (i.e. Diagnostic Pigment Analysis – DPA, Vidussi et al. 2001, Uitz et al. 2006). According to Uitz et al. (2006), the Chla can be expressed by the weighted sum of seven diagnostic pigments (DP) as:

$$Chla \sim DP_w = a_1 Fuco + a_2 Perid + a_3 Hexfuco + a_4 Butfuco + a_5 Allo + a_6 TChlb + a_7 Zea$$
(2.30)

where DP_w is the estimated Chla, a_i are the partial coefficients (derived from multiple regression analysis, Uitz et al. 2006). The summed terms on the right are the concentration of the diagnostic pigments representing the main PFTs (Table 2.1).

The *f*-PFT/PSC is determined as the ratio of the DPs of a specific PFT/PSC to the sum of the weighted concentration of the seven DPs (DP_w). For example, the fraction of Chla that is attributed to diatoms (*f*-Diatom) is derived as:

$$f - Diatom = \frac{a_1 Fuco}{DP_w}$$
(2.31)

f-Diatom values lower than 0 and greater than 1 are set to 0 and 1, respectively. Table 2.2 presents the DPA applied to calculate other PFTs and PSCs in Hirata et al. (2011).

Table 2.2. Equations used to calculate *f*-PFT/PSC (adapted from Hirata et al. 2011). DP_w is the sum of the weighted concentration of the DP and a_i are the partial coefficients as in Uitz et al. (2006).

PFTs/PSCs	Equation
Microplankton	$(a_1 \text{ Fuco} + a_2 \text{ Perid}) / DP_w$
Diatoms	$(a_1 \text{ Fuco}) / DP_w$
Dinoflagellates	$(a_2 \text{ Perid}) / DP_w$
Nanoplankton	$(X_n\, a_3 \text{ Hexfuco} + a_6 \text{ Chlb} + a_4 \text{ Butfuco} + a_5 \text{ Allo}) / DP_w$
Haptophytes	Nanoplankton - Green Algae
Green Algae	$(a_6 \text{ TChlb}) / DP_w$
Picoplankton	$(Y_p\, a_3 \text{ Hexfuco} + a_7 \text{ Zea}) / DP_w$
Prokaryotes	$(a_7 \text{ Zea}) / DP_w$
Pico-eukaryotes	Picoplankton – Prokaryotes
Prochlorococcus sp.	0.74 DvChla/Chla

Once the *f*-PFT/PSC has been determined (Table 2.2), the relationship between *f*-PFT/PSC and Chla can be quantified using empirical equations (Figure 2.3a), with the empirical equation varying according to the PFT/PSC (Table 2.3). With the knowledge of the empirical model, its parameters and Chla, which is operationally produced as a satellite product, it is possible to retrieve the *f*-PFT/PSC (Figure 2.3b). The Chla of each PFTs/PSC can be determined by multiplying the *f*-PFT/PSC by the Chla. A limitation of retrieving PFTs from HPLC pigments is the presence of a DP in more than one PFT (Hirata et al. 2011; Uitz et al. 2006). Thus, uncertainties of ABA vary according to the PFT of choice and the best performance was obtained for picoplankton (root mean squared error = 7.12 % Chla, see Table 4 in Hirata et al. 2011). For diatoms the coefficient of determination was 0.73 and the root mean squared error 7.98 % Chla (Hirata et al. 2011).

Table 2.3. Models and parameters used to estimate the *f*-PFT/PSC (adapted from Hirata et al. 2011).

PFTs/PSCs	Equation	p_0	p_1	p_2	p_3	p_4	p_5	p_6
Microplankton	$[p_0 + \exp(p_1\, x + p_2)]^{-1}$	0.91	-2.73	0.4				
Diatoms	$[p_0 + \exp(p_1\, x + p_2)]^{-1}$	1.33	-3.98	0.20				
Dinoflagellates	Microplankton – Diatoms							
Nanoplankton	1 - Microplankton – Picoplankton							
Haptophytes	Nanoplankton - Green Algae							
Green Algae	$(p_0 / y) \exp[(p_1\, (x + p_2)^2]$	0.25	-1.26	-0.55				
Picoplankton	$-[p_0 + \exp(p_1\, x + p_2)]^{-1} + p_3\, x + p_4$	0.15	1.03	-1.56	-1.86	2.99		
Prokaryotes	$(p_0 / p_1 / y) \exp[p_2\, (x + p_3)^2 / p_1^2] + p_4\, x^2 + p_5\, x + p_6$	0.007	0.62	-19.52	0.96	0.10	-0.12	0.06
Pico-eukaryotes	Picoplankton – Prokaryotes							
Prochlorococcus sp.	$(p_0 / p_1 / y) \exp[p_2\, (x + p_3)^2 / p_1^2] + p_4\, x^2 + p_5\, x + p_6$	0.01	0.68	-8.6	0.97	0.007	-0.16	0.04

$x = \log_{10}(\text{Chla})$; $y = \text{Chla}$
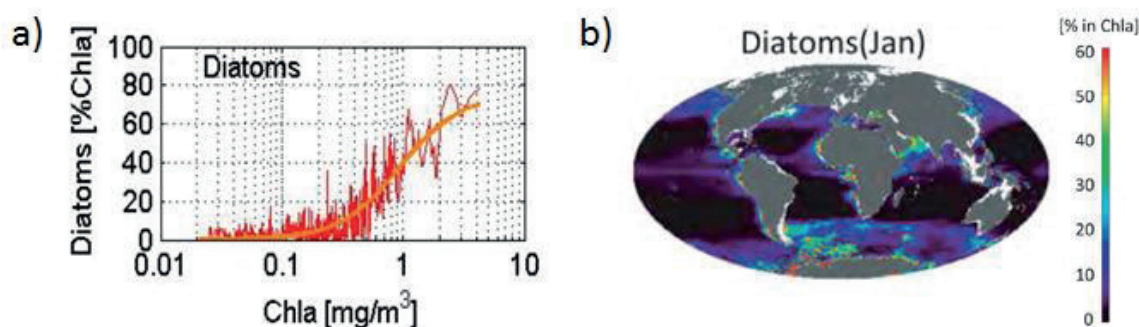
Figure 2.3. (a) Relationship between Chla and Diatom (% Chla). To get % Chla, the *f*-Diatom is multiplied by 100. The orange line represents the model and fitting parameters of Hirata et al. (2011) for Diatoms, as presented in Table 3, red line represents a running mean of the *in situ* data. Modified from Hirata et al. (2011). **(b)** Mean % of Chla of Diatoms over 1998-2010 for January. Modified from IOCCG (2014).

2.1.4.2 Spectral based approach

Spectral approaches to retrieve the phytoplankton community structure are the algorithms of Alvain et al. (2005; 2008) and Bracher et al. (2009). Alvain et al. (2005; 2008) developed an algorithm called PHYSAT that determines the dominance of PFTs (diatoms, nano-eukaryotes, *Prochlorococcus*, *Synechocococus*-like and *Phaeocystis*-like) by identifying their specific spectral signatures in the nL_w, more specifically in the satellite radiance anomaly (Ra) from SeaWiFS or MODIS sensors. Ra is defined as the ratio of nL_w and a reference nL_w (nL_{wref}) at five wavelengths (e.g. 412, 443, 488, 531 and 555 nm for MODIS). The nL_{wref} represents the average nL_w spectra for different Chla intervals from 0.02 to 3 mg m^{-3} (Ben Mustapha et al. 2014). The normalization by the nL_{wref} removes the first order effect of the Chla in the nL_w (Alvain et al. 2005). A dataset of satellite Ra spectra is matched with HPLC pigment data collected in different regions of the global ocean to identify Ra spectra associated with a specific PFTs. Based on this information, Alvain et al. (2005) established thresholds and shape criteria to distinguish between the spectral signatures of different PFTs which were initially used to classify the satellite Ra spectra to obtain maps of the PFTs dominance.

The PHYSAT was improved by Ben Mustapha et al. (2014) by using Self-Organizing Maps (SOM). The SOM allows to automatically classify a larger number of satellite Ra spectra based on their similarity in shape and amplitude, without the necessity of establishing thresholds. The Ra at each pixel is assigned to a specific PFT if the Ra spectrum is between the mean ± one standard deviation of the specific PFT Ra spectrum (or reference vector in the case of SOM). Otherwise, the pixel is assigned to "unidentified phytoplankton assemblage" group (Figure 2.4). Validation with *in situ* pigment data showed 83.3%, 66.7%, 58.1% and 66.7% of successful identification for diatom, nano-eukaryotes like, *Prochlorococcus* and *Synechocococus*-like, respectively (Ben Mustapha et al. 2014).
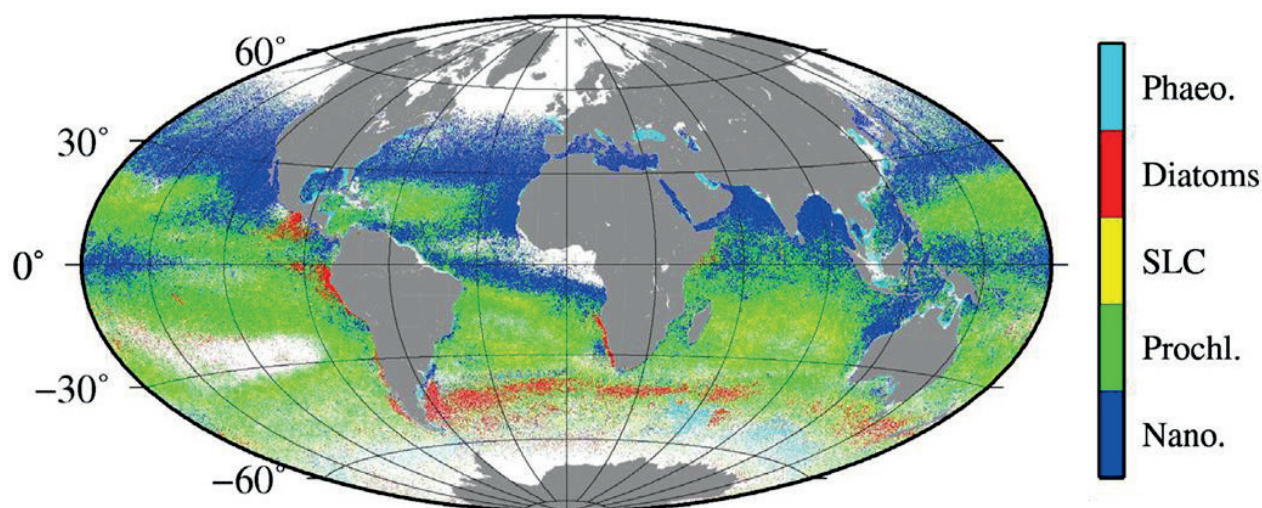
Figure 2.4. Climatology of the dominance of multiple PFTs for January (1997-2010) applied to SeaWiFS. White areas represent missing data or unidentified phytoplankton type. Modified from Ben Mustapha et al. (2014).

Like PHYSAT, PhytoDOAS is based on analyzing optical information and retrieves diatoms, cyanobacteria, dinoflagellates and coccolithophores, by identifying their specific absorption in the backscattered solar radiation. This is done by using the differential optical absorption spectroscopy method (DOAS). First, the ratio of the backscattered solar radiation at the top of atmosphere and the extraterrestrial irradiance, both measured by the sensor, is calculated. Exploiting only the differential structures (a fitted low order polynomial is subtracted) all contributions of oceanic and atmospheric constituents are fitted to this ratio, for example phytoplankton groups, water vapour, water and atmospheric trace gases (e.g. ozone). The contributions of constituents with low level of spectral structure, including Mie and Rayleigh scattering and absorption of colored detrital matter, are approximated by a low order polynomial.

The DOAS method is applied to two spectral windows; one in the UV range of 340 nm to 385 nm and a second in the visible range of 429 nm to 521 nm. The UV window is used to retrieve the spectral signature of the Vibrational Raman Scattering (VRS) of water molecules, a proxy for the light penetration depth in the water (Dinter et al. 2015; Vountas et al. 2007). The DOAS-fit in the visible window yields the specific phytoplankton absorption signatures. Thus, fitting is carried out twice, first excluding the VRS part to derive the fit factor for the PFTs and, second, excluding the PFT part to derive the fit factor for the VRS of water molecules, which is extrapolated to the visible window. The concentration of each PFT is calculated by dividing the fit factor for the specific PFT by the light penetration depth in the water (Bracher et al. 2009, Vountas et al. 2007).

The extended PhytoDOAS version, called multi-target fit, by Sadeghi et al. (2012) simultaneously fits the absorption spectra of diatom, dinoflagellates and coccolithophores. Up to now, PhytoDOAS is the only spectral algorithm applied to hyperspectral satellite data. Application of PhytoDOAS is restricted to hyperspectral sensors and up to now it was applied to data from the Scanning Imaging Absorption Spectrometer for Atmospheric Cartography (SCIAMACHY, level-1 top of atmosphere data) onboard the European Environmental Satellite (ENVISAT) (Figure 2.5). A direct validation with *in situ* measurements is difficult owing to the large pixel size (about 30 km by 60 km). Nevertheless, preliminary validation by Bracher et al. (2009) indicated that

satellite-derived information on cyanobacteria and diatom distributions matched well with corresponding *in situ* information based on pigment analyses of co-located water samples.
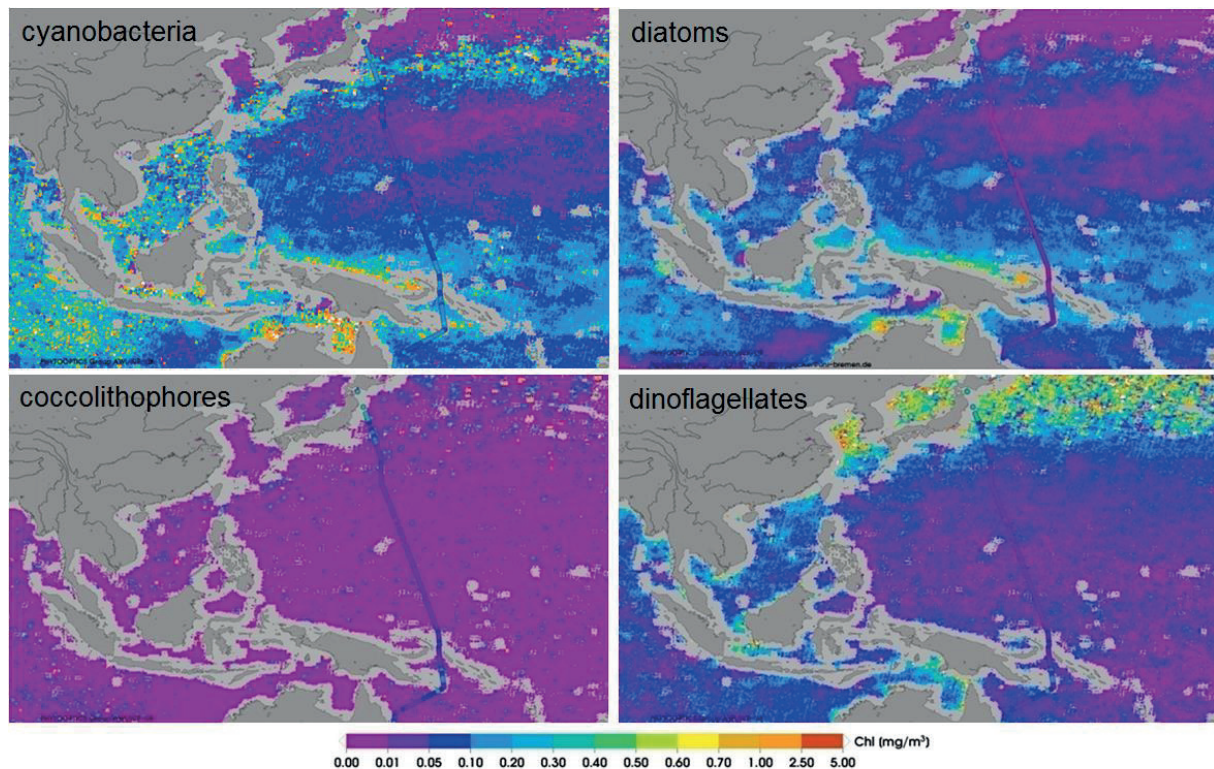
Figure 2.5. Monthly Chla for specific phytoplankton groups – October 2009. The coloured circles are the Chla of the respective groups derived from HPLC pigment concentration and CHEMTAX analysis of *in situ* samples taken during TransBrom Sonne cruise (9–23 October 2009) (IOCCG 2014).

2.1.4.3 Potentials and limitations of the methods

The potentials and limitations of the above mentioned algorithms are summarized in Table 2.4. Some limitations are occasioned by the sensor and not directly by the algorithms. For example, although PHYSAT can be applied on hyperspectral satellite data, currently there is no global product of water leaving radiance from hyperspectral sensors, limiting the application of the algorithm to multispectral sensors. Besides PhytoDOAS, all current global PFT products are retrieved from multispectral sensors, which have a much higher spatial resolution (1 to 4.6 km) and temporal coverage (1-3 days), when compared with current hyperspectral sensors. On the other hand, the small number of wavelength bands and the broad band resolution of multispectral sensors provide limited information on the phytoplankton absorption structures for spectral algorithms (i.e. PHYSAT). As mentioned earlier, although different PFTs have different marker pigments, they can also have some pigments in common. This is a limitation of retrieving PFTs from HPLC pigments using the diagnostic pigment analysis, as in some abundance based approaches (i.e. Brewin et al. 2010, Hirata et al. 2011). As shown by Brewin et al. (2014), abundance-based approaches can be also parameterized using size-fractionated chlorophyll data

derived from filtration and in-vitro fluorometry for example.

Using PhytoDOAS, the specific optical signatures of different PFTs are separated by their specific differential absorption spectra only visible in hyperspectral data. The drawback of applying PhytoDOAS is the coarser spatial resolution of the ground scene of current global hyperspectral sensors (e.g. SCIAMACHY, 30 km by 60 km) which is satisfactory for open oceans, but limited close to the coasts and at the high latitudes where more factors can influence the retrievals (e.g. CDOM, sea ice, different surface albedos). A second limitation of current global hyperspectral sensors is the revisiting time which in the case of SCIAMACHY is every 6 days. Especially for studies on phytoplankton bloom a data product with better temporal and spatial resolution is required to meet the high spatial and temporal variability of blooms. This issue limits up to now the use of PhytoDOAS products for phenological studies of phytoplankton blooms.

Table 2.4. Potential and limitations of the algorithms described in section 2.3. Based on IOCCG (2014).

Algorithm	Potential	Limitations
PHYSAT	- detection of multiple PFTs - spectral approach - accounts for variability in the spectral response within a PFT	- retrieves the dominant PFT and not concentration - requires large number of match-up between *in situ* and satellite data for algorithm development - implemented for SeaWiFS and MODIS - requires clear sky conditions
ABA	- detection of multiple PFTs and PSCs - retrieves concentration - applicable to any sensor that derives Chla	- based on empirical relationships - requires large *in situ* database for algorithm development - products should not be treated as independent of Chla
PhytoDOAS	- detection of multiple PFTs - retrieves concentration - spectral approach	- does not account for variability in the absorption spectra within a PFT - up to date applied only to SCIAMACHY with low temporal and spatial resolution

2.2 The Southern Ocean dynamics and phytoplankton blooms

2.2.1 Southern Ocean circulation

The SO is of crucial importance for the global climate. The region is unique in that it contains two important circulation features: an important part of the Meridional Overturning Circulation (MOC) and the Antarctic Circumpolar Current (ACC) (Cunningham 2005). These two features are responsible for storing and transporting heat, salt, CO_2, nutrients and other substances, as well as anomalies, around the globe.

The MOC connects all ocean basins through a large-scale system of surface and deep currents (Schmittner et al. 2013). The role of the SO in this system includes the formation of the Antarctic Bottom Water (AABW) and the wind-driven upwelling of deep waters (e.g. North Atlantic Deep

Water – NADW) (Talley 2013). The SO is the major region of the global oceans where the deep waters are upwelled to the surface (Rintoul and Garabato 2013). A conceptual representation of the MOC is presented in Figure 2.6a. The major water masses and pathways are next described based on the works of Rintoul et al. (1999) and Talley (2013).

The NADW, Indian Deep Water (IDW) and Pacific Deep Water (PDW) rise into the mixed layer in the SO where they form the Circumpolar Deep Waters (CDW). The IDW and PDW are less dense than the NADW and upwell above and north of the NADW, being the main source of the upper CDW (UCDW). Part of the UCDW is then diverted northward by Ekman transport across the ACC and leads to the formation of the Subantarctic Mode Water (SAMW).

The SAMW is produced during deep winter convection (Rintoul et al. 1999) and is not only an important source of nutrients for the global oceans (Sarmiento et al. 2004) but it is also rich in anthropogenic CO_2 by air-sea exchange (Sabine et al. 2004). The densest portion of the SAMW further forms the Antarctic Intermediate Waters (AAIW) (Rintoul et al. 1999). The SAWM and AAIW continue flowing northwards into the thermocline and are the main mechanism for transporting anthropogenic CO_2 to the ocean interior (Sabine et al. 2004).

The remaining fraction of the UCDW joins the upwelled lower CDW (LCDW), formed from the NADW. They are then transported southward by eddies and will contribute to the formation of the AABW. The cold winds blowing off Antarctica, over the continental shelves, cause the cooling of ocean surface through heat loss as well as the brine release during the formation of sea ice. These two processes produce dense waters that sink and form the AABW. Main regions for the formation of AABW include the polynyas of the Weddell and Ross Seas. The AABW flows northwards until it rises into IDW, PDW and NADW in the subtropics (Talley 2013).

The zonal circulation of the SO is driven by the ACC. The wind-driven ACC is the strongest current of the global oceans (~ 137 Sv in the Drake Passage, Rintoul et al. 2010), flowing eastward and connecting the southern part of the Atlantic, Indian and Pacific oceans. The ACC transport is constrained into multiple strong narrow jets defined as fronts (Graham and De Boer 2013; Sokolov and Rintoul 2007). The position of the fronts is mainly controlled by the interaction of the flow with the topography (Pollard et al. 2002). Such fronts act as boundaries that split the SO in different zones of waters with distinct characteristics (Cunningham 2005; Sokolov and Rintoul 2007). The main fronts observed in the ACC are: Subantarctic Front (SAF), Polar Front (PF) and Southern Antarctic Circumpolar Front (SACCF) (Figure 2.6b). North of the ACC there is the Subtropical Front (STF), the northern limit of the surface waters SAMW and AAIW (Orsi et al. 1995).
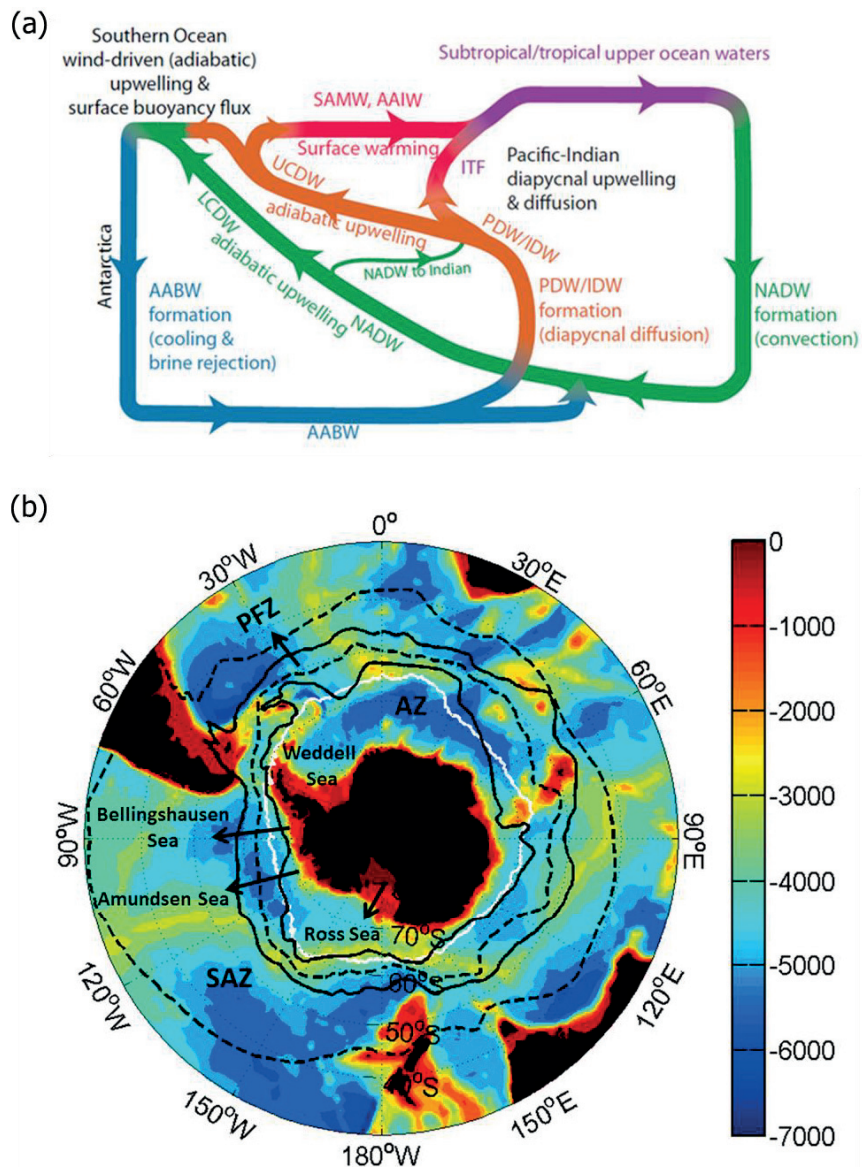
Figure 2.6. (a) Two-dimensional view of the Southern Ocean part of the meridional overturning circulation (MOC). NADW, North Atlantic Deep Water; Indian Deep Water – IDW; Pacific Deep Water – PDW; Indonesian Throughflow – ITF; Upper Circumpolar Deep Water - UCDW; Lower Circumpolar Deep Water - LCDW; Subantarctic Mode Water (SAMW), Antarctic Intermediate Water (AAIW). Adapted from Talley (2013). **(b)** Southern Ocean bathymetry (m) overlaid with the mean position of the maximum sea ice extent (1997-2012, solid white line, Fetterer et al. 2002), Subtropical Front (Orsi et al. 1995) and the Antarctic Circumpolar Current fronts (Orsi et al. 1995, Salle et al. 2008). From north to south: Subtropical Front (STF, dashed line), Subantarctic Front (SAF, solid line), Polar Front (PF, dashed line), and Southern Antarctic Circumpolar Front (SACCF, solid line). SAZ, Subantarctic Zone; PFZ, Polar Front Zone; AZ, Antarctic Zone.

2.2.2 Phytoplankton blooms

The SO is amongst the most productive regions of the global oceans (Comiso 2010; Rousseaux and Gregg 2014). The high seasonal variation of the solar irradiance is the main control of the seasonality of the phytoplankton photosynthesis, growth and distribution (Comiso 2010). Phytoplankton growth is limited in the winter by the reduced sunlight, lower water temperatures and strong vertical mixing. Temperature affects metabolic processes of phytoplankton as well as the stratification of the water column. The convective heat loss in the autumn and winter creates deep mixed layers that dilute the phytoplankton population and rapidly moves phytoplankton through the water column. As a consequence, phytoplankton receive significantly less light than if standing in the euphotic zone and also the grazing pressure is reduced (Behrenfeld and Boss 2014; Franks 2014). Once the solar radiation increases again in spring, the convective mixing is reduced and phytoplankton grow and form blooms, given that sufficient nutrients are available. The following decline of the blooms is controlled not only by the mechanisms above mentioned (light, temperature, deep mixing) but also major factors are the depletion of nutrients and grazing.

Although open waters of the SO are generally characterized by high level of macronutrients, the phytoplankton biomass remains low in many parts of the region, even in the summer when light is normally not limited. The main reason is the lack of the micronutrient iron in the euphotic zone, essential for electron transport in photosynthesis. The SO is a typical high nutrient low chlorophyll (HNLC) system (Falkowski et al. 1998).

Nevertheless, the topography of the SO varies largely (Figure 2.6b) and when the flow associated with the fronts interacts with topographic features, water rich in macro- and micro-nutrients rises to the surface and promotes phytoplankton growth and initiation of blooms. The waters rich in nutrients and in phytoplankton are then advected horizontally with scales of hundreds of kilometers (Sokolov and Rintoul 2007). Additional input of nutrients to the surface occurs by the winter deep mixing, vertical diapycnal diffusion, Ekman upwelling, atmospheric deposition and island's shelf sediments (Borrione et al. 2014; Comiso 2010; Tagliabue et al. 2014). Whereas phytoplankton growth in open waters might be limited by nutrients, the continental shelves of the SO have often higher biomass of phytoplankton. In these regions, nutrients are supplied by river runoff, shelf sediments and melt of ice. In the seasonal ice zone, the area between the minimum and maximum excursion of the sea ice, the increase in phytoplankton biomass follows the retreat of sea ice. An important consequence of the melting of sea ice is the increase of the vertical stratification of the water. At first, the stratification maintains phytoplankton in the upper layers, in the euphotic zone, where nutrients and light promote phytoplankton growth. Also important is that the partial ice cover reduces the mixing of the water column by the winds (Taylor et al. 2013). As sea ice continues to melt, the area of open waters expands. When sea ice has almost disappeared, the wind is able again to mix the water, which in turn dilutes phytoplankton in the water column (Taylor et al. 2013).

2.2.2.1 Hypothesis on phytoplankton bloom initiation

To date, there is a general good understanding on the mechanisms controlling phytoplankton

blooms in high latitudes, but still the mechanisms leading to the start of the spring bloom are discussed. The main hypotheses are briefly introduced below.

2.2.2.1.1 *Sverdrup's Critical Depth Hypothesis*

The Sverdrup's Critical Depth Hypothesis (Sverdrup 1953) is probably the most revisited one. This hypothesis is based on the balance between the net primary production and the rate of losses (respiration, grazing, sinking, mortality) which is controlled by the amount of available light (Franks 2014). The depth where these two processes are equivalent is defined as the critical depth. In the winter, phytoplankton population is diluted and mixed in the deep mixed layer. The respiration exceeds primary production limiting phytoplankton growth and biomass accumulation (Behrenfeld and Boss 2014). In spring, surface heating shoals the mixed layer; phytoplankton are trapped in the surface and exposed to higher light levels. If mixed layer depth is above the critical depth, the production is superior to the losses and concentration begins to rise.

Criticisms to the Critical Depth Hypothesis include the use of a constant loss rate and the density-defined mixed layer depth. Classically, mixed layer depth is defined as the depth at which a density changes by a given threshold value relative to the one at a near-surface (Montegut et al. 2004). Within this mixed layer the water properties are nearly homogeneous and there is a continuous mixing. However, in the Critical Depth Hypothesis there is no differentiation on the strength of the mixing or sinking of phytoplankton (Huisman et al. 2002).

2.2.2.1.2 *Critical Turbulence Hypothesis*

The Critical Turbulence Hypothesis (Huisman et al. 2002) is similar to the Critical Depth Hypothesis, but it differentiates between mixed layer and turbulent mixed layer (Behrenfeld and Boss 2014). The turbulence influences the light levels which phytoplankton are exposed to, as well as the sinking of phytoplankton; hence the development of a bloom depends on the balance in the turbulent mixing rates. If the turbulence is above a minimal threshold, critical turbulence, phytoplankton are diluted and not exposed to light. On the other hand when the turbulence is low, the sinking of phytoplankton out of the euphotic zone dominates and inhibits the development of the bloom similarly. However, at intermediate turbulence phytoplankton are maintained at adequate light levels, the production exceeds the losses and a bloom develops.

2.2.2.1.3 *Disturbance-Recovery-Hypothesis*

The Disturbance-Recovery Hypothesis (Behrenfeld et al. 2013) focus on the role of grazing on controlling the balance between production and loss. According to this hypothesis, the decrease in phytoplankton during autumn and winter is not only caused by the decrease in sunlight, deep mixed layers along with the dilution of phytoplankton, but also by the dilution of zooplankton. Accordingly, the phytoplankton biomass increases with the reduction of phytoplankton-grazers encounters. Thus, the start of the bloom occurs before the shoaling of the mixed layer in spring,

even if the phytoplankton biomass is low due to the dilution by convective mixing (Behrenfeld 2014; Behrenfeld and Boss 2014).

2.3 Climate oscillations and the influence in the Southern Ocean

The phytoplankton biomass and the start, magnitude and duration of blooms vary each year and studies in the SO have suggested that part of this variability is linked to the climate oscillations ENSO and SAM (Alvain et al. 2013; Arrigo and van Dijken 2004; Montes-Hugo et al. 2008; Racault et al. 2012; Smith et al. 2008). Smith et al. (2008), for example, observed a later spring sea-ice retreat and lower phytoplankton biomass offshore in the western Antarctic Peninsula in El Niño or negative SAM events. ENSO and SAM dominate the climate variability on interannual timescales in the tropics and in the SO, respectively. Whereas ENSO is an oscillation of the coupled ocean-atmosphere system, SAM is an oscillation of the atmospheric system.

2.3.1   El Niño Southern Oscillation - ENSO

The ENSO is an ocean-atmosphere phenomenon located in the tropical Pacific ocean that occurs irregularly every 2 to 5 years (Clarke 2008). During neutral years, the surface atmospheric pressure is low in the warmer waters of the western tropical Pacific and high in the colder waters of the central and eastern tropical Pacific. The trade winds that blow eastward tend to pile up the warm waters in the western Pacific forming the "warm pool" (Penland et al. 2013). The warm water pool leads to strong atmospheric convection. The air in higher altitudes moves eastward, sinks over the American continent and returns as easterly winds (Figure 2.7a, Robinson 2010). Neutral years are also characterized by a deeper thermocline in the west side and shallower thermocline in the east side of the Pacific.

In El Niño events anomalous high sea surface temperature (SST) are observed in the eastern tropical Pacific (Figure 2.7b and 2.7d). These higher SSTs are accompanied by lower atmospheric pressure and reduction of the easterly trade winds. With the weakening of the winds the waters of the western Pacific are able to expand eastwards and the warm pool expands. This also creates an anomalous deeper thermocline in the eastern Pacific and shallower in the west Pacific.

In La Niña events the system is reversed and the patterns are similar to normal years, however intensified (Figure 2.7c). The easterly winds are stronger than normal. The SST in the east tropical Pacific is colder than in normal years and the upwelling is intensified (Figure 2.7e).
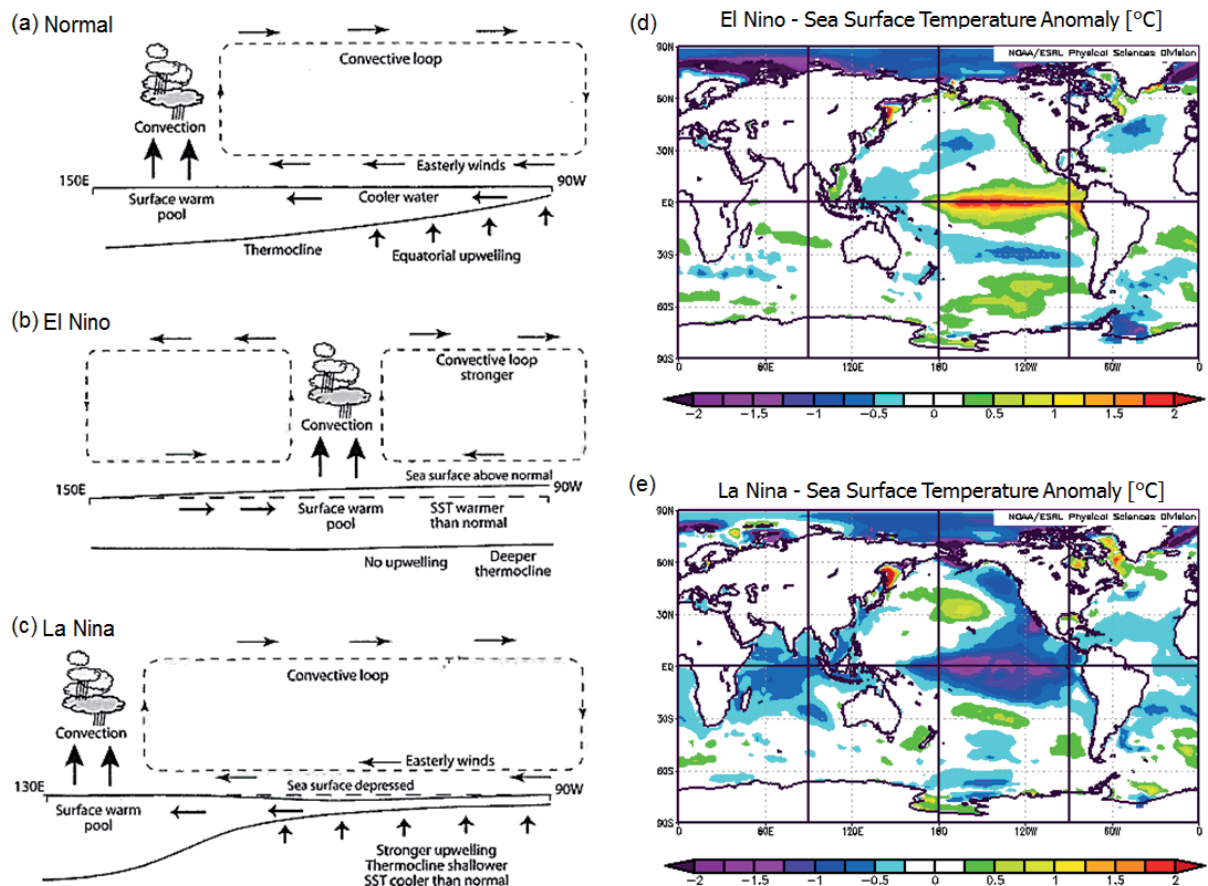
Figure 2.7. On the left: ocean-atmosphere processes that occur during **(a)** normal years, **(b)** El Niño event and **(c)** La Niña event. Modified from Robinson (2010). On the right: composite of anomalies of Sea Surface Temperature from November to March in **(d)** El Niño (1965, 1972, 1982, 1987, 1991, 1993, 1994, 1997, 2002) and **(e)** La Niña (1950, 1955, 1956, 1964, 1971, 1974, 1988, 1998, 1999) events. The maps were produced from the data display pages of the NOAA/ESRL Physical Sciences Division, Boulder Colorado, available at http://www.esrl.noaa.gov/psd/.

The ENSO strongly influences oceanic and atmospheric processes. One of the strongest El Niño was observed in 1982. The upwelling in the coast of Peru was weaker than usual since the thermocline in the region is deeper during El Niño events. As a consequence, less nutrients were available that resulted in a decrease in the phytoplankton biomass with direct impact in the anchovy, sea birds and seals population in the east Pacific region (Clarke 2008).

Although the ENSO is restricted to the tropical Pacific, its effects can be observed in different regions of the globe. Induced changes in sea level pressure, surface air and water temperatures and sea ice cover have been observed in different sectors of the SO (Kwok and Comiso 2002). However, while the teleconnection mechanisms are well established in the tropical Pacific, they are more complex in the SO. The heating in the tropical Pacific ocean and the deep convention generate an atmospheric Rossby wave train that propagates until near Antarctica (Yeo and Kim 2015). In addition to that, the anomalous high SST changes the strength and position of the atmospheric cells and jets that connect the tropics to the SO (Yuan 2004). More information on this topic can be found in the works of Yuan (2004), L'Heureux and Thompson (2006), Ciasto et

al. (2015), Yeo and Kim (2015).

2.3.2   Southern Annular Mode - SAM

The SAM, also known as the Antarctic Oscillation, is the leading mode of atmospheric variability south of 20°S (Pohl et al. 2010). It is characterized by differences in the atmospheric pressure between mid-latitudes and the Antarctic region. A positive phase of SAM consists of anomalous high pressure at mid-latitudes and anomalous low pressure at high latitudes (Figure 2.8a). This pressure difference strengthens and shift the westerly winds around Antarctica (Figure 2.8b). The opposite is observed during a negative phase of SAM.

The influence of SAM has been observed in distinct regions of the SO. The intensified winds during a positive phase of SAM are associated with enhanced Ekman transport in the Antarctic and Polar Frontal Zone (Lovenduski and Gruber 2005). Changes in the sea ice cover have also been observed. Lefebvre et al. (2004) showed that during a positive SAM phase the Bellingshausen and Weddell Seas are influenced by warm northerly winds and the sea ice cover decreases. On the other hand, the Ross and Amundsen Seas are more affected by southerly winds, which increase the sea ice cover.

Moreover, it has been shown that SAM presents a significant trend towards the positive phase in the last decades (Pohl et al. 2010; Sallee et al. 2010). It has also been recognized that ENSO and SAM are not linearly independent at interannual time scales (L'Heureux and Thompson 2006; Pohl et al. 2010). Studies have also shown that El Niño yields to anomaly patterns in ocean and atmosphere similar to a negative phase of SAM, and *vice versa* (Lovenduski 2007; Pohl et al. 2010). Fogt et al. (2011) observed that the teleconnection between ENSO and the SO is intensified when ENSO co-occur with a weak SAM or when both oscillations coincide with opposing phases (e.g. El Niño occurs with a negative SAM phase). When El Niño (La Niña) coincides with positive (negative) SAM phase the magnitude of the teleconnection is reduced.
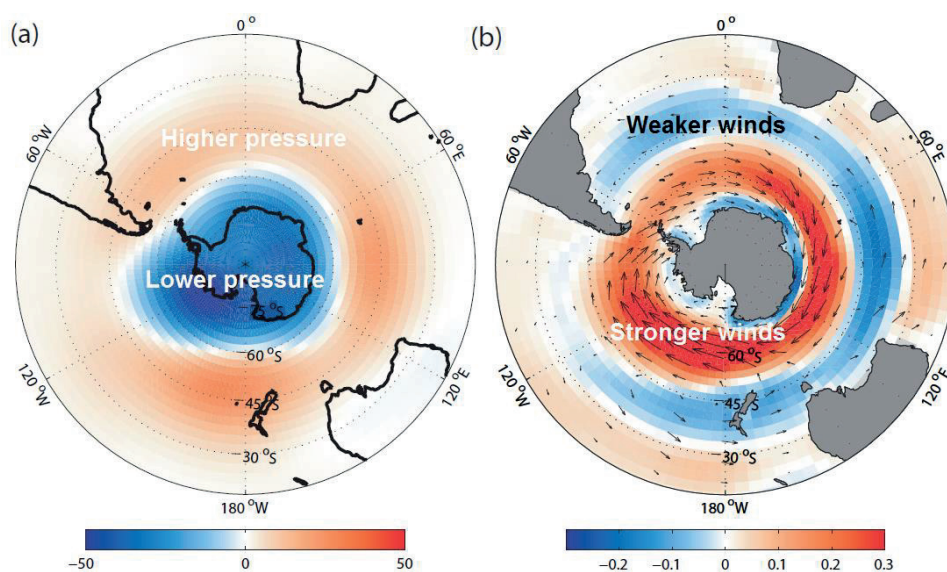
Figure 2.8. Regression of anomaly patterns of **(a)** atmospheric pressure at 700 mb and **(b)** wind stress (dyne cm^{-2}) onto the SAM index. Modified from Lovenduski (2007).

Chapter 3

Satellite derived euphotic depth in the Southern Ocean: implication for primary production modeling

3 Study 1: Satellite derived euphotic depth in the Southern Ocean: implication for primary production modeling

3.1 Motivation

The uncertainty of NPP models can be reduced by improving the input variables (Saba et al. 2011) and a common one, shared by different models (Behrenfeld and Falkowski 1997; Hirawake et al. 2012; Hirawake et al. 2011; Westberry et al. 2008) is the Z_{eu}. However, there is no detailed evaluation of the satellite Z_{eu} in the SO (defined here as the region south of 30°S). A comparison of ocean colour sensor/retrievals with *in situ* measurements, as well as the further impact on the NPP estimation is thus necessary. In this context, the main goal of this chapter is to investigate the differences in estimating Z_{eu} from satellite remote sensing using different approaches and sensors in the SO. We compute Z_{eu} from ocean colour products of (i) Chla and (ii) IOPs and validate those using *in situ* measurements of Z_{eu}. In addition, we compare Z_{eu} derived from the MODIS and the SeaWiFS sensors. The approaches and sensors are further examined in terms of the spatial distribution of Z_{eu}. Since a_{ph} data are used in the NPP calculation, we also examine the uncertainties of MODIS and SeaWiFS a_{ph} derived with the Quasi-Analytical Algorithm (QAA, Lee et al. 2002; Lee et al. 2009). Finally, we apply the absorption based primary production model (ABPM, Hirawake et al. 2012, Hirawake et al. 2011) to investigate how different Z_{eu} products influence the estimation of NPP in the SO.

3.2 Material and Methods

3.2.1 *In situ data*

A dataset of *in situ* measurements of Chla (N=1032) and Z_{eu} (N=1288) in the SO was built to validate the satellite measurements. The dataset compiled measurements from 1997 to 2008 taken by several investigators (Figure 3.1). The Chla data were restricted to Chla derived from HPLC pigment analysis, within 12 m surface layer and taken within 3 hours of the Z_{eu} *in situ* measurements. An average value of Chla was calculated if two or more samples were collected within the surface layer. We used Z_{eu} data provided in the databases that were calculated from *in situ* measurements of vertical profiles of PAR (N=977). In addition, vertical profiles of PAR were also available in the SeaBASS database and those were used to calculate Z_{eu} (N=311). A third dataset of *in situ* measurements of a_{ph} (N=465) was compiled to validate the a_{ph} derived from satellite R_{rs}. The a_{ph} data are derived from filter pad measurements taken in the years 2007, 2008, 2010 and 2012. The ANT-XXVI/3 and ANT-XXVIII/3 data were measured according to the filter pad method described in Taylor et al. (2011). Figure 3.1 presents the relative frequency distribution of the Z_{eu}, Chla and spectrally averaged a_{ph} coefficient over 400–700 nm ($\bar{a}_{ph}$, see section 3.4) *in situ* measurements that matched with SeaWiFS and MODIS data.
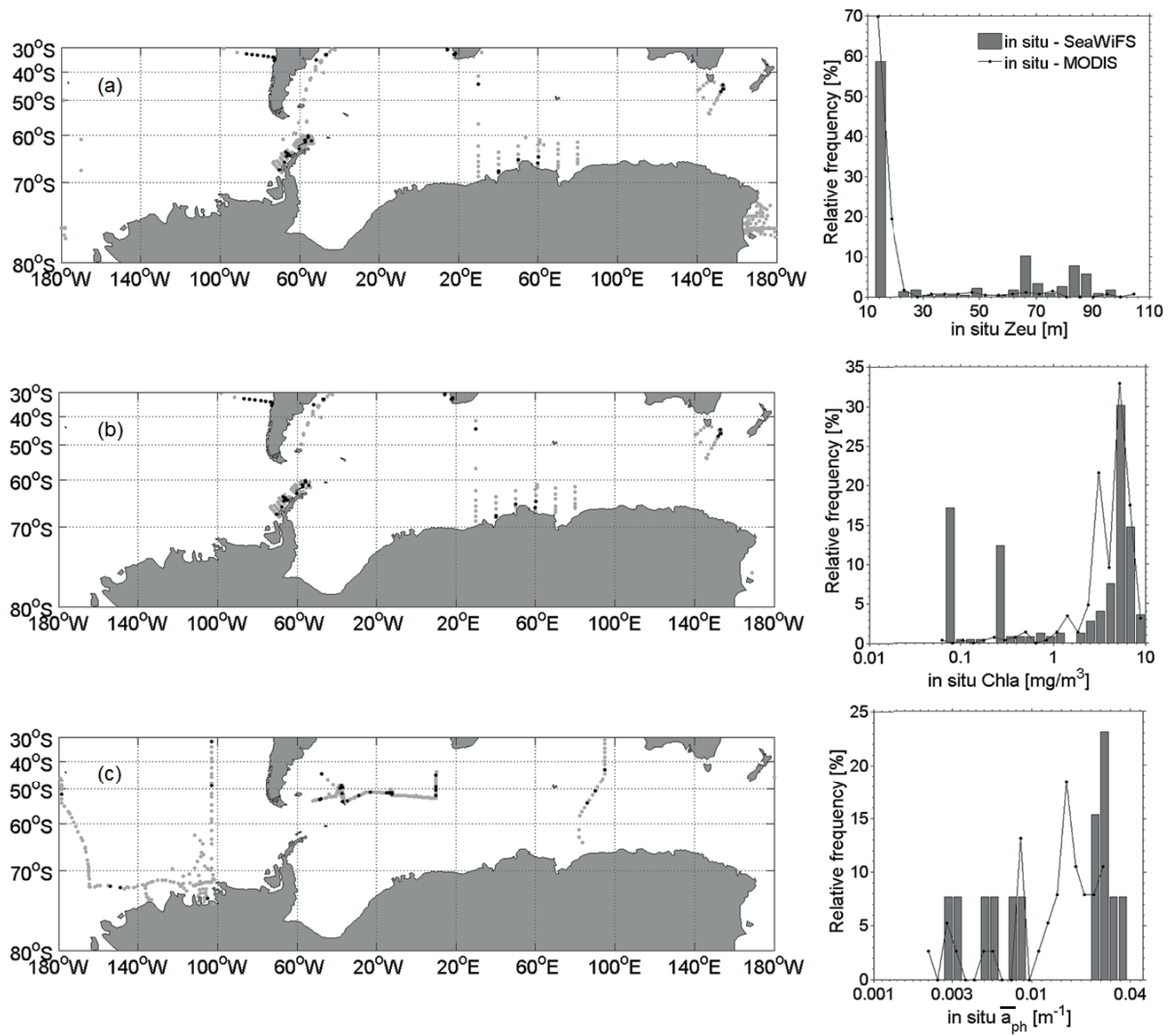
Figure 3.1. On the left, location of the *in situ* measurements in light grey and the matched ones with satellite in black: **(a)** Z_{eu} (1288), **(b)** Chla (1032) and **(c)** $a_{ph}(\bar{a}_{ph})$ (465). On the right, the respective relative frequency distribution of the matched *in situ* measurements.

3.2.2   Satellite data

MODIS-Aqua (R2012.0) and SeaWiFS (R2010.0) level 3 products of Chla (CHL1), PAR, R_{rs} were obtained at http://oceancolor.gsfc.nasa.gov/. The data are produced and distributed by the NASA Goddard Space Flight Center's Ocean Data Processing System (ODPS). The SeaWiFS dataset has the longest time series; however, the data acquisition ended in December 2010. We used MODIS and SeaWiFS data at 9 x 9 km² spatial resolution. Satellite PAR and a_{ph} (see section 3.2.4) derived from R_{rs} were used in the NPP model. For the validation with *in situ* measurements daily images were used; for spatial distribution analysis we used monthly data.

3.2.3 Z_{eu} derived from ocean colour

Two approaches were used to derive Z_{eu} from ocean colour products of: (i) Chla (Z_{eu}-Chla) and (ii) IOPs (Z_{eu}-IOP), as presented in section 2.1.3. The QAA (version 5, Lee et al. 2009) was applied to derive the absorption and backscattering coefficients at 490 nm ($a490$ and b_b490) from the satellite R_{rs}. The detailed QAA for the retrieval of $a490$ and b_b490 and of Z_{eu} was presented in chapter 2 (section 2.1.2). The uncertainties of the IOPs retrieved from QAA are discussed in Lee et al. (2005) and Lee et al. (2006; 2010).

3.2.4 Primary production model

The NPP was calculated using the Absorption Based Primary Production Model (ABPM, Hirawake et al. 2012; Hirawake et al. 2011), an improved version of the Vertically Generalized Production Model (Behrenfeld and Falkowski, 1997) for polar oceans. In the ABPM, the product of the chlorophyll-*a* normalized maximum photosynthetic rate in the water column (P_{opt}^B, mg C (mg Chla)$^{-1}$ h^{-1}) and Chla (mg m^{-3}) is replaced by a linear relation of the spectrally averaged a_{ph} coefficient over 400–700 nm ($\bar{a}_{ph}$, m^{-1}). This model eliminates uncertainties of the satellite Chla product and the temperature effect on the estimation of the P_{opt}^B (Hirawake et al. 2011). The ABPM is expressed as:

$$NPP = \left(109.66\, \bar{a}_{ph}(0^-) - 0.02\right) \frac{0.66125 \cdot E_0}{E_0 + 4.1} Z_{eu}\, D_{irr} \qquad (3.1)$$

where E_0 is the daily integrated photosynthetic available radiation (PAR, Einsteins m^{-2} day^{-1}) from satellite and D_{irr} is the photoperiod (h) calculated as described in http://orca.science.oregonstate.edu/faq01.php. The NPP estimated from Z_{eu}-Chla is represented as NPP-Z_{eu}-Chla and from Z_{eu}-IOP as NPP-Z_{eu}-IOP.

The QAA was applied to derive the a_{ph} at the SeaWiFS spectral bands of 412, 443, 490, 510 and 555 nm and MODIS spectral bands of 412, 443, 488, 531 and 555 nm. Satellite $\bar{a}_{ph}$ were then derived by adjusting the a_{ph} integrated over the visible bands of SeaWiFS and MODIS to the *in situ* $\bar{a}_{ph}$ over the continuous visible range (400 – 700 nm) (Hirawake et al. 2012, Hirawake et al. 2011):

$$\bar{a}_{ph}(0^-) = \frac{a \sum_{N=1}^{4}\left[\left(a_{ph}(\lambda_{i+1}) + a_{ph}(\lambda_i)\right)\left(\left(\lambda_{i+1} - \lambda_i\right)/2\right)\right]}{700 - 400} \qquad (3.2)$$

where λ were the above mentioned spectral bands of SeaWiFS and MODIS. The parameter *a* represents the slope of the regression of the satellite $\bar{a}_{ph}$ to the *in situ* $\bar{a}_{ph}$ and corresponded to 1.3656 for SeaWiFS and 1.5354 for MODIS.

3.2.5 Validation and statistical analysis

The MODIS and SeaWiFS match ups were obtained when the day, latitude and longitude of the *in situ* observation fell within the limits of 1x1 pixel. The bias, average absolute percentage of error (*E*), root-mean-square error (RMSE) and mean absolute error (MAE) were calculated to evaluate the differences between the *in situ* Z_{eu} and the satellite Z_{eu}:

$$log_{10}\text{bias} = \frac{1}{N}\sum_{i=1}^{N}(log_{10}(Y_i) - log_{10}(X_i)) \tag{3.3}$$

$$E = \left(\frac{1}{N}\sum_{i=1}^{N}\left|\frac{Y_i - X_i}{X_i}\right|\right) 100\% \tag{3.4}$$

$$log_{10}\text{RMSE} = \sqrt{\frac{1}{N}\sum_{i=1}^{N}(log_{10}(Y_i) - log_{10}(X_i))^2} \tag{3.5}$$

$$log_{10}\text{MAE} = \frac{1}{N}\sum_{i=1}^{N}|(log_{10}(Y_i) - log_{10}(X_i))| \tag{3.6}$$

where *X* was the *in situ* value, *Y* the satellite value and *N* is the number of matching pairs. The statistical indicators log_{10}bias, *E* and log_{10}RMSE were chosen based on the GlobColour Validation Report (Durand 2007) and other literatures on satellite validation (Shang et al. 2011b; Zibordi et al. 2006). The log_{10}MAE was used as a statistical estimator of error for comparisons between the sensors and a_{ph} at different wavelengths, since *N* changes. Willmott and Matsuura (2005) showed that RMSE is sensitive to the square root of *N* and MAE should be preferred instead. No outliers were removed. For reference, a 1:1 line was included in the scatterplots to show how well the satellite and *in situ* data agree.

Monthly climatologies of Z_{eu} and NPP in December, January and February, were computed to investigate spatial differences. The climatology fields were calculated from monthly images for the 2003-2009 period, excluding the year of 2008 when SeaWiFS did not acquire data. For each pixel, the relative difference between the spatial fields was derived:

$$\text{DIFF} = \left(\frac{A-B}{B}\right) 100\% \tag{3.7}$$

where A corresponded to Z_{eu}-Chla, Z_{eu}-SWF or NPP-Z_{eu}-Chla and B to Z_{eu}-IOP, Z_{eu}-MODIS or NPP-Z_{eu}-IOP. We did not compare the spatial distribution of NPP between the sensors because $\bar{a}_{ph}$, PAR and Chla might introduce differences in the NPP estimation.

3.3 Results

3.3.1 Comparison of satellite and in situ Z_{eu}

Figure 3.2 presents the comparison between satellite and *in situ* Z_{eu}. The overall statistics show that the two approaches agree well with the *in situ* measurements. When Z_{eu}-SWF was derived by the IOP approach, the statistics are slightly better than Z_{eu}-Chla improving the *E* in 3.5% (Figures 3.2a and b) and the regression line is close to the 1:1 line (dotted line). On the other hand, Z_{eu}-Chla shows better results than Z_{eu}-IOP for MODIS, reducing the *E* in 9.5% (Figures 3.3c and d). Differences in $\log_{10}$MAE indicate that Z_{eu} retrieved from SeaWiFS is more accurate than MODIS. Negative biases are found for Z_{eu}-MODIS and positive biases for Z_{eu}-SWF.
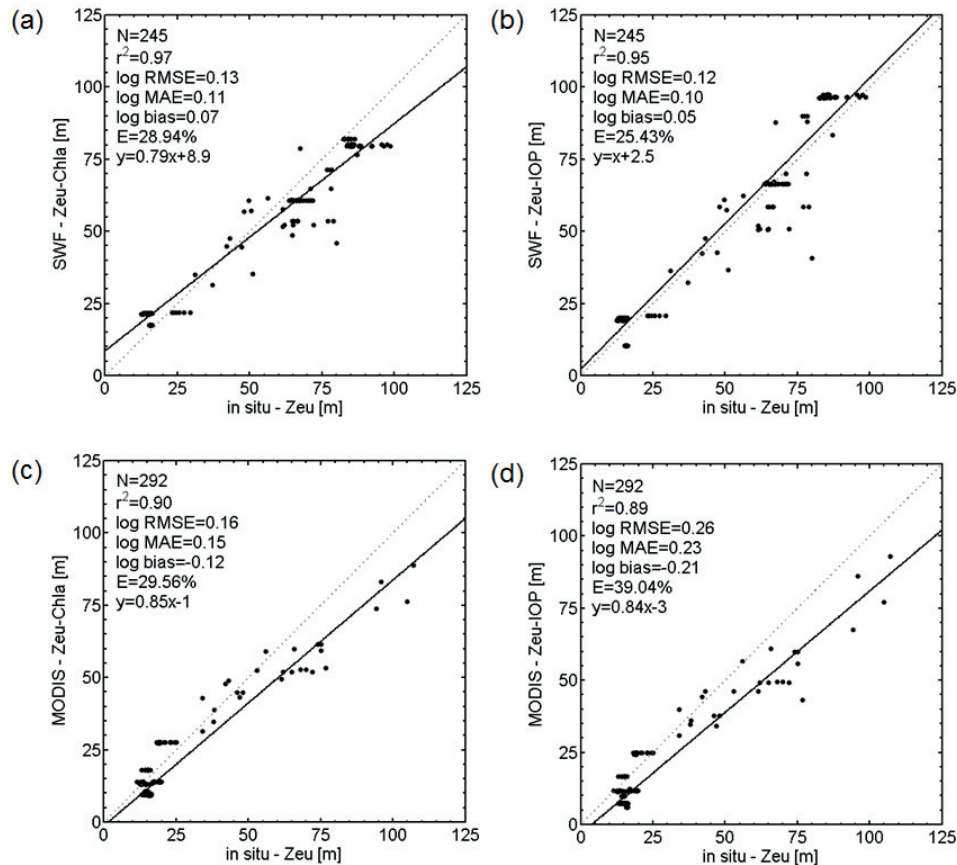
Figure 3.2. Scatterplots of satellite Z_{eu} against *in situ* Z_{eu}. **(a)** and **(c)** Z_{eu} is derived from Chla approach (Z_{eu}-Chla), **(b)** and **(d)** Z_{eu} is derived from the IOP approach (Z_{eu}-IOP). The solid line represents the regression and the dotted line represents 1:1 line as reference.

Compared to collocated *in situ* HPLC Chla data of our validation dataset, the standard SeaWiFS algorithm (OC4v.6) underestimates Chla (Figure 3.3). For MODIS, the OC3M algorithm leads to under- and overestimation of Chla depending on the concentration of the *in situ* Chla. For *in situ* Chla < 1.5 mg m^{-3}, Chla was on average underestimated, whereas for higher concentrations (> 1.5 mg m^{-3}) the retrievals were overestimating the *in situ* values.

50
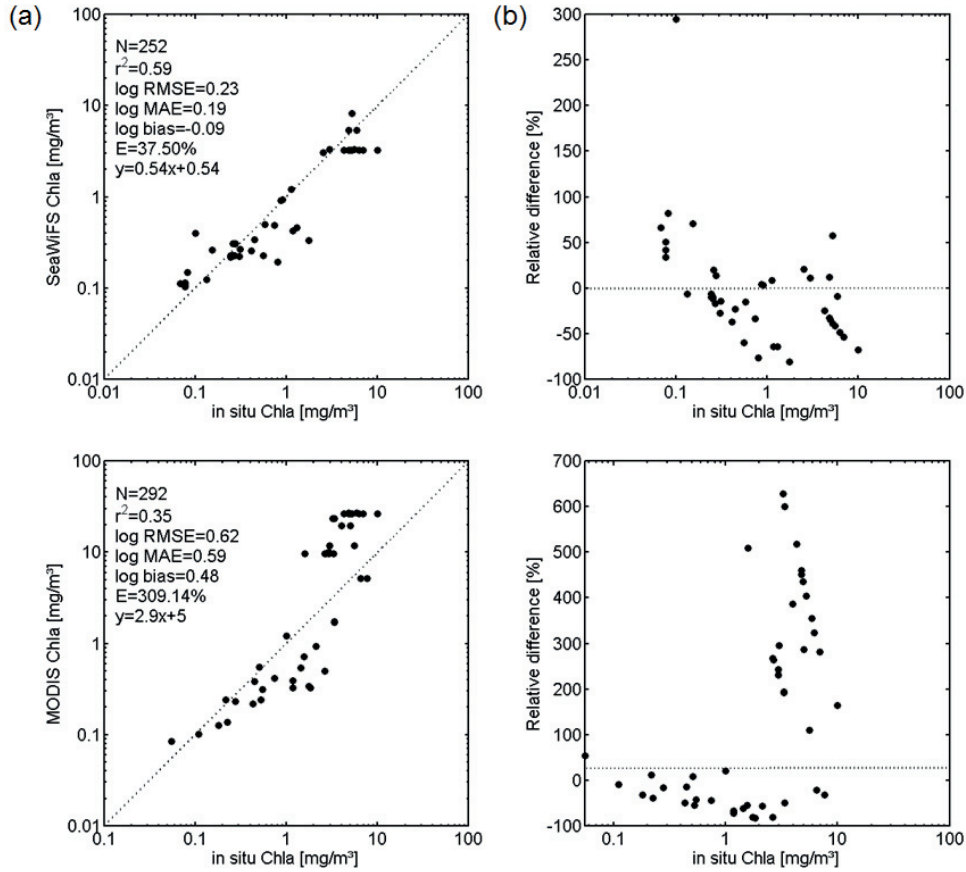
Figure 3.3. (a) Scatterplots of satellite and *in situ* Chla. The dotted line represents the 1:1 line as reference. **(b)** Relative differences between satellite Chla and *in situ* Chla. The dotted line represents the zero line.

3.3.2   Spatial distribution of Z_{eu}-Chla and Z_{eu}-IOP

Figure 3.4 presents the spatial distribution of the climatology of Z_{eu} for February, using data from 2003 to 2009. Deeper Z_{eu} are associated with oligotrophic waters in the zonal band of 30° - 40°S. Shallower Z_{eu} are observed in the waters around the Antarctic continent, South America, south and west part of South Africa and between 40° - 50°S, except for the eastern Pacific Sector. Shallower Z_{eu} are related to terrigenous influence (e.g. La Plata river plume in the Patagonian Shelf region) and higher chlorophyll concentrations in upwelling regions (e.g. Benguela upwelling), islands (e.g. Kerguelen islands) and continental shelves (e.g. Antarctic Peninsula). The difference in calculating the climatology of Z_{eu} from daily or monthly images was small. For instance, the standard deviations of the difference between Z_{eu}-Chla calculated from daily data and monthly data in February 2003 are 1.22 m for SWF and 1.08 m for MODIS. For the IOP approach the values are 0.91 m for SeaWiFS and 0.77 m for MODIS.

When Z_{eu}-Chla was compared with Z_{eu}-IOP, large differences were observed. While the range of Z_{eu}-Chla from SeaWiFS varies between 5.97 and 234.31 m (median = 65.50 m), using the IOP approach this range is much narrower, from 2.5 to 150 m (median = 63.93 m). Similar for MODIS, Z_{eu}-Chla varies between 5.89 and 259.69 m (median = 65.50 m) and Z_{eu}-IOP from 3.5 to

51

146.3 m (median = 62.37 m). On average, for the entire region, Z_{eu}-Chla from SeaWiFS and MODIS are 3.61 and 5.41% deeper than Z_{eu}-IOP. These differences followed a zonal distribution. The most notable difference was observed in the Pacific Sector within the 30°- 40°S zonal band, corresponding to the South Pacific subtropical gyre, where Z_{eu}-Chla is ~ 20 - 30% deeper than Z_{eu}-IOP. The spatial distribution maps also pointed out differences of about 10 - 15% south of 60°S, with Z_{eu}-Chla usually deeper than Z_{eu}-IOP; especially for MODIS. Regions corresponding to deeper Z_{eu}-IOP were also presented, but they were less abundant and only about ~ 10% deeper.
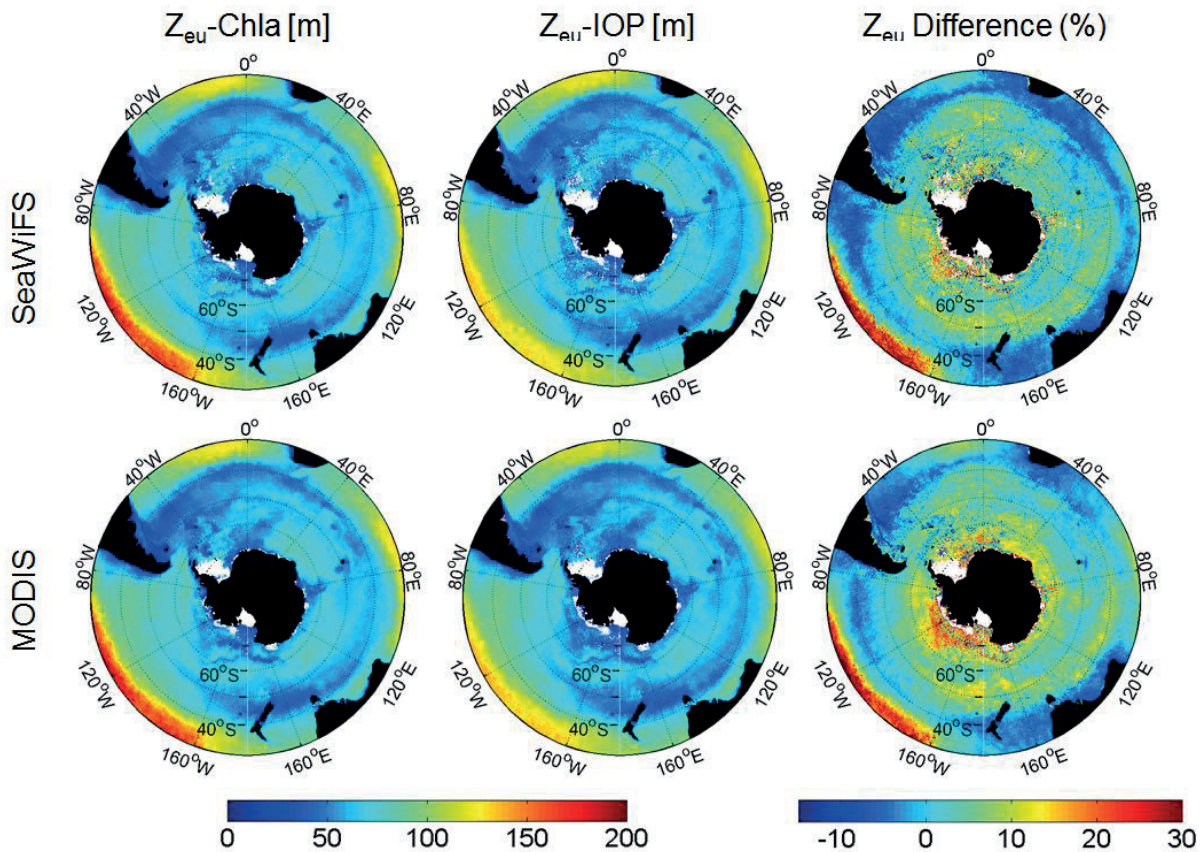
Figure 3.4. Spatial distribution of Z_{eu} in the Southern Ocean (climatology of February). The white pixels correspond to areas with no data.

Comparing the sensors, the spatial distribution of Z_{eu} is similar in both approaches, with an average difference (DIFF) of -0.005 and 2.68% for Z_{eu}-Chla and Z_{eu}-IOP, respectively in February (Figure 3.5). However, the spatial differences are larger south of 60°S and more evident in Z_{eu}-IOP. A corresponding pattern was observed in December and January.
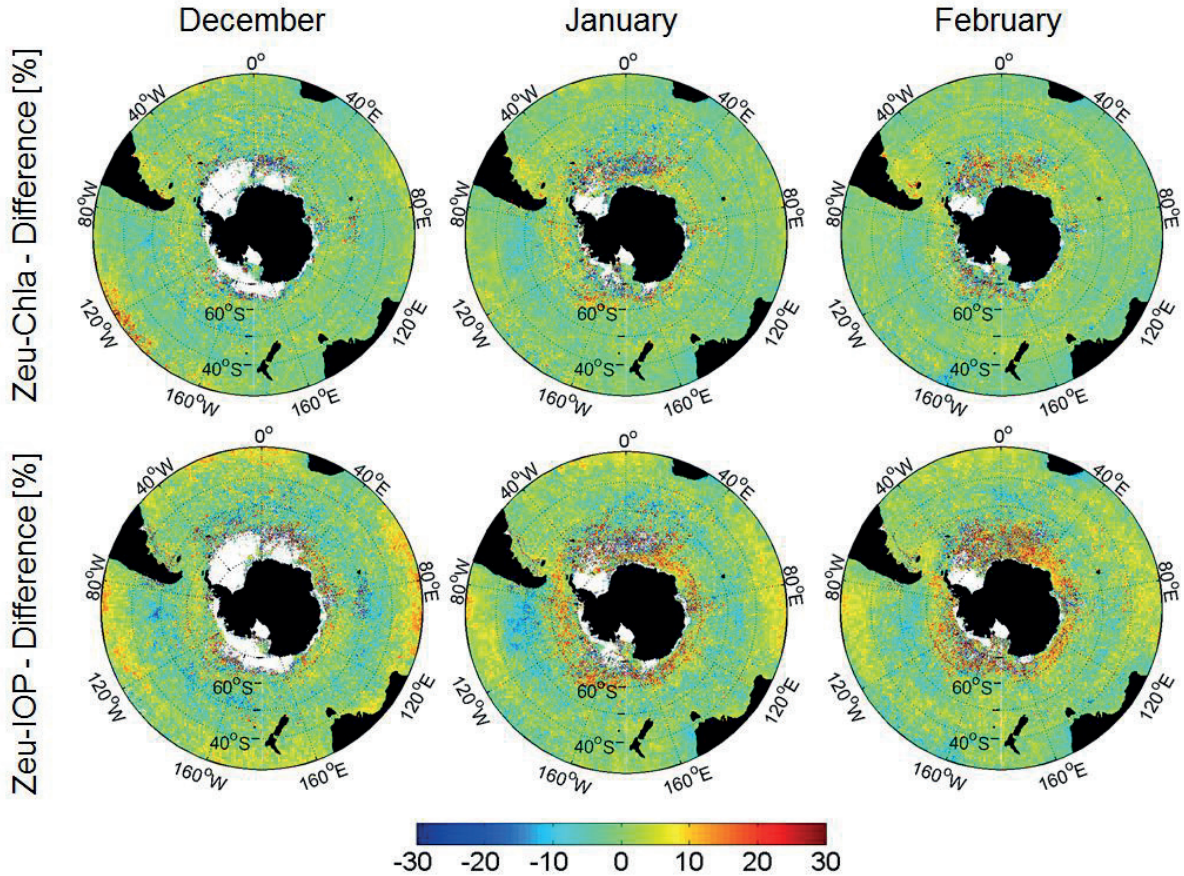
Figure 3.5. Spatial distribution of the relative percentage of difference between SeaWiFS and MODIS. The white pixels correspond to areas with no data.

3.3.3 Primary Production

3.3.3.1 Validation of SeaWiFS and MODIS derived a_{ph}

The ocean colour NPP model used here is a function of $\bar{a}_{ph}$. The $\bar{a}_{ph}$ can be determined empirically through linear relations between *in situ* $\bar{a}_{ph}$ and satellite a_{ph} integrated over the visible spectral bands of SeaWiFS and MODIS. Hirawake et al. (2012; 2011) calculated these relationships based on a_{ph} derived from ship R_{rs} at the MODIS and SeaWiFS spectral bands, using the QAA. However, within this study the satellite R_{rs} derived a_{ph} were not validated due to the insufficient number of collocations between satellite and *in situ* data. Furthermore, at the current state of knowledge, there is no information on the performance of the QAA to derive a_{ph} from satellite R_{rs} in the SO. Therefore, before we investigated the NPP, we briefly assessed the quality of the a_{ph} derived from SeaWiFS and MODIS R_{rs} using the QAA with *in situ* a_{ph}. Results are presented in Table 3.1.

The E of a_{ph}-SWF increase for increasing wavelengths (except at 443 nm) and negative biases indicate an underestimation of a_{ph}. Results for MODIS show similar $\log_{10}$MAE at 412, 443 and

488 nm, increasing towards 550 nm. Negative a_{ph} were retrieved at SeaWiFS bands 490, 510 and 555 and at MODIS bands 412 and 443 nm and lead to small but negative $\bar{a}_{ph}$. Those values were removed before the calculation of the statistics presented in Table 3.1. Estimates of NPP on pixels with negative $\bar{a}_{ph}$ were removed as well.

Table 3.1. Statistical results of the comparison between QAA-satellite derived a_{ph} and *in situ* $a_{ph.}$

SeaWiFS (N=12)					Range				
Wavelength (nm)	r^2	$\log_{10}$MAE	$\log_{10}$bias	E (%)	satellite			*in situ*	
412 (N=12)	0.81	0.22	-0.20	38.26	0.002	- 0.15	0.001	- 0.110
443 (N=12)	0.57	0.20	-0.15	36.97	0.003	- 0.171	0.011	- 0.092
490 (N=11)	0.19	0.20	-0.12	44.71	0.008	- 0.119	0.011	- 0.056
510 (N=11)	0.06	0.40	-0.32	71.78	0.001	- 0.083	0.006	- 0.054
555 (N=11)	0.37	0.36	-0.29	60.15	0.0003	- 0.042	0.001	- 0.02
$\bar{a}_{ph}$ (N=11)	0.48	0.20	-0.15	39.29	0.005	- 0.076	0.006	- 0.04
MODIS (N=36)								
412 (N=34)	0.48	0.17	-0.08	36.53	0.002	- 0.066	0.001	- 0.056
443 (N=34)	0.49	0.15	-0.04	33.93	0.003	- 0.079	0.002	- 0.064
488 (N=36)	0.52	0.16	-0.08	29.03	0.0005	- 0.05	0.001	- 0.047
531 (N=36)	0.48	0.23	0.005	98.53	0.001	- 0.025	0.0001	- 0.025
550 (N=36)	0.29	0.41	0.41	220.34	0.009	- 0.025	0.0	- 0.014
$\bar{a}_{ph}$ (N=34)	0.58	0.14	0.04	43.46	0.002	- 0.038	0.0005	- 0.029

3.3.3.2 *Spatial distribution of NPP-Z_{eu}-Chla and NPP-Z_{eu}-IOP*

Generally, higher NPP-Z_{eu}-Chla than NPP-Z_{eu}-IOP were observed using both sensors over the SO (Figure 3.6). For SeaWiFS NPP-Z_{eu}-Chla was 7% higher than NPP-Z_{eu}-IOP and for MODIS 10.22% higher. The average of NPP-Z_{eu}-Chla and NPP-Z_{eu}-IOP were 321.18 and 283.84 mg C m^{-2} d^{-1} for SeaWiFS, respectively. Using MODIS data the NPP-Z_{eu}-Chla and NPP-Z_{eu}-IOP were 438.50 and 393.78 mg C m^{-2} d^{-1}, respectively. Although these differences may not be significant for studies focusing on the entire SO, for local comparisons they are relevant. For instance, in the region south of 60°S (60°S – 80°S, 120°W – 160°W) NPP-Z_{eu}-Chla was ~ 30% higher than NPP-Z_{eu}-IOP.
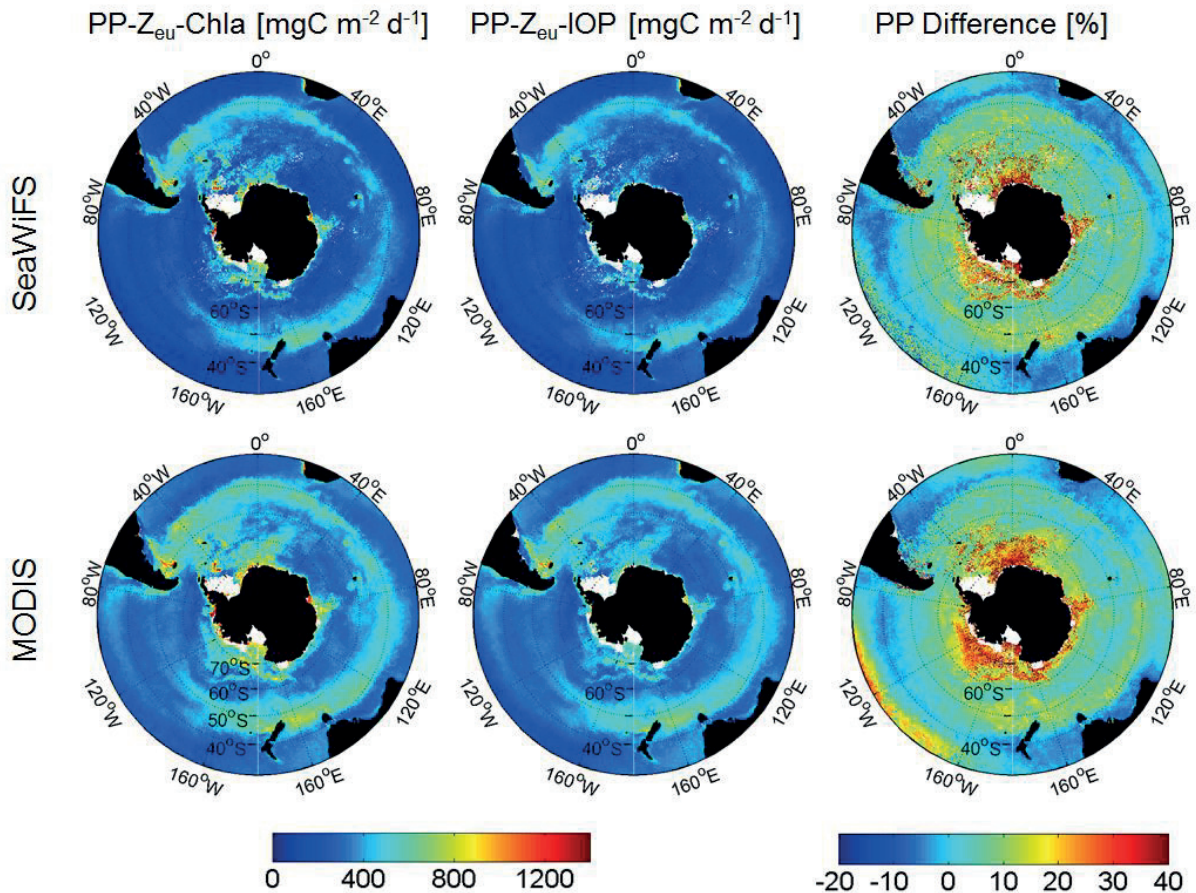
Figure 3.6. Spatial distribution of net primary production (in the figure caption called PP) in the Southern Ocean (climatology of February). NPP-Z_{eu}-Chla (left), NPP-Z_{eu}-IOP (right) and relative percentage of difference between NPP-Z_{eu}-Chla and NPP-Z_{eu}-IOP (center). The white pixels correspond to areas with no data.

3.4   Discussion

3.4.1   *Validation of Z_{eu} and Chla*

This study investigated differences between two approaches to derive satellite Z_{eu}: the first one by Morel (in Lee et al. 2007) is empirical and based on Chla and the second one by Lee et al. (2005) is semi-analytical and based on IOPs. We focused on the Chla approach because of its simplicity, but also to investigate if the known inaccuracy of the standard satellite Chla products in the SO would impact the Z_{eu} retrieval. The SO is heterogeneous in terms of bio-optical conditions. It comprises not only oligotrophic waters, but ultra-oligotrophic waters (e.g. South Pacific Gyre), complex waters (e.g. high concentration of non-algal particles in the Patagonia Shelf), upwelling regions (e.g. Benguela upwelling), polar fronts and coastal Antarctic waters (e.g. Antarctic Peninsula). For this reason, we included a more complex approach in our investigation: the IOP approach, which accounts for the vertical distribution of other in-water components that also contribute to the light attenuation. The QAA can be applied globally, regardless of the optical

complexity of the water and has been widely used and cited in the literature.

Our validation dataset covered a wide range of bio-optical conditions (Figure 3.1); however uncertainties in Z_{eu} were only improved by the IOP approach for SeaWiFS (Figure 3.2). This observation agrees with Lee et al. (2007). The authors compared *in situ* Z_{eu} with Z_{eu}-Chla and Z_{eu}-IOP calculated from ship borne R_{rs} in the Monterey Bay, the Gulf of Mexico and the Arabian Sea and reported improved Z_{eu} from the IOP approach. In addition, Shang et al. (2011b) studied oligotrophic and coastal waters of the South China Sea using MODIS data and showed that Z_{eu}-IOP was more accurate than empirically deriving Z_{eu} from Chla (Morel et al. 2007). Within MODIS data, our Z_{eu} estimation with the Chla approach yielded better results than the IOP approach.

Our results indicate that Z_{eu} can be accurately estimated by both approaches and sensors with a $\log_{10}$MAE within 0.10 and 0.23 m. The relative consistency observed between the sensors is related to the common processing schemes applied, such as the atmospheric correction and data binning, as already pointed out by Mélin (2011). Differences might be caused by the different coverage of areas, spectral bands, orbital characteristics and equator-crossing times. MODIS-Aqua crosses the equator at 13:30 pm. For SeaWiFS the equator crossing time drifted throughout the mission, from 12:00 to 14:20, but 12:30 pm was used for calculations. Additional sources of error in the validation analysis include the *in situ* measurements, as the use of different field sensors and data/sample processing.

Results of the Chla validation indicate that the satellite Chla products from SeaWiFS are more accurate than from MODIS in the SO (Figure 3.3). Our MODIS validation dataset is, however, biased towards high Chla waters (Figure 3.1); 95% of the *in situ* data had Chla > 1 mg m^{-3} where the errors are generally higher as well. In contrast, the SeaWiFS validation dataset has only 65% of samples at Chla > 1 mg m^{-3}. For instance, the difference in the $\log_{10}$MAE between MODIS and SeaWiFS for Chla < 1 mg m^{-3} is 0.02 mg m^{-3} (0.17 mg m^{-3} for MODIS and 0.15 mg m^{-3} for SeaWiFS); for higher concentrations this difference increases to 0.4 mg m^{-3} (0.61 mg m^{-3} for MODIS and 0.21 mg m^{-3} for SeaWiFS). The observed underestimation of Chla by the operational SeaWiFS and MODIS algorithms (here only for Chla < 1.5 mg m^{-3}) is in accordance with previous studies that used earlier algorithm versions, indicating that this issue still persists in the SO (Dierssen and Smith 2000; Garcia et al. 2005; Johnson et al. 2013; Kahru and Mitchell 2010; Szeto et al. 2011). Further, it is important to mention that we used surface Chla instead of the weighted Chla in the first optical depth. Our coincident *in situ* measurements of HPLC Chla profiles, Kd and Z_{eu} were all concentrated in the Antarctic Peninsula region which represents a particular region of the SO, thus we used surface Chla values only. Moreover, we avoided the use of fluorometric data in our study and used HPLC data. Marrari et al. (2006) showed that the chlorophyll fluorescence of accessory pigments (e.g. chlorophyll-b) interferes in the determination of Chla by fluorometric methods in the SO.

Nevertheless, uncertainties of the satellite Chla have some but small influence on the Z_{eu}-Chla, which is in part linked to the nature of the power function that empirically relates Z_{eu} to Chla. One has to note that we used the Chla even in waters that hardly fit to the Case 1 assumption, for instance on the Patagonian shelf and around the Antarctic Peninsula (Dierssen and Smith 2000; Garcia et al. 2005). The error in Z_{eu} induced by the error in Chla depends on the *in situ* concentrations. A 100% error in lower Chla values has higher impact on Z_{eu} than 100% error in high Chla values. For instance, a 100% overestimation in the lowest and highest *in situ* Chla (0.05 mg m^{-3}

and 9.98 mg m^{-3}) of our SeaWiFS validation dataset would lead to an error of 26.79 and 2.82 m in Z_{eu}, respectively.

3.4.2 Z_{eu} spatial distribution

The spatial distribution maps of Z_{eu}-Chla and Z_{eu}-IOP highlighted large differences in the South Pacific subtropical gyre and south of 60°S (Figure 3.4). Morel et al. (2007) evaluated the Chla approach for waters of the South Pacific subtropical gyre with data collected during the BIOSOPE cruise and showed that an empirical relationship based on Chla (Morel and Gentili 2004) was valid to estimate Z_{eu} in those waters. Thus, for this region the satellite Z_{eu}-Chla may be the better choice. Unfortunately, beside the data from the BIOSOPE cruise, there were no *in situ* measurements of Z_{eu} available from the South Pacific and other SO subtropical gyres for a detailed investigation. Our comparison between satellite and *in situ* Z_{eu} for data south of 60°S did not show significant differences between the approaches for SeaWiFS and slightly better estimates of Z_{eu}-Chla for MODIS (Figure A1). Overall, Z_{eu}-IOP was shallower than Z_{eu}-Chla, as observed by Lee et al. (2007) for other oceanic regions.

Although the spatial distribution of Z_{eu} is consistent, it is important to mention that close to the Antarctic continent the values might be impacted by ice contamination. Pixels contaminated by cloud/ice and straylight are flagged in the Level-3 data. Nevertheless, Belanger et al. (2007) and Wang and Shi (2009) showed that the standard SeaWiFS and MODIS flags may not remove all pixels impacted by the adjacency effect, sub-pixel ice and mixed ice-water contamination. Based on radiative transfer simulations Belanger et al. (2007) showed the significant impact of the adjacency effect and sub-pixel ice contamination on the water leaving radiance and derived Chla and IOP products. In general, the sub-pixel contamination leads to an overestimation of Chla and the total absorption at 443 nm (a_{443}). The adjacency effect overestimates Chla in low Chla waters (0.05 mg m^{-3}) and for Chla > 0.5 mg m^{-3}, a_{443} and Chla retrievals are underestimated. Wang and Shi (2009) observed that MODIS Chla is often overestimated in sea ice contaminated pixels. Therefore, both shallower and deeper Z_{eu} regions observed close to the Antarctic continent might be biased.

In addition, when comparing the sensors, the spatial differences were larger close to the sea ice edge and were likely related to the few pixels sampled at different times (Figure 3.5). These differences were as large as 20% and more pronounced in the Z_{eu}-IOP, which might be explained by the following reasons. The IOP approach is probably more influenced by the atmospheric correction since the QAA uses the 670 nm band to derive the total absorption at the reference wavelength. The 670 nm band is important for the retrievals of IOPs from R_{rs} in high-absorption waters (Lee at al. 2006, Lee at al. 2007). At 670 nm water absorption dominates and the signal to noise ratio is low, which in turn leads to a high sensitivity to light conditions. This is also the most likely reason for the large differences seen south of 60°S (Figures 3.4 and 3.5). Moreover, differences between Z_{eu}-SWF and Z_{eu}-MODIS might be associated to changes in the QAA depending on the sensor used. Examples of the QAA adjustment to sensors are the difference in reference wavelength (555 nm for SeaWiFS and 550 nm for MODIS) and the constants used to derive total absorption at the reference wavelength. These are based on relations to a different set

of collocations and the solar zenith angle. An alternative is the use of merged products (e.g. GlobColour, OC-CCI), aimed to reduce discrepancies caused by the use of different sensors as observed here.

3.4.3   Validation of a_{ph}

The assessment of MODIS and SeaWiFS QAA-derived a_{ph} is presented in Table 3.1. The comparison of R_{rs}-satellite and *in situ* a_{ph} shows satisfactory results in terms of $\log_{10}$MAE for both sensors at 412 and 443 nm, and at 488 and 531 for MODIS. The percentage differences are higher than the values presented by Lee at al. (2011). Nevertheless, Lee at al. (2011) derived a_{ph} from ship borne R_{rs} instead of satellite $R_{rs;}$ larger uncertainties would be expected in satellite R_{rs}.

The E of a_{ph}-MODIS at 412 and 443 is comparable to the values reported by Shang et al. (2011a) when evaluating QAA-derived a_{ph} from satellite MODIS R_{rs} in the Taiwan Strait as well. At 488 nm the error is lower. Generally, a_{ph}-MODIS showed lower $\log_{10}$bias and $\log_{10}$MAE than a_{ph}-SWF for the same wavelengths. Further, the comparison of $\log_{10}$MAE from the Chla and a_{ph}443 validations suggested improvement of a_{ph}443 over Chla in the SO for MODIS, as observed by Shang et al. (2011a) in the Taiwan Strait.

Uncertainties in the validation of the satellite a_{ph} could be introduced by error in the *in situ* measurements of a_{ph}, as well as in the satellite R_{rs} and in the estimation of *gelbstoff* absorption by the QAA (Lee et al. 2006; Lee et al. 2011; Shang et al. 2011a). Unfortunately, it is beyond the scope of this study to propose modifications in the algorithm for the SO. Hirawake et al. (2011) modified the QAA based on underwater spectral radiation data and *in situ* a_{ph} from the Indian Sector of the SO. This modified QAA was also tested by us, but the results were less robust than with the original QAA (results not shown). In part, regional differences across the SO, as discussed above and as seen in the Z_{eu}, make it difficult to extrapolate local properties to the entire region.

Because Z_{eu}-IOP was calculated using the same approach as a_{ph}490, we could also expect an improvement of Z_{eu}-IOP over Z_{eu}-Chla; particularly for MODIS that showed a larger difference in the validation between the two Z_{eu} approaches and lower uncertainties of a_{ph}490 than Chla. However, this was not observed here and it is likely related to our validation datasets of Z_{eu}, a_{ph} and Chla which greatly differ in number of samples and location. Moreover, our a_{ph} validation dataset is small, especially for SeaWiFS. From 271 *in situ* a_{ph} collected between 2007 and 2010, 12 matched with SeaWiFS observations. Persistent cloudiness and high solar zenith angles limit the satellite retrievals in the SO.

3.4.4   Primary Production

Finally, the impact of the Z_{eu} products on the NPP was as expected; deeper Z_{eu} led to an increase in NPP as more light was available (Figure 3.6). Note that the classification of empirical and semi-analytical used for Z_{eu} is not valid for NPP since both NPP-Z_{eu}-Chla and NPP-Z_{eu}-IOP

used a_{ph} derived from QAA. The spatial differences observed between Z_{eu}-Chla and Z_{eu}-IOP strongly influenced the NPP estimation. In both NPP calculations we used the same set of input data (PAR, D_{irr}, $\bar{a}_{ph}$), except for Z_{eu}, thus the observed differences can be directly attributed to Z_{eu}. In particular, NPP-Z_{eu}-Chla estimates were much higher than NPP-Z_{eu}-IOP in the western part of the South Pacific subtropical gyre and south of 60°S. The latter region is of great importance in the global carbon cycle, as pointed out by Arrigo et al. (2008) and Takahashi et al. (2009). According to these authors, once the sea ice retreats in springtime, more light and nutrients become available enhancing the development of phytoplankton blooms and leading to a strong sink of atmospheric CO_2. Accurate estimates of NPP are essential for a better understanding of the role of the SO in the global carbon cycle.

From the results presented here it becomes clear that the uncertainties of Z_{eu} should be considered to improve the estimates of NPP. Saba et al. (2011) investigated how satellite derived sea surface temperature, mixed layer depth, Chla and PAR affected the NPP estimates of 21 ocean colour models. They found that when uncertainties of the Chla are accounted for in NPP models, the root mean square difference is reduced by 44% in the Antarctic Polar Front Zone. They also observed that biases in the ocean colour NPP estimates are related to the water column depth, possibly due to uncertainties in the Z_{eu}.

3.5 Conclusions

Here we provided a quality assessment of the Z_{eu} derived from MODIS and SeaWiFS using a large dataset of *in situ* measurements in the SO. In summary, satellite Z_{eu} derived using the Chla and IOP approaches are reliable in the region. Although uncertainties depend on the sensor and approach used, the best results were obtained by the IOP approach using SeaWiFS data. Within the MODIS data, Z_{eu} estimation with the Chla approach generally yielded better results than the IOP approach. When assessing the differences in the spatial distribution between Z_{eu}-Chla and Z_{eu}-IOP, large discrepancies were observed over specific regions with significant impact on the NPP retrievals. Those differences were not observed in the validation. Therefore, we emphasize the importance of spatial studies together with the validation using *in situ* measurements for comparing ocean colour satellite products retrieved from different sensors and approaches. Further, we validated a_{ph} and found that MODIS data lead to lower uncertainties of $\bar{a}_{ph}$ and $a_{ph}443$ than SeaWiFS data.

To which extend these results are influenced by the lack of *in situ* measurements in our dataset used for validation and/or by regional differences in the SO is still unclear. To look more deeply in this issue and to address these differences found in the spatial distribution of Z_{eu} and NPP, a more representative dataset of simultaneous bio-optical and NPP data is necessary. The results presented here can support future campaigns by prioritizing areas of disagreement between approaches and poorly sampled regions to reduce uncertainty of NPP in regional and global scales. In addition, special designed satellite missions using at least two quasi-polar orbits and same optical sensor could be considered. In this case, earlier (later) equator crossing time in descending (ascending) mode would increase signal to noise for the SO, thus reducing uncertainties of NPP estimates.

Chapter 4

Global retrieval of diatoms abundance based on phytoplankton pigments and satellite data

4 Study 2: Global retrieval of diatoms abundance based on phytoplankton pigments and satellite data

4.1 The role of diatoms in the Southern Ocean

Diatoms are the most diverse phytoplankton group of the global oceans (Armbrust 2009) and the highest number of endemic diatoms species is found in the SO (Smetacek et al. 2004). These organisms occur in a wide range of environments due to several abilities. Under nutrient or light stress, diatoms can: migrate in the water column by controlling their buoyancy, store nutrients in the central vacuoles for later use, reduce iron requirements and maintain symbiosis with nitrogen fixing cyanobacteria (Armbrust 2009; Kooistra et al. 2007). In addition, diatoms produce thick cell walls, spines and toxins to avoid grazers (Kooistra et al. 2007; Smetacek 1999) and the rapid mass sinking events are considered a seeding strategy to overcome periods adverse to growth conditions (Kooistra et al. 2007; Smetacek 1985).

In iron-limited regions of the SO, the community of diatoms is dominated by large species with thick silica shells and high silica to nitrogen ratio (>2, Smetacek et al. 2004) for grazer protection (Assmy et al. 2013). Key species in iron-limited regions include the endemic *Fragilariopsis kerguelensis* and *Thalassiothrix antarctica* (Smetacek et al. 2004). While the biomass is recycled in the surface by grazing, the sinking out of the thick shells sequesters silica, resulting in loss of Si (silica sinkers) but retention of N and P at surface. Part of the frustules will dissolve while sinking and accumulate as silicic acid in the Circumpolar Deep Water and part will be buried into the sediments forming the major global biogenic silica accumulation (Smetacek 1999; 2004).

In iron-replete regions on the other hand, large-medium sized and weakly silicified diatoms prevail. These diatoms have high growth rates and form high biomass blooms that drive the carbon pump (Smetacek et al. 2004). Common diatoms include *Thalassioria antarctica* and the genus *Chaetoceros*. As a result, diatoms shape the biogeochemistry of the oceans as carbon and silica sinkers (Assmy et al. 2013; Smetacek et al. 2004), in addition to their role in the marine food web leading to intensive fisheries in coastal waters (Armbrust 2009).

4.2 Motivation

This second study examines the satellite retrievals of diatoms abundance derived by the ABA of Hirata et al. (2011). Compared to optically based approaches, a great advantage of the ABA is the smaller computational effort; even if the satellite data volume becomes larger with higher temporal and spatial resolutions, the data processing load is not heavy and re-processing can also be done relatively easily. The ABA can be applied to global level-2 or level-3 products of TChla, which are freely available to the scientific community, as opposed to, for example, PhytoDOAS method that uses the top of atmosphere radiance data (*i.e.* level-1 product) which is not freely available. On the other hand, because ABA is an empirical model, it is recommended to re-

evaluate the approach in the light of additional *in situ* phytoplankton pigment data and/or satellite data.

This study is based on two premises: (i) diatoms are the major primary producers and key players in the carbon and silicon pump in the SO and (ii) 90% of the diffusely reflected irradiance measured by ocean color sensors originates from the first optical depth, also referred to as the penetration depth (Z_{pd}) (Gordon and Mccluney 1975). These premises are also general limitations of the existing ABA. Although Hirata et al. (2011) used a large global dataset of phytoplankton pigments, new measurements, particularly in the SO (defined here as the region south of 50°S), have become available since then. Main objectives of this study are:

(1). Compilation of a new and large global dataset of *in situ* phytoplankton pigment profiles, including more measurements in the SO (Figure 4.1) which was not well covered previously, and to investigate the relationship between fractional contribution of diatoms and TChla using the new dataset in comparison to previous findings.

(2). Refinement of the ABA to account for the pigment information in the Z_{pd} (ABA$_{Zpd}$). In ABA (Hirata et al. 2011), the fractional contribution of diatoms to TChla was estimated based on the previous work of Uitz et al. (2006), who used the phytoplankton pigment concentration integrated over the euphotic depth (Z_{eu}). However, the pigment concentration estimated by the satellite sensor is an optically-weighted concentration in the Z_{pd}, which is approximately 4.6 times shallower than the Z_{eu} (Hyde et al. 2007).

(3). Evaluation of the performance of the ABA (*i.e.* ABA$_{Zpd}$) for global oceans and for the SO region.
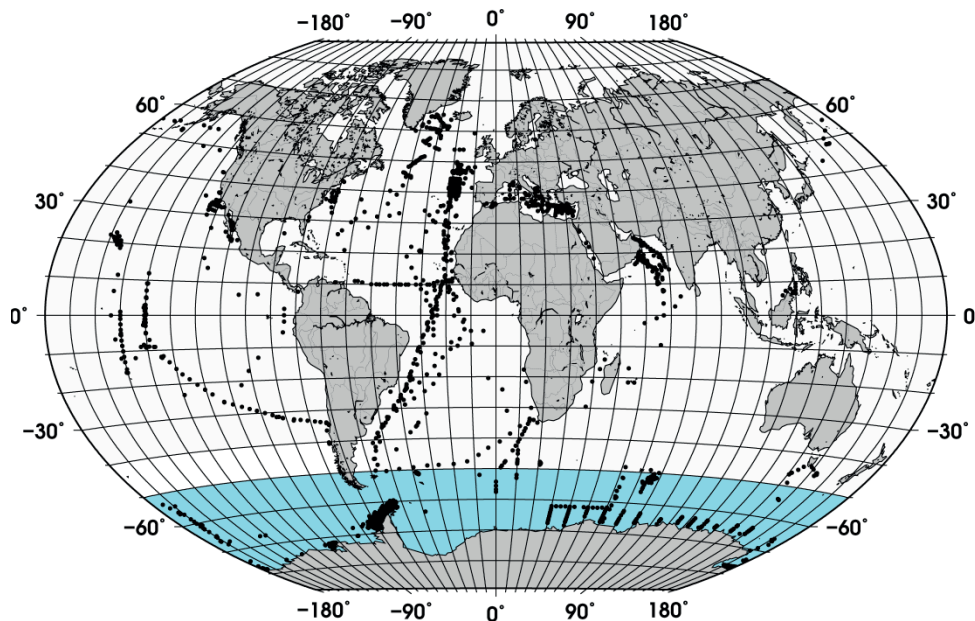
Figure 4.1. Distribution of the quality controlled in situ measurements. The SO, region south of 50°S, is the portion of the global ocean presented in blue.

4.3 Data and Methods

4.3.1 In Situ Measurements of Phytoplankton Pigments

A dataset of phytoplankton pigment profiles measured with the HPLC technique was supplemented with data obtained from the SeaWiFS Bio-optical Archive and Storage System – Sea-BASS (Werdell et al. 2003), Marine Ecosystem Data – MAREDAT (Peloquin et al. 2013), and from the individual cruises KEOPS (Uitz et al. 2009b), Bonus Good Hope, ANT-XVIII/2 - EisenEx, ANTXXI/3 – EIFEX (Smetacek et al. 2012), ANT XXVI/3, ANT XXVIII/3, Sonne SO218 (Cheah et al. 2013), Merian 18-3, Meteor 55 and Meteor 60. The pigments from the cruises Meteor 55, Meteor 60, ANT XXVI/3 and ANT-XVIII/2 were measured in accordance with the method described in Hoffmann et al. (2006) and for the cruises Merian 18-3 and ANT XXVIII/3 in accordance with Taylor et al. (2011).

The data were quality controlled in a way similar to the one used by Uitz et al. (2006) and Peloquin et al. (2013): (i) Samples with accessory pigment concentrations below 0.001 mg m^{-3} were set to zero, (ii) samples with TChla below 0.001 mg m^{-3} and fewer than 4 accessory pigments were excluded. To ensure that the profiles had a minimum vertical resolution, we restricted the dataset to profiles with at least (i) one sample at the surface (0 to 12 m), (ii) one sample below the surface, (iii) samples collected at four or more different depths, and (iv) with one sample within the Z_{pd}. The last quality control measure was based on the $\log_{10}$-linear relationship between TChla$_{Zpd}$ and the sum of all accessory pigments in the Z_{pd} (TACC$_{Zpd}$). Data that fell outside the 95% confidence interval were removed. The quality controlled dataset was corrected for Fuco to account for its co-existence in other PFTs, in accordance with Hirata et al. (2011).

In addition, samples located in coastal waters (< 200 m) were excluded using the ETOPO1 bathymetry (Amante and Eakins 2009). The final dataset contained 3988 samples, which were randomly split into work (70% of the data) and validation (30% of the data) subsets. While the whole dataset was used to calculate the partial coefficients used for estimating f-Diatom$_{Zpd}$, the work and validation subsets were used for model development and validation of the ABA$_{Zpd}$, respectively.

4.3.2 Satellite Data

Eleven years (2003–2013) of MODIS Aqua Level 3 4km binned TChla data (R2012.0) were used. MODIS is a multispectral sensor on board of the Aqua satellite and with global coverage. The data were obtained from http://oceancolor.gsfc.nasa.gov/ at daily temporal resolution. Monthly averages of diatoms abundance were calculated onto a 10 minute grid and used to derive climatological maps of diatoms abundance. To avoid coastal waters, where the retrieval of the ABA was not intended, we removed grid cells located in waters shallower than 200 m using the ETOPO1 bathymetry (Amante and Eakins 2009).

4.3.3 An Improved Abundance Based Approach

In previous approach (Hirata et al. 2011), the *f*-Diatom was calculated using the coefficients of Uitz et al. (2006), which take account of the phytoplankton pigment integrated over the Z_{eu}. Here, we extended the ABA to take account of the information in the Z_{pd}. For this purpose, we recalculated the coefficients a_i (Eq. 2.30) using the updated global dataset of HPLC phytoplankton pigment profiles. The weighted pigment concentration in the Z_{pd} (DP_{Zpd}) was calculated as described in Gordon and Clark (1980) for TChla:

$$C_{pd} = \frac{\int_0^{Z_{pd}} C(z)g(z)dz}{\int_0^{Z_{pd}} g(z)dz} \tag{4.1}$$

where C is the TChla at a depth z and g is:

$$g(z) = \exp\left[-2\int_0^z Kd(z')dz'\right] \tag{4.2}$$

The same approach was applied to the other pigments. The light attenuation coefficient (Kd_{490}, m^{-1}) was estimated from profiles of chlorophyll-a concentration (Morel and Maritorena 2001):

$$Kd_{490}(z) = Kd_w + 0.07242 * TChla(z)^{0.68955} \tag{4.3}$$

where Kd_w (m^{-1}) is the attenuation coefficient for pure water (0.01660 at 490 nm). The Z_{pd} was computed as $Z_{pd} = Z_{eu}/4.6$ and Z_{eu} was derived from the surface TChla as $Z_{eu} = 34TChla^{-0.39}$ (Morel, in Lee et al. 2007). Profiles were interpolated with 1-m increments from the deepest sample to the sample closest to the surface before the calculation of DP_{Zpd}.

Nonlinear minimization was used to retrieve the partial coefficients, which represent the estimates of the TChla to the DP ratios (Uitz et al. 2006). The function to be minimized is expressed as:

$$\|exp(c)M_{Zpd}\| \rightarrow min \tag{4.4}$$

where c is a vector containing the seven coefficients which each correspond to each DP_{Zpd} on the log scale, and M_{Zpd} a matrix containing the seven DP_{Zpd}. The nonlinear minimization method requires an initial guess of c, which was obtained from the multiple linear regression analysis. The standard deviation of the coefficients is given by the square root of the diagonal elements of the inverse of the Hessian matrix.

Using the new coefficients, the *f*-Diatom$_{Zpd}$ was calculated for each sample of the work and validation subsets. The work subset was then sorted according to the TChla$_{Zpd}$ and smoothed with a 5-point running mean filter to improve the signal-to-noise ratio (Hirata et al. 2008; Hirata et al. 2011). Next, the relationship between *f*-Diatom$_{Zpd}$ and TChla$_{Zpd}$ was quantified using a nonlinear least-square fit applied to the work subset and represented by a model and its fitting parameters. Once the model has been defined, satellite-derived TChla data was applied to the model to obtain

the global distribution of f-Diatom$_{Zpd}$. Diatom abundance (Diatom$_{Zpd}$, mg m^{-3}) is then obtained by multiplying f-Diatom$_{Zpd}$ by TChla$_{Zpd}$.

The accuracy of the new model was tested using the validation subset. The uncertainties were estimated by the mean absolute error (MAE, Willmott and Matsura 2005) between the modeled and the measured (*in situ*) Diatom$_{Zpd}$. The models were compared by the difference between the MAE of the original model and the new model, relative to the original model, and expressed in percent (%). The data were log transformed prior to the calculation of the validation statistics. We used log$_{10}$(data + λ) where λ=0.00003, approximately one half of the smallest non-zero value of the *in situ* Diatom$_{Zpd}$ validation data, since the dataset contained zeroes. In addition, to investigate whether using different partial coefficients results in significant changes in f-Diatom, we estimated f-Diatom using the coefficients of Uitz et al. (2006) and Brewin et al. ((2014)) and compared the results based on the coefficient of determination. The processing steps of ABA$_{Zpd}$ are summarized in Figure 4.2.
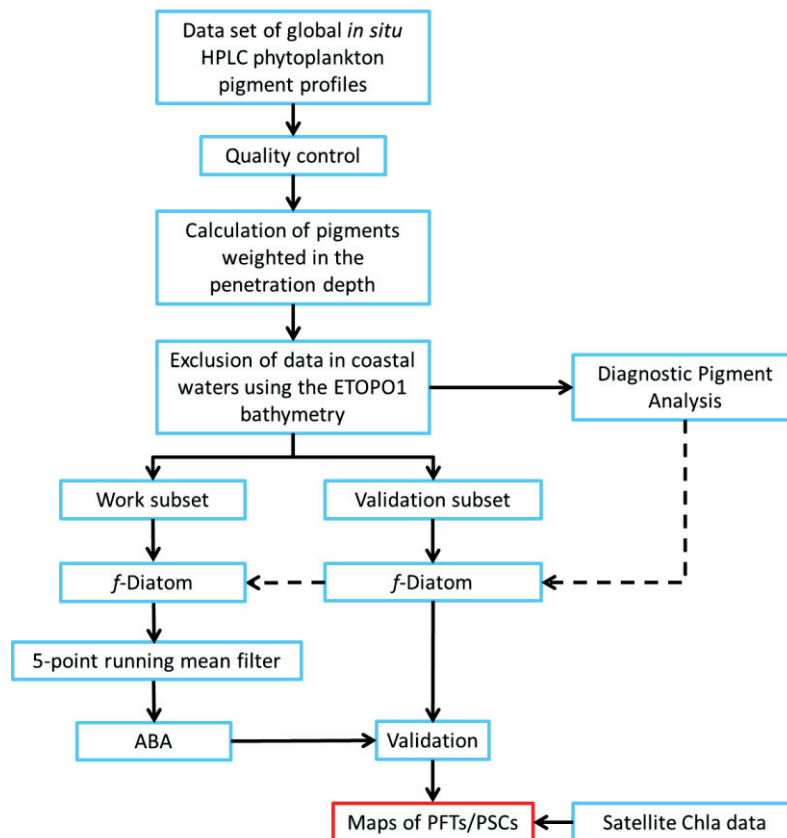
Figure 4.2. A flow chart of the processing steps conducted to retrieve diatom abundance using ABA$_{Zpd.}$

4.3.3.1 A Regional Model for the SO

The main difference between the SO model and the global model is that the relationship between Diatom$_{Zpd}$ and TChla$_{Zpd}$ is investigated not in terms of f-Diatom$_{Zpd}$, but instead in terms of the concentration of TChla$_{Zpd}$ that is attributed to diatoms, similar to the approach adopted by Brewin et al. (2010) to retrieve phytoplankton size classes. As in Brewin et al. (2010), the fit func-

tion was applied to $\log_{10}$-transformed data. To develop the regional model for the SO, we selected the samples of the global work and validation datasets that were located in the SO, creating a SO work and a validation dataset with 1069 and 460 samples, respectively. The relationship between $Diatom_{Zpd}$ and $TChla_{Zpd}$ was investigated and validated. Note that for the work dataset we applied the running mean exclusively to the SO data.

4.3.4   Statistical Analysis of Trends

Linear trends were computed for February from monthly standardized anomalies over the 2003-2013 period in the SO using the regional model. To remove the seasonal cycle we calculated the monthly anomalies in diatoms abundance for each grid cell by subtracting the climatological mean from the corresponding monthly mean (e.g., February 2003 - climatology of February). The monthly anomalies were divided by the corresponding climatological standard deviation (e.g., standard deviation of February) to enable the direct comparison of trends between different regions (grid cells). The trends were computed using the non-parametric Kendall's tau test with Sen's method at the 95% confidence level and in grid cells with 100% temporal coverage.

4.4   Results and Discussion

4.4.1   The ABA_{Zpd}

Table 4.1 shows the partial regression coefficients, and their respective standard deviation, calculated with Eq. 4.4. For comparison, we also present the partial coefficients estimated by Uitz et al. (2006), Brewin et al. (2014) and Fujiwara et al. (2014). Comparing our coefficients with those from Uitz et al. (2006), there is a notable difference, except for the coefficients of Fuco and TChlb. These differences result from the inclusion of more profiles, their geographical distribution, the adjustment of Fuco prior to the DPA analysis, and because we used the pigment concentration weighted in the Z_{pd}, while Uitz et al. (2006) integrated the pigments over Z_{eu}. When compared to the two other studies, where the partial coefficients were derived from surface measurements, our coefficients are more similar to those described in Brewin et al. (2014). Brewin et al. (2014) included measurements of five Atlantic Meridional Transect (AMT) cruises in the Atlantic Ocean, while Fujiwara et al. (2014) used measurements from three cruises in the Western Arctic Ocean. Although our dataset includes measurements from these regions, the number of samples in the Arctic region is fewer than that from the Atlantic (Figure 4.1).

Table 4.1. The partial regression coefficients and standard deviation (in brackets) where available. The number of samples is indicated by N. The empty fields indicate that the coefficient is not statistically significant.

Coefficients	Ocean	N	Fuco	Perid	Hexfuco	Butfuco	Allo	TChlb	Zea
Present study	Global	3988	1.554 (0.010)	0.413 (0.568)	0.855 (0.068)	1.174 (0.145)	2.387 (0.099)	1.062 (0.070)	2.037 (0.040)
Uitz et al. (2006)	Global	2419	1.41 (0.02)	1.41 (0.10)	1.27 (0.02)	0.35 (0.15)	0.60 (0.16)	1.01 (0.10)	0.86 (0.09)
Brewin et al. (2014)	Atlantic	466	1.72	1.27	0.68	1.42	4.96	0.81	1.28
Fujiwara et al. (2014)*	Arctic	76	1.85	1.49	1.74		5.88	1.31	3.54

* standard errors are less than 1.

Moreover, we have re-run the analysis taking into consideration the surface samples (< 12 m) from our profiles and observed only a slight difference in the coefficient of Fuco (1.531) as compared to the weighted Z_{pd} concentrations. Except for Perid and Hexfuco, the standard deviation of our coefficients are lower than, or similar to, the ones obtained by Uitz et al. (2006).

Nonetheless, we observed very similar f-Diatom values when using the partial coefficients of Uitz et al. (2006), Brewin et al. (2014) and ours. The coefficients of determination are higher than 0.98, suggesting the choice of partial coefficients has no influence on the retrievals of f-Diatom, which is consistent with Brewin et al. (2014). Brewin et al. (2014) compared size-fractionated chlorophyll (SFC) estimated from phytoplankton pigment data and calculated using Uitz et al. (2006) partial coefficients and their own, with size-fractionated filtration (SFF) measurements. They observed biases between SFC and SFF for nanoplankton and picoplankton size classes; however, the variations in the partial coefficients did not influence the results significantly. The high correlation between the $TChla_{Zpd}$ and DP_w, with DP_w calculated using Eq. 4.4 ($r^2 = 0.85$, $DP_w = 0.86 \ TChla_{Zpd} + 0.074$, N = 3988, p < 0.001), gives us confidence to use the partial coefficients to determine the f-Diatom.

Figure 4.3 shows the change in the f-Diatom$_{Zpd}$ with increasing $TChla_{Zpd}$. The green and blue lines represent the new model (ABA_{Zpd}) and the model of Hirata et al. (2011) (ABA*), respectively, parameterized with the DP_{Zpd} dataset. The red line represents the original model and fitting parameters of Hirata et al. (2011) (ABA**). It can be seen that diatoms are dominant at high $TChla_{Zpd}$ (Figures 4.3a and b), which is consistent with previous studies (Hirata et al. 2011) even if a significant number of new samples were added in our dataset. Moreover, we also observed unusually high f-Diatom$_{Zpd}$ in low $TChla_{Zpd}$ waters (< 0.1 mg m^{-3}, N = 670). Taking a closer look at the profiles, in which Fuco$_{Zpd}$ corresponded to at least 50% of the $TACC_{Zpd}$, we observed that most of the data (12 out of 16) are from samples taken in Antarctic, in the East Antarctic marginal ice zone (BROKE cruise, Wright and van den Enden 2000). On average, the ratio of Fuco$_{Zpd}$ to $TChla_{Zpd}$ is 0.165 for the entire DP_{Zpd} dataset, 0.071 excluding the SO data, but 0.317 for the SO data, indicating higher f-Diatom$_{Zpd}$ values in low $TChla_{Zpd}$ waters in the SO.
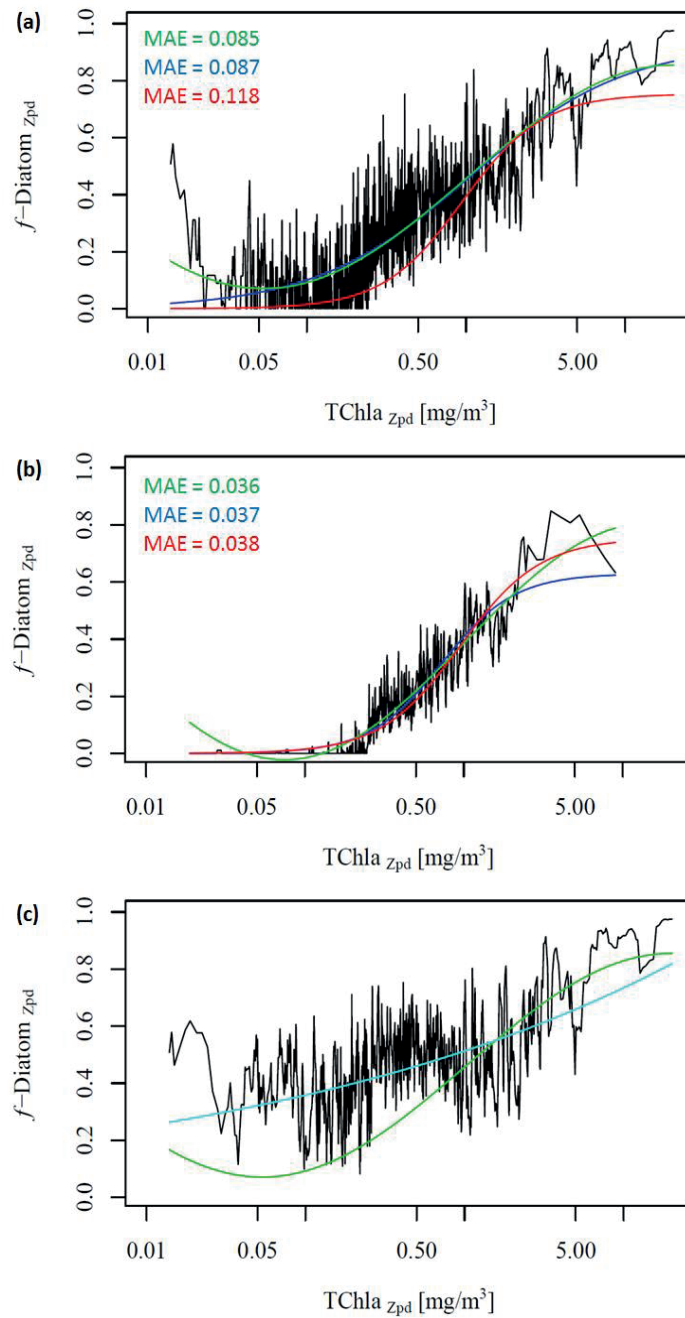
Figure 4.3. Relationship between $TChla_{Zpd}$ and $f\text{-Diatom}_{Zpd}$: **(a)** Global dataset (N = 2806), **(b)** global dataset excluding SO data (N = 1737) and **(c)** SO data (N = 1069). The datasets were smoothed with a 5 point running mean to improve the signal-to-noise ratio (Hirata et al. 2011) The green and blue lines represent the new model (ABA_{Zpd}) and the model of Hirata et al. (2011) (ABA*) parameterized with the DP_{Zpd} dataset. The red line represents the original model and fitting parameters of Hirata et al. (2011) (ABA**). The fitting parameters are presented in Table 4.2. The MAE values refer to the errors in terms of $f\text{-Diatom}_{Zpd}$. Note that we could not fit the global models to the SO dataset exclusively. The cyan and green lines in (c) represent the regional model for the SO and the ABA_{Zpd} plotted with the global fitting parameters as reference.

68

Table 4.2. Models of f-Diatom$_{Zpd}$ as a function of TChla$_{Zpd}$ and their respective fitting parameters used to plot the lines in Figure 4.3a and 4.3b. Note that we could not fit the global models to the SO data exclusively. The fitting parameters of the original ABA model of Hirata et al. (2011) (ABA**) do not change and therefore they are presented only once in the table.

	f-Diatom$_{Zpd}$	Model	a_0	a_1	a_2	a_3
	ABA$_{Zpd}$	$a_0 + a_1\sin(a_2(x + a_3))$	0.4629	0.3921	1.2214	-0.01412
Global dataset	ABA*	$[a_0 + \exp(a_1x + a_2)]^{-1}$	1.0733	-2.0484	0.1314	-
	ABA**	$[a_0 + \exp(a_1x + a_2)]^{-1}$	1.3272	-3.9828	0.1953	-
Global dataset	ABA$_{Zpd}$	$a_0 + a_1\sin(a_2(x + a_3))$	0.3909	0.4131	1.3763	-0.0114
excluding SO	ABA*	$[a_0 + \exp(a_1x + a_2)]^{-1}$	1.5890	-4.3778	-0.1521	-
data						

$x=\log_{10}$(TChla)

*model of Hirata et al. (2011) parameterized with the DP$_{Zpd}$ dataset.

**original model and fitting parameters of Hirata et al. (2011).

Considering our newer dataset, Hirata et al. (2011) considerably underestimates f-Diatom$_{Zpd}$ in almost the entire TChla$_{Zpd}$ range (Figure 4.3a - red line). This is partly due to the difference in the dataset used. When we fit their model to the new dataset, the model is found to fit well to the data, as indicated by the low errors (Table 4.3 and Figure 4.3a - blue line). However, it fails when predicting f-Diatom$_{Zpd}$ in very low TChla$_{Zpd}$ waters, mostly for the SO. Thus, we test a new model, a sinusoidal function to better fit this observed trend in the SO (Table 4.3, Figure 4.3a - green line). The ABA$_{Zpd}$ and ABA* produce almost identical curves for TChla$_{Zpd}$ above 0.065 mg m^{-3} and similar fitting and validation statistics. The ABA** model provides accurate retrieval of diatoms globally. However, it produces larger errors than the ABA$_{Zpd}$ and the ABA* do for the SO. The ABA$_{Zpd}$ improves the MAE by 27.96% for the SO (Table 4.4 and Figure A2 in the Appendix).

Table 4.3. Statistical results of the fits for the global dataset and global excluding SO data using the fitting parameters of Table 4.2. Note that we could not fit the global models to the SO data exclusively. The fitting statistics for the SO dataset refer to the regional SO model (Figure 4.5). The MAE is given in f-Diatom$_{Zpd}$ for the global models and for the regional model in mg m^{-3} ($\log_{10}$-transformed data).

Fit		N	r^2	$p - $value	MAE
	ABA$_{Zpd}$	2806	0.71	$= 0$	0.085
Global dataset	ABA*	2806	0.70	$= 0$	0.087
	ABA**	2806	0.66	$= 0$	0.118
Global dataset	ABA$_{Zpd}$	1737	0.89	< 0.001	0.036
excluding SO data	ABA*	1737	0.88	< 0.001	0.037
	ABA**	1737	0.88	< 0.001	0.038
SO dataset	Regional model	1069	0.95	< 0.001	0.104

*model of Hirata et al. (2011) parameterized with the DP$_{Zpd}$ dataset.

**original model and fitting parameters of Hirata et al. (2011).

Table 4.4. Statistical results of the validation in terms of diatoms abundance. Note that we could not fit the global models to the SO data exclusively. The results for the SO dataset correspond to the global models using the global fitting parameters and the regional model. The MAE is given in mg m^{-3}. The statistics were calculated with log$_{10}$-transformed data (e.g., log$_{10}$(y+0.00003)).

Validation		N	r^2	p - value	MAE
	ABA$_{Zpd}$	1182	0.57	< 0.001	1.219
Global dataset	ABA*	1182	0.55	< 0.001	1.217
	ABA**	1182	0.57	< 0.001	1.035
Global dataset	ABA$_{Zpd}$	722	0.59	< 0.001	0.883
excluding SO data	ABA*	722	0.68	< 0.001	1.195
	ABA**	722	0.69	< 0.001	1.200
	ABA$_{Zpd}$	460	0.40	< 0.001	0.559
SO dataset	ABA*	460	0.39	< 0.001	0.562
	ABA**	460	0.39	< 0.001	0.776
	Regional model	460	0.39	< 0.001	0.465

*model of Hirata et al. (2011) parameterized with the DP$_{Zpd}$ dataset.
**original model and fitting parameters of Hirata et al. (2011).

To further investigate the influence of the SO data, we removed these data from the work dataset (38% of the data), recalculated f-Diatom$_{Zpd}$, and fitted the models (Figure 4.3b and Table 4.2). The comparison of Figure 4.3a and Figure 4.3b shows clearly the influence of the SO data, which is responsible for most of the data spread in Figure 4.3a as well as for the high f-Diatom$_{Zpd}$ in low TChla$_{Zpd}$ waters. When we exclude the SO data from the analysis, the fits improve greatly the MAE decrease to values close to 0.04 (Table 4.3). In addition, it leads to a better representation of the diatom abundance in oligotrophic waters, as well as to an underestimation of the actual f-Diatom$_{Zpd}$ in the SO, as shown in Figure 4.4. The advantage of including the SO data is a more realistic retrieval of diatoms in the SO, but an overestimation in other regions of low TChla$_{Zpd}$. While the *in situ* data show that the f-Diatom$_{Zpd}$ might be very low (~ 0) at very low TChla$_{Zpd}$ (e.g. in oligotrophic gyres), the predicted f-Diatom$_{Zpd}$ presents values higher than zero, overestimating f-Diatom$_{Zpd}$ in the oligotrophic gyres.
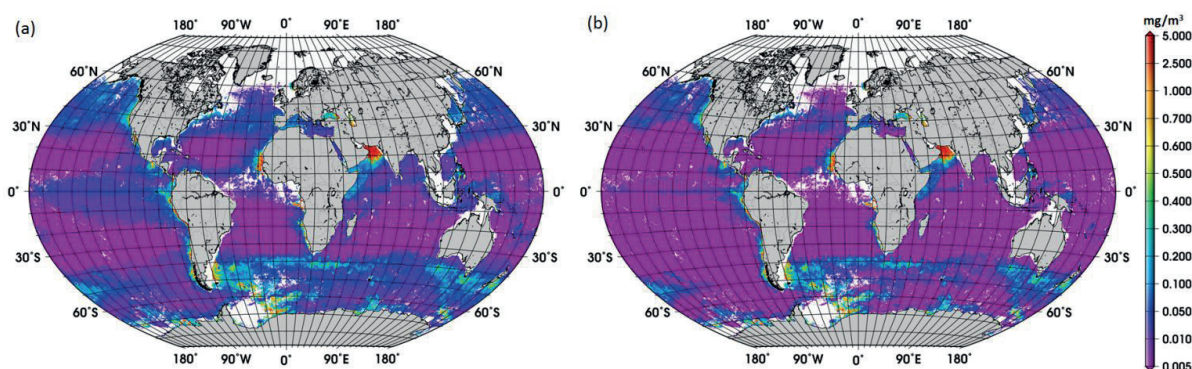
Figure 4.4. Monthly mean TChla$_{Zpd}$ (mg m^{-3}) of diatoms for February 2003 using the ABA$_{Zpd}$ model parameterized with: **(a)** Global dataset (average = 0.060 mg m^{-3}) and **(b)** global dataset excluding SO data (average = 0.041 mg m^{-3}). White areas correspond to waters with depths

shallower than 200 m or without satellite information.

It should be noted that the model used to retrieve f-Diatom$_{Zpd}$ as a function of TChla$_{Zpd}$ was empirically built upon *in situ* datasets, which showed that diatoms tend to be the dominant PFT at high TChla. However, this may not be the case of blooms of mixed PFTs, or dominated by a different PFT as pointed out by Brewin et al. 2010. For example, the coccolithophore *Emiliania huxleyi* typically occur in the North Atlantic and can form massive blooms in the Bering Sea (Iida et al. 2002). In the Ross Sea in the SO, blooms of the haptophyte *Phaeocystis antarctica* can exceed 15 mg m^{-3} and dominate the spring bloom, following by a later development of diatom blooms in the summer (Smith et al. 2012). In such cases, additional information on PFTs derived from methods that do not depend on this assumption (e.g. PhytoDOAS) may improve the knowledge on the diatom abundance and their distribution pattern.

Moreover, we did not obtain significant results in fitting the two global models to the SO data exclusively (Figure 4.3c, ABA$_{Zpd}$ plotted as reference). The diatoms in the SO exhibit a variability which is different from other oceanic regions (e.g., the North Pacific and the North Atlantic), and there is a need for a regional SO model. Thus, we developed a regional model for the SO, and the relationship between TChla$_{Zpd}$ and Diatom$_{Zpd}$ can be expressed as: $\log_{10}(y) = 1.1559\log_{10}(x) + (-0.2901)$ (Figure 4.5). The validation results of the SO model show that the regional model is consistent and more appropriate than the global ABA$_{Zpd}$ model for retrieving diatoms in the SO (Table 4.4 and Figure 4.5). The regional model improved by 17% the retrieval of diatoms abundance in the SO compared with the ABA$_{Zpd}$.
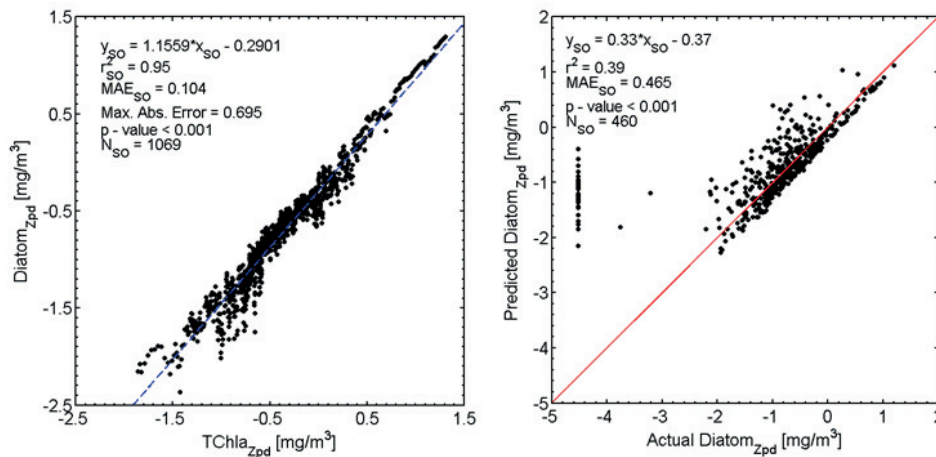
Figure 4.5. On the left: relationship between TChla$_{Zpd}$ and Diatom$_{Zpd}$ in the SO with the fit function plotted in blue ($\log_{10}$ transformed data). On the right: validation calculated with both $\log_{10}$ transformed data (e.g. $\log_{10}(y+0.00003)$). The red line represents the 1:1 line.

The ideal global retrieval of diatoms should apply the ABA$_{Zpd}$ model parameterized with the global dataset excluding SO data (Figure 4.3b green line) to the region north of 50°S, and the regional SO model for waters south of 50°S. These two models presented overall the lowest fitting and validation errors for the corresponding regions. This approach would not only provide more accurate retrievals of diatoms in the SO, but also overcome the overestimation of the global AB-

A_{Zpd} model in oligotrophic waters. However, applying two models generated a non-negligible off-set between the SO and adjacent oceans (result not shown).

4.4.2 *Satellite Retrieval of Diatoms using ABA$_{Zpd}$*

Acknowledging the uncertainties of the satellite Chla product, we first assessed the difference between the satellite retrievals of diatom abundance using the ABA$_{Zpd}$ and the original ABA, for the SO and global oceans. As expected from the previous findings (Figure 4.3a), we observed that, on average, higher abundances of diatoms were retrieved with the ABA$_{Zpd}$ than with the original ABA for the entire 2003-2013 period. For the SO, the concentration of diatoms calculated using the global ABA$_{Zpd}$ is 0.074 mg m^{-3} and for the global oceans 0.070 mg m^{-3}. In contrast, estimates of diatoms with the original ABA are 0.049 and 0.050 mg m^{-3}, respectively. For comparison, the concentration of diatoms using the regional SO model is 0.117 mg m^{-3}. This evidence of the enhanced abundance of diatoms retrieved from the global ABA$_{Zpd}$ model and from the regional SO model suggests that the production and export of carbon to the deep ocean might be larger than previously expected in the SO.

The new global climatology of diatom abundance is presented in Figure 4.6. The climatology for the SO is presented in the Appendix (Figure A3). The general distribution of the global diatom abundance is in line with current knowledge on the distribution of diatoms, *i.e.* higher concentrations of diatoms in the upwelling and coastal regions. Low concentrations of diatoms are observed in oligotrophic waters of the subtropical gyres and in HNLC waters, such as regions in the SO where waters are rich in macronutrients but are lacking in iron. There is also a clear seasonal cycle in the polar regions, with diatoms reaching the highest concentrations during their respective summer months, which is also observed in the climatology for the SO. Among other important patterns is the increase in diatom concentration from January to March and again high concentrations in September in the Arabian Sea. These observed patterns are associated with the Northeast and Southwest monsoons, respectively. According to Garrison et al. (2000), the monsoon seasons are generally characterized by increased concentrations of diatoms, thus our result shows a consistency with the previous *in situ* study too.
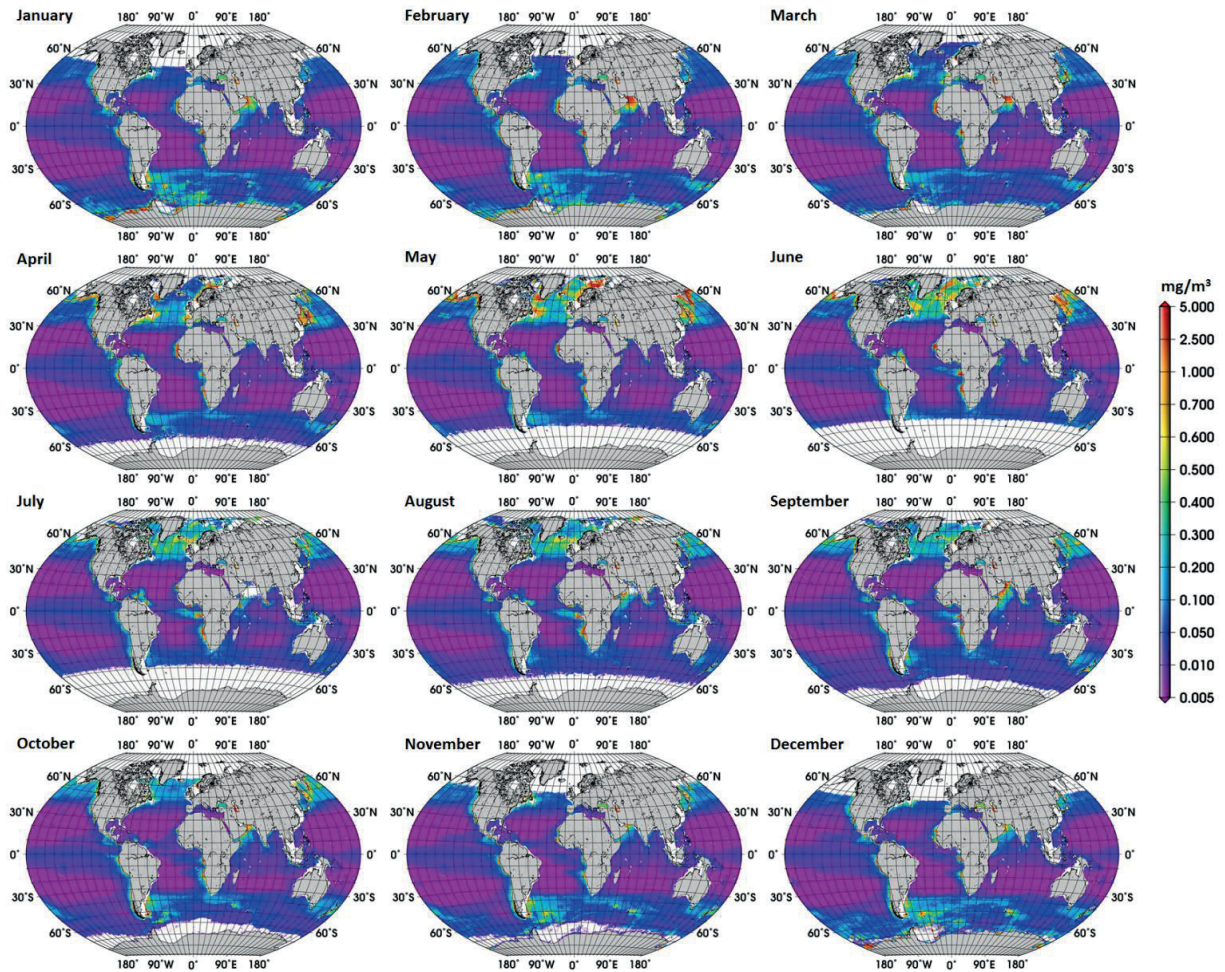
Figure 4.6. Climatology of TChla$_{Zpd}$ of diatoms (mg m^{-3}) for the months of January to December based on the period 2003-2013 retrieved using the ABA$_{Zpd}$ model. White areas correspond to waters with depths shallower than 200 m or without satellite information.

The climatology mostly covers the spatial variability, within a limited temporal range, whereas the trend gives information for a longer period, and both are important information for the understanding of ocean biogeochemistry. The spatial variability of the linear trends of diatom abundance in the SO is high, and no significant trend was observed for most of the sub regions of the SO (results not shown). Overall the trend for the SO was 0.036 (year^{-1}) (p-value = 0.019). Clearly, a more detailed analysis is needed to investigate the main driving forces behind these trends.

4.4 Conclusions

In conclusion, we have shown that the original ABA underestimates the diatom abundance in the SO. Our investigation revealed that diatoms in the SO might be more abundant than previous thought, possibly because (1) the lack of *in situ* phytoplankton pigment data, and that (2) the relationship between Chla and the *f*-Diatom in the SO is distinct from the global relationship.

We have developed a new global and a regional ABA$_{Zpd}$ that improves the uncertainties of the retrievals of diatoms in the SO. The mean absolute error (MAE) declined from 0.776 to 0.559 using the global ABA$_{Zpd}$, improving by 28% the estimation of diatoms in the SO. The regional mod-

el further improved the MAE by 17% (MAE = 0.465) compared with the global ABA_{Zpd} model. This was achieved by re-evaluating the ABA using a large dataset of global phytoplankton pigment profiles spanning 24 years (1988–2012). Additionally, the ABA was further improved by considering the information in the Z_{pd}.

We have shown that the ideal global retrieval of diatoms combines the ABA_{Zpd} model fitted to the dataset (excluding SO data, MAE = 0.883) with the regional SO model. However, applying two models generates an offset between the oceans, thus selective use of the global and the SO algorithms may be necessary depending on the objective of the application.

Satellite retrievals of PFTs are a useful tool for identifying and quantifying their presence in the oceans and in this study we have advanced our knowledge on the retrieval of diatoms from space by identifying limitations and developing improvements. Future studies should focus on optimizing the ABA method also for other PFTs.

Chapter 5

Mean patterns and interannual variability of diatom phenology in the Southern Ocean

5 Study 3: Mean patterns and interannual variability of diatom phenology in the Southern Ocean

5.1 Motivation

In the previous study we have advanced our knowledge on the retrieval of diatoms abundance from space by identifying limitations of the original method and developing a regional model for the SO. However, the mean patterns and interannual variability of the diatom bloom phenology in the SO remain unquantified. As the major primary producers in the region (Rousseaux and Gregg 2014), this study is focused on their specific phenology and variability. The aim of this chapter is improve previous studies on phytoplankton bloom phenology by: (i) focusing on the SO, (ii) using a new merged satellite Chla product with better spatial and temporal coverage than the datasets used in previous studies, (iii) examining a longer time series (1997-2012), (iv) looking at the concentration of Chla of diatoms using the regional algorithm of Soppa et al. (2014), (v) examining the different characteristics of the phenology, (vi) investigating trends, and for completeness, (vii) investigating if the interannual variability of the diatom phenology could be modulated by the large scale climate oscillations ENSO and SAM.

5.2 Data and Methods

5.2.1 Satellite data

We analysed 15 years (September 1997 – April 2012) of the level 3 Chla data (ESACCI-OC-L3S product, 4 km, version 1.0) from the Ocean Colour Climate Change Initiative (OC CCI). The OC CCI project is a European effort to produce high quality ocean colour products combining the MERIS, MODIS-Aqua and SeaWiFS sensors. Current data processing improves limitations of ocean colour remote sensing in polar regions due to low solar elevation and frequent cloud cover. Radiometric contaminations by sun glint, thin clouds or heavy aerosol plumes are removed from the MERIS with the Polymer algorithm (Steinmetz et al. 2011), while the SeaWiFS and MODIS data are processed for atmospheric correction with the algorithm of Gordon and Wang (1994). Subsequently, the SeaWiFS OC4v6 algorithm is applied on the merged remote sensing reflectance data to obtain the OC-CCI Chla product. The global validation of the Chla product with *in situ* HPLC Chla have shown that the relative errors are lower than 30% for most of the Chla range, except for concentrations lower than 0.1 mg m^{-3} (Krasemann et al. 2014). More details on the project and processing steps can be found in http://www.esa-oceancolour-cci.org/, where also the Chla data are available.

In our study, we calculated weekly averages of Chla from daily data onto a 15 minutes spatial grid for the area south of 50°S. To avoid coastal waters, we removed the three closest grid cells to the coastline. Diatom abundance was derived by applying the regional ABA$_{Zpd}$ SO model (Soppa et al. 2014) to the weekly Chla data, hereinafter referred to as Diatom-Chlorophyll-a (Dia-Chla).

5.2.2 Polar fronts position

We used the weekly position of the Polar Front (PF), available at http://ctoh.legos.obs-mip.fr/applications/mesoscale/southern-ocean-fronts, which is derived based on sea level anomalies observed in altimetry data and climatological mean sea level from historical data and ARGO profiles (Sallée et al. 2008). The mean and the standard deviation of the PF position were calculated from 1997 to 2012, for the months of September to April, the same period that was used to describe the phenology (see section 2.4). The standard deviation of the latitudinal position of the PF was used as a proxy of the interannual variability of the PF position. In addition, we included the mean position of the Southern Antarctic Circumpolar Current Front (SACCF) in our analysis. The SACCF position is derived from historical hydrographic data of the SO until 1990 (Orsi et al. 1995).

5.2.3   Maximum Sea Ice Extent

We used monthly sea ice extent data (Fetterer et al. 2002) for the SO to delineate the seasonal ice zone. The seasonal ice zone is the area delimited by the winter maximum of sea ice extent (NSDC 2015) which occurs in September. Sea ice extent data is available by the National Snow and   Ice   Data   Center   (NSIDC)   at ftp://sidads.colorado.edu/DATASETS/NOAA/G02135/shapefiles/. The maximum sea ice extent of September was binned into longitude bins of 1 degree. Coordinates were automatically extracted from the sea ice extent data and statistics (mean and standard deviation) of the latitude values were calculated for each longitude bin to examine the interannual variability in the entire period (1997 to 2012).

5.2.4   Climate indices

To investigate if the Dia-Chla phenology in the SO is influenced by ENSO and SAM, we used two indices: the Multivariate El Niño Southern Oscillation index (MEI) and the Antarctic Oscillation (AAO) index. The MEI, available at http://www.esrl.noaa.gov/psd/enso/mei/#loadings, is based on six variables (cloudiness, sea surface temperature, sea-level pressure, surface air temperature and the zonal and meridional components of the surface wind) over the tropical Pacific from 30°N to 30°S (Wolter and Timlin 1993). Positive MEI values characterize El Niño events while negative values indicate La Niña events. The Antarctic Oscillation (AAO) index, available at http://www.cpc.ncep.noaa.gov/products/precip/CWlink/daily_ao_index/aao/monthly.aao.index.b79.current.ascii.table, is based on the first principal component of monthly mean pressure anomalies at 700 mb for the region south of 20°S (Mo 2000). Positive/negative phases of the Southern Annular Mode (SAM) are associated with positive/negative values of AAO, respectively. Annual ENSO and SAM indices were calculated by averaging their respective indices from September of

the previous year to April of the following year, the same period used to estimate the phenological indices (Figure 5.1).
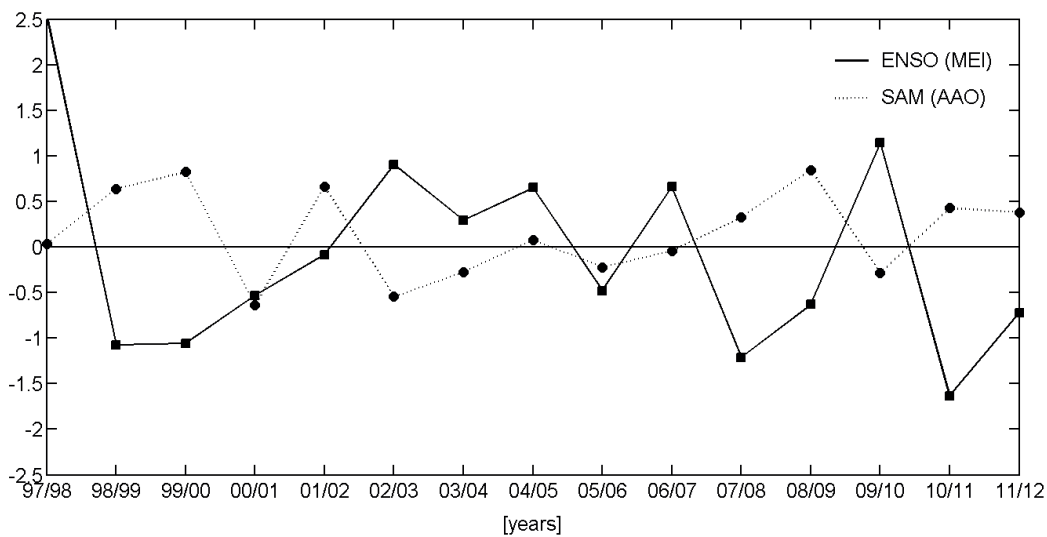
Figure 5.1. Time series (adimensional) of annual Multivariate ENSO Index (MEI, solid line) and Antarctic Oscillation index (SAM, dashed line).

5.2.5   *Phenological indices*

We assessed the diatom phenology using the threshold method of Siegel et al. (2002). Phytoplankton blooms start (defining the bloom start date - BSD) when the Chla value exceeds the value of 5% above the median (Siegel et al. 2002) and remains above this threshold for at least two consecutive weeks (Thomalla et al. 2011). To isolate primary blooms from secondary blooms, we first identified the maximum Chla of the time series and then looked backwards in time to find the bloom start date (Brody et al. 2013). The bloom end date (BED) was determined as the first week when Dia-Chla level fell below the threshold. The period between bloom start date and end date defines the total bloom duration (BD). Within this period the Dia-Chla reaches a maximum (CM) at the date of Dia-Chla maximum (CMD). The sub-periods before and after the maximum determine the bloom growth duration (BGD) and bloom decline duration (BDD), respectively. During the growth duration, the average (CAV) and integrated Dia-Chla values (CI) are calculated. In addition, the amplitude of the bloom (CA) is determined as the difference between maximum and threshold Dia-Chla value. The phenological indices are listed in Table 5.1 and illustrated in Figure 5.2. Using these indices, we analyzed the phenology in the entire time series (1997 to 2012), each year from September to April of the following year (e.g. September 2002 - April 2003).

Before computing the phenological indices, the time series were linearly interpolated in time to fill gaps less than 3 weeks in length (Henson and Thomas 2007). After the temporal interpolation, if there were remaining gaps of more than two weeks between the date of Dia-Chla maximum and the estimated bloom start or bloom end date, these phenological indices were not calculated to avoid erroneous detection of the bloom timing. This led to slightly different data coverage of the

phenological indices. The best data coverage is achieved for date of Dia-Chla maximum, Dia-Chla maximum and amplitude.

Table 5.1. Phenological indices.

Indices	Abbreviation	Units
Bloom Start Date	BSD	Week
Date of Dia-Chla Maximum	CMD	Week
Bloom End Date	BED	Week
Bloom Duration	BD	Week
Bloom Growth Duration	BGD	Week
Bloom Decline Duration	BDD	Week
Dia-Chla Amplitude	CA	mg m^{-3}
Dia-Chla Maximum	CM	mg m^{-3}
Dia-Chla averaged over BGD	CAV	mg m^{-3}
Dia-Chla integrated over BGD	CI	mg m^{-3}
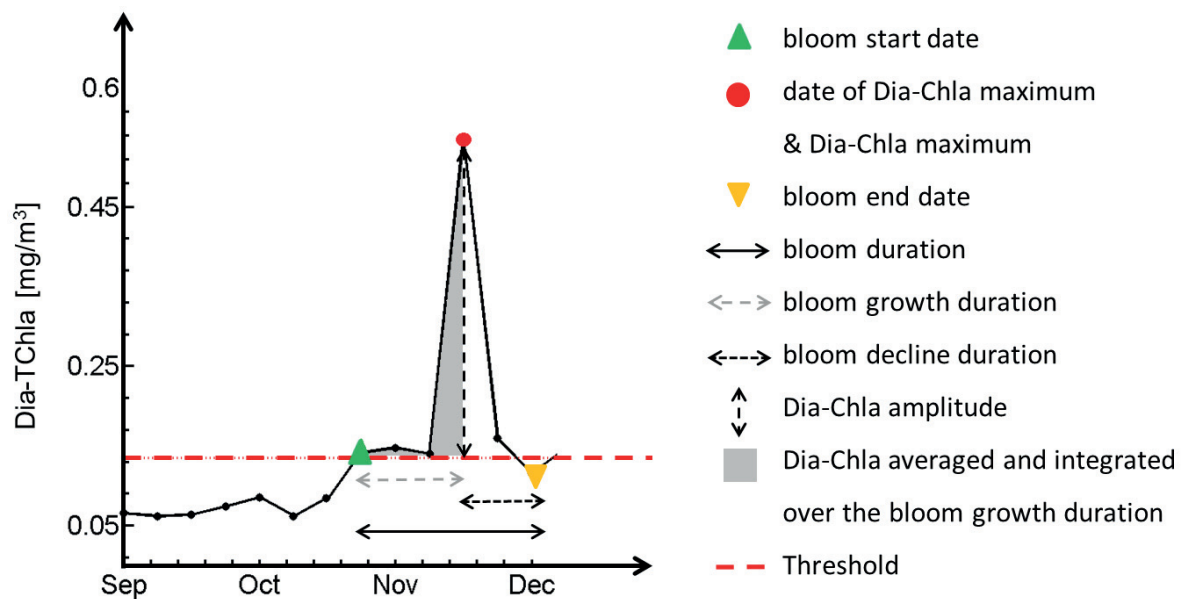
Figure 5.2. Schematic of the indices used to describe the diatom phenology.

5.2.6 *Statistical analysis*

The mean spatial patterns were obtained by averaging the 15 years of phenological indices. The interannual variability of the diatom phenology was examined by: (i) the relative standard deviation (RSD) of the indices, (ii) trends, (iii) correlations and partial correlations with ENSO and SAM and, (iv) composite maps of the anomaly of the indices. The relative standard deviation is the standard deviation of the indices divided by the average over the 15 years. Trends, correlations and composite maps were calculated using the standardized anomaly data. Standardized anomalies (adimensional and hereafter termed as anomalies) were produced by subtracting the average (15-yr) from the annual phenology data (e.g. 2002-2003) and dividing by the standard

deviation (15-yr), pixel by pixel. Trends were investigated with non-parametric Kendall's tau test with Sen's method at the 95% confidence level for each grid cell (only when 100% of data were available). The correlation between the climate indices and anomalies of the phenological indices was determined using Spearman correlation. Partial correlations were used to study the influence of both oscillations separately, for example, by considering the relationship between SAM and Dia-Chla maximum after removal of the variance of ENSO (Pohl et al. 2010). Composite maps of the anomalies of the phenological indices were computed by averaging the anomalies from the different phases (positive/negative) of the ENSO and SAM, as well as for amplified years (e.g. El Niño coincided with negative phase of SAM). Using composite maps we investigated the dominant patterns of the anomalies associated with the different phases and oscillations (Kwok and Comiso 2002).

5.3   Results and discussion

5.3.1   Mean spatial distribution of the phenological indices

The spatial patterns of the diatom phenological indices averaged over 15-yr of data are presented in Figures 5.3 to 5.5, together with the corresponding latitudinal variation in Figure 6. The spatial patterns of the indices are generally associated to the location of the asymmetric contour of the Southern Antarctic Circumpolar Current Front (SACCF) and of the maximum sea ice extent. This association is strong for the start date, date of maximum (peak), growth duration and total duration of the blooms. The connection between the indices and the fronts is clearer especially in the western part of the SO.

The general pattern of the bloom start date is consistent with Thomalla et al. (2011). The blooms start and the date of the maximum of Dia-Chla is reached earlier north of the SACCF - outside the seasonal ice zone (Figure 5.3). The authors linked the start of the blooms south of 40°S to the light availability (indicated by PAR). The development of the blooms in the SO following the increase in the seasonal PAR was also described by Racault et al. (2012). On the other hand, the end of the bloom of diatoms is more likely related to the exhaustion of nutrients (Smetacek 1999; Smetacek et al. 2004; Smetacek 1985). Borrione and Schlitzer (2013) suggested the exhaustion of silicate as limiting factor for the end of the spring bloom of diatoms in the South Georgia region. Grazing pressure is thought to control the diatom species composition and biomass, rather than the end of the diatom blooms (Smetacek et al. 2004).

In the seasonal ice zone the start of the bloom is driven by light as well as water column stability; as the sea ice retreats, the melting of ice increases the stratification of the water column which favors to maintain the phytoplankton in the euphotic zone. The end of the bloom occurs when the mixed layer deeps caused by wind forcing, which dilutes the phytoplankton in the water column (Taylor et al. 2013). Apart from melting of ice and wind forcing, changes in mixed layer depth in the SO are also caused by heating from the atmosphere (Sallee et al. 2010).

Particularly notable is the early start of the blooms in the waters surrounding Antarctica (light green), caused by the opening of areas free of ice around the continent. Arrigo et al. (2012)

showed that in the Amundsen polynya small areas free of ice occur throughout the year and that their size increases with three factors: advection of sea ice offshore, increase in temperature and melting of ice. These factors, combined with an increase in solar radiation and water column stability, as shown by Taylor et al. (2013), are linked to the earlier bloom start date in these waters surrounding Antarctica as compared to waters northwards of the seasonal ice zone.
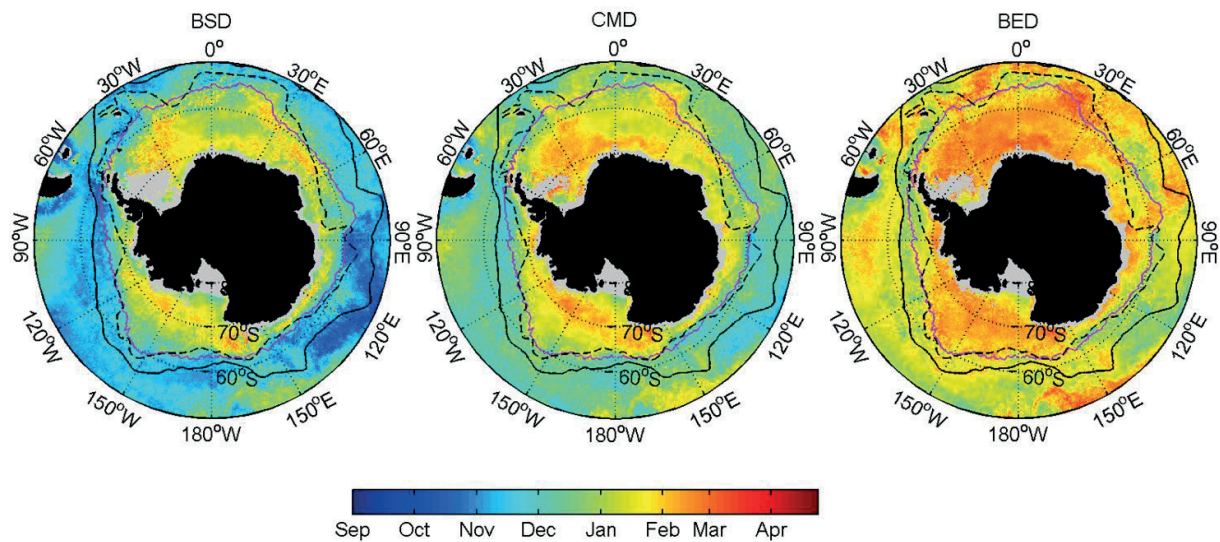
Figure 5.3. Spatial distribution of the mean diatom phenology in 1997 – 2012: (left) bloom start date – BSD, (center) date of Dia-Chla maximum – CMD, (right) bloom end date - BED. Grey areas represent missing data. Black solid lines show the mean position of the Polar Front (Sallee et al. 2008) over 1997-2012. Dashed lines show the Southern Antarctic Circumpolar Front (Orsi et al. 1995). Purple line displays the mean position of the maximum sea ice extent over 1997-2012 (Fetterer et al. 2002).

In general, the duration of the blooms is shorter south of the SACCF, in the seasonal ice zone, and vice versa. Outside this region it forms a belt of higher values (longer duration) around the Polar Front (PF), particularly between 30°W and 120°E (Figure 5.4). Compared to Racault et al. (2012), the overall duration of the blooms is shorter. The average duration of the blooms for the regions 50°S-60°S and 60°S-70°S was 8.3 and 6.5 weeks, while these authors reported 14 and 11 weeks, respectively. However, the authors used satellite Chla data to investigate the phytoplankton phenology, which includes all PFTs while in the present study we looked specifically at the diatom Chla concentration.

As shown by Taylor et al. (2013), the duration of the bloom in the seasonal ice zone results from a combination of factors influencing the growth and decline phases of the bloom, mainly light and stability of the water column, while nutrients are less important. The belt of "longer lasting" blooms outside the seasonal ice zone is likely linked to a complex inter-play of different forcings: longer light periods and deeper mixed layers (Sallee et al. 2010) that enhance the supply of nutrients at surface as well as reduce the grazing pressure by zooplankton (Behrenfeld et al. 2013). The mixed layer depth is deeper in the vicinity the fronts; around 100 m in the summer and up to 400 m in the winter (Sallee et al. 2010).

The deepening of the mixed layer in the winter together with diapycnal diffusion replenishes the surface with nutrients from subsurface waters, including iron (Tagliabue et al. 2014). It is known that iron is a limiting nutrient in the surface waters of the SO controlling phytoplankton growth, particularly in the open ocean. This micronutrient is rapidly depleted by spring blooms. In late spring and summer, phytoplankton relies on the pelagic recycling until the following deepening of the mixed layer in autumn (Tagliabue et al. 2014). Open ocean diatoms have the ability to reduce their requirement of iron (Armbrust 2009) which can help to sustain their blooms for longer periods.

In regions where the Antarctic Circumpolar Front (ACC) interacts with the topography, the nutrient supply is enhanced (Sokolov and Rintoul 2007) leading to higher Chla and consequently, higher amplitude of the blooms (Figure 5.5). This occurs for example in the Pacific Antarctic Ridge (see Figure 7 in Sokolov and Rintoul 2007). The enrichment from the coastal and shelf sediments close to islands (e.g. Kerguelen, Crozet and South Georgia Islands) are also important sources of nutrients, especially iron (Blain et al. 2007; Borrione et al. 2014; Planquette et al. 2007). Other important factors controlling the duration of the bloom are the increasing in grazing pressure and algal viruses (Behrenfeld et al. 2013; Smetacek et al. 2004).
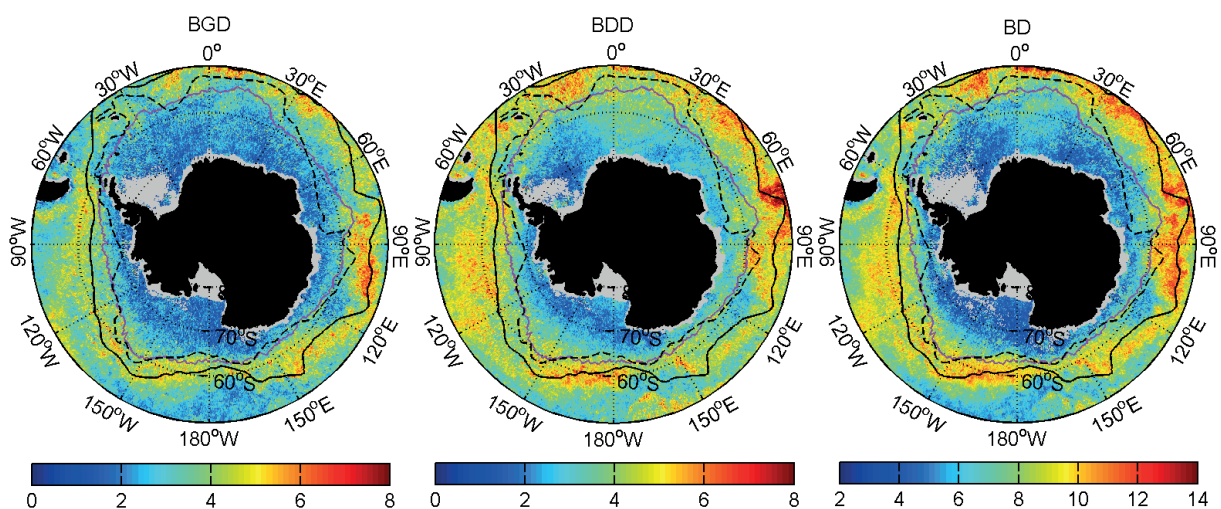
Figure 5.4. Same as Figure 5.3, but for bloom growth duration (BGD), bloom decline duration (BDD) and total duration (BD) of the blooms. Units are in week.

The relationship of the biomass indices with the fronts is not as evident as for the other indices (Figure 5.5). The spatial distribution shows that more intense blooms (higher biomass) occur in coastal regions, in the seasonal ice zone and in the Atlantic sector of the SO. Sokolov and Rintoul (2007) have showed that at a broader scale the distribution of Chla is mainly controlled by the upwelling of nutrients via Ekman transport while the upwelling associated with bathymetric features is responsible for the magnitude and duration of the blooms. Blooms around Antarctica can be considered as more efficient blooms, with short duration and high biomass.
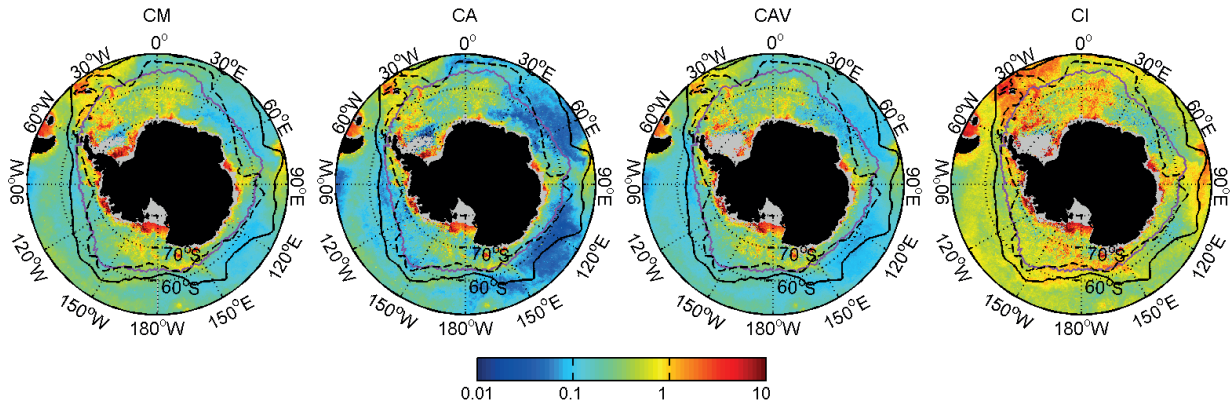
Figure 5.5. Same as Figure 5.4, but for Dia-Chla maximum (CM), Dia-Chla amplitude (CA), Dia-Chla average (CAV) and Dia-Chla integrated over the growth duration (CI). Units are in mg m^{-3}.

The latitudinal variability displays, from north to south, a progressive delay in the start, maximum and end date of blooms until about 73°S (Figure 5.6). The opposite is observed for the duration; there is a decrease in the growth, decline and total duration of the bloom from north to south. South of 73°S the trend is reversed except by the growth duration which holds at about the same duration. The biomass indices present similar latitudinal variations, but are rather small until the first peak at ~ 67°S, followed by two steep peaks at ~ 72°S and at ~ 76°S, and then decreasing towards the south.
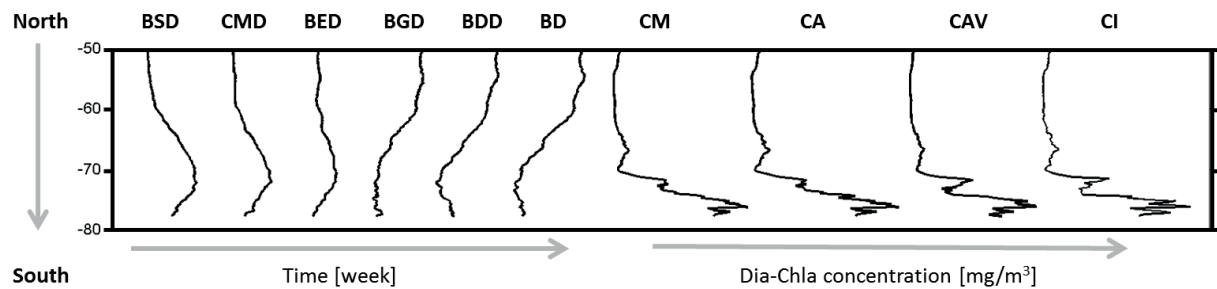
Figure 5.6. Schematic representation of the latitudinal variability (longitudinal average) of the phenological indices: bloom start date (BSD), date of Dia-Chla maximum (CMD), bloom end date (BED), bloom growth duration (BGD), bloom decline duration (BDD), bloom duration (BD), Dia-Chla maximum (CM), Dia-Chla amplitude (CA), Dia-Chla averaged BGD (CAV), Dia-Chla integrated over BGD (CI).

5.3.2   Interannual variability

The relative standard deviations of two of the phenological indices over the 15 years are displayed in Figure 5.7. To investigate whether the variability could be associated with a variation in the mean position of the Polar Front and in maximum sea ice extent, their relative standard deviations are also shown (dashed lines). The spatial patterns of the relative standard deviation of the bloom start date, date of Dia-Chla maximum and bloom end date are very similar to each other, as well as among the duration or biomass indices. This is corroborated by the correlation maps

83

among the date, duration and biomass indices presented in Figure A4. Figure 5.7 shows the maps with the highest variability of the relative standard deviation, namely bloom start date and Dia-Chla amplitude. The spatial variability of relative standard deviation of the duration indices does not show a clear pattern and therefore is not presented.

Comparing the relative standard deviation maps of bloom start date and Dia-Chla amplitude, the spatial distribution is different. The bloom start date presents higher variability in the vicinity of the fronts, while the amplitude shows higher variability in the seasonal ice zone. This suggests that the environmental forcings controlling the start date and the amplitude of the bloom are different. It is important to note that the variability of the indices is linked to the main position of the PF and the maximum sea ice extent, rather than with their variability which is low (dashed lines).

The variability of the amplitude of the bloom seems to be linked to the interannual variability in the sea ice concentration, which in turn controls the light availability and the stability of the water column. On the other hand, the variability in the bloom start date is probably related with the variability in the nutrient supply which is large where the seasonal amplitude of the mixed layer depth is strong and small in the ice-influenced region.
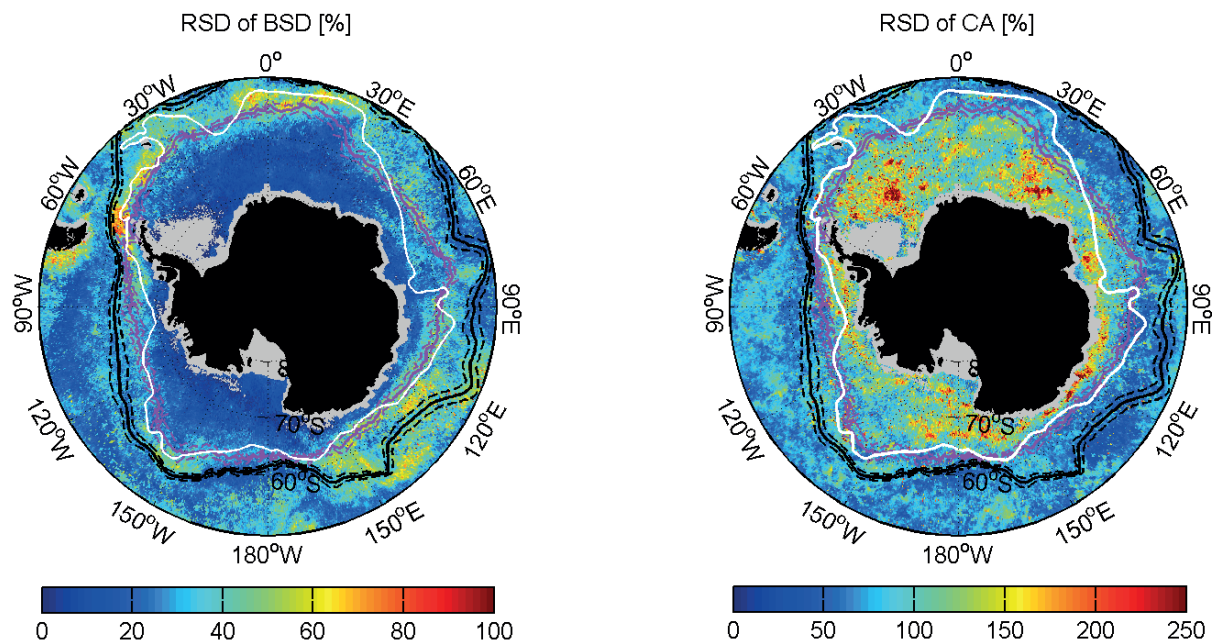
Figure 5.7. Spatial distribution of the relative standard deviation (RSD) of the bloom start date (BSD) and Dia-Chla amplitude (CA) for 15 years of data (1997-2012). Grey areas represent missing data. Black continuous lines represent the mean Polar Front position (Sallee et al. 2008) and dashed black lines the standard deviation of the position over 1997-2012. Purple continuous lines indicate mean of the maximum sea ice extent (Fetterer et al. 2002) and dashed purple lines the standard deviation of the position for the years of 1997 to 2012. White line indicates the mean position of the Southern Antarctic Circumpolar Front (Orsi et al. 1995).

5.3.2.1 Trends

Most of the indices are not gap free and for this reason trends could only be determined for the

date of Dia-Chla maximum, Dia-Chla maximum and amplitude. For the same reason the anomaly data were not detrended afterwards. Trends in the Dia-Chla amplitude are very similar to Dia-Chla maximum and not shown.

Coherent patches of significant positive and negative trends were detected for the date of Dia-Chla maximum and Dia-Chla maximum (Figure 5.8). For example, in the region between the Malvinas and South Georgia Islands (Figure 5.8, green star) there is a trend towards an earlier maximum of the bloom leading to higher biomass (Dia-Chla maximum). However, the relationship between the date of the maximum of the bloom and the biomass can be reverse as well, as in the region south of 60°S and between 120°E and 150°E (Figure 5.8, black star) where a later start of the bloom leads to an increase in biomass. Although we could not estimate trends in the bloom start date and bloom end date, we can expect a similar pattern to the ones detected for date of Dia-Chla maximum since these indices are highly correlated (Figure A4).

These observations combined with recent studies on the trends in sea surface temperature (Maheshwari et al. 2013) and sea ice cover (Maksym et al. 2012) over the last three decades, suggest a link between these two variables and the diatom phenology. For example, in the region south of 60°S and from 60°E to 120°E (Figure 5.8, grey star) the earlier date of Dia-Chla maximum and the increased Dia-Chla maximum coincide with the observed increase trend in SST and decrease in sea ice cover (earlier sea ice melt).

Compared to literature, the spatial distribution of trends in Dia-Chla maximum are similar to trends in total Chla from SeaWiFS reported by Henson et al. (2010) and Siegel et al. (2014) for the 1997-2007 and 1997-2010 periods, respectively. The last study on global total Chla trends (1998-2012), by Gregg and Rousseaux (2014), displays large areas in the SO with positive trends as we observed here, but also positive trends between the 60°E and 150°E north of 60°S whereas we observed negative trends. Different trends can be expected due to the different variables used (total Chla instead of Dia-Chla), as well as data treatment (bias correction, data assimilation) performed by the authors.
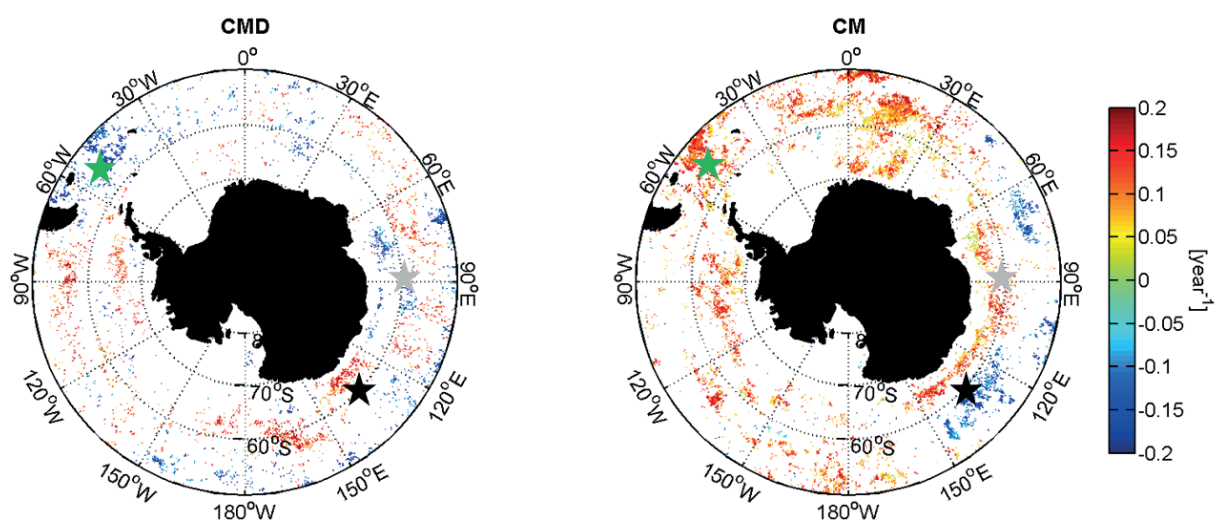
Figure 5.8. Trends of the standardized anomalies of date of Dia-Chla maximum (CMD) and Dia-Chla maximum (CM). Reddish colour indicates a positive trend and bluish indicates a negative trend. Only statistically significant trends ($p < 0.05$) are shown. The stars highlight the regions

between Malvinas and South Georgia Islands (green) and south of 60°S between 120°E to 150°E (black) and 60°E to 120°E (grey).

5.3.2.2 Relationships with ENSO and SAM

5.3.2.2.1 Correlation maps

To further explore the interannual variability of the diatom phenology, we examined the relationship of phenological indices with ENSO and SAM (methods described in section 5.2.5 and 5.2.6). During the 1997-2012 period there were six El Niño years (1997/1998, 2002/2003, 2003/2004, 2004/2005, 2006/2007, 2009/2010), eight La Niña years (1998/1999, 1999/2000, 2000/2001, 2005/2006, 2007/2008, 2008/2009, 2010/2011, 2011/2012), seven years of positive phase of SAM (1998/1999, 1999/2000, 2001/2002, 2007/2008, 2008/2009, 2010/2011, 2011/2012) and four of negative phase (2000/2001, 2002/2003, 2003/2004, 2009/2010). The correlation maps are presented in Figure 5.9 for date of Dia-Chla maximum and Dia-Chla maximum as representative of the date indices and biomass indices, respectively. Significant positive (negative) correlations indicate that the anomalies are in phase with ENSO and SAM. Coherent areas in the duration indices are less evident for the duration indices and not shown.

Several areas show significant correlation between ENSO/SAM and the diatom phenology. The correlation coefficients for ENSO are opposite to that of SAM. For example, the date of Dia-Chla maximum in the sector of the seasonal ice zone between 120°W-150°W is negatively correlated with ENSO (MEI index) and positively correlated with SAM (AAO index). Moreover, the patterns in El Niño (La Niña) years and negative (positive) SAM are similar. These results are in line with observations of the sea ice concentration, SST, Chla and wind speed and direction in the SO (Lovenduski 2007; Pohl et al. 2010). Smith et al. (2008) also observed that high biomass offshore the Western Antarctic Peninsula region was associated La Niña and/or positive SAM events. Hence, we can expect the spatial patterns of the anomalies of phenological indices during El Niño (La Niña) years and negative (positive) phase of SAM to resemble each other.

The most remarkable feature in the correlation maps of the date of Dia-Chla maximum can be seen in the Pacific Sector (90°W to 150°W), north of the PF and south of the maximum sea ice extent. This pattern is consistent with the results of Kwon and Comiso (2002) and Lefebvre et al. (2004) for earlier periods, 1982-1998 and 1980-1999 and using satellite and model data, respectively. For the same region, Kwon and Comiso (2002) observed an increase in SST and a decline in sea ice concentration associated with El Niño. Lefebvre et al. (2004) showed that the winter sea ice concentration decreases in negative SAM events. As a result, an earlier start, maximum and end of the bloom can be expected in El Niño or negative SAM events.

The Dia-Chla maximum displays less significant correlations, but the general pattern of Dia-Chla maximum is consistent with the results of Lovenduski and Gruber (2005) for the relationship between satellite Chla and SAM. In contrast, the general increase in diatom concentration between 50°S and 70°S during positive SAM event showed by Hauck et al. (2013) was not observed in our results. The authors used a coupled ecosystem – general circulation model and

lagged correlations (4 months) to investigate the relationship and these might be the cause for disagreement between the results, as well as the different periods analysed in their study (1948-2010) and in the present study (1997-2012). In addition, the observed lower Dia-Chla maximum at 60°E during El Niño (negative correlation) can be linked to lower SST in El Niño years, as shown by Kwon and Comiso (2002) (see Figure 6 in Kwon and Comiso, 2002).

Because SAM and ENSO are not linearly independent at interannual time scales during the austral summer season (L'Heureux and Thompson 2005; Pohl et al. 2010), we expected that some of the variability we observed related to SAM may be biased by ENSO, or *vice versa*. This was in part confirmed by the partial correlations (Figure A5), but the differences between the correlations and partial correlations are in general small. Higher differences were observed between the date of Dia-Chla maximum and MEI. The correlations with SAM and between the Dia-Chla maximum and MEI/SAM did not change. One possible reason for not observing differences is that the short time series used here might not allow distinguishing the respective influence of the oscillations.
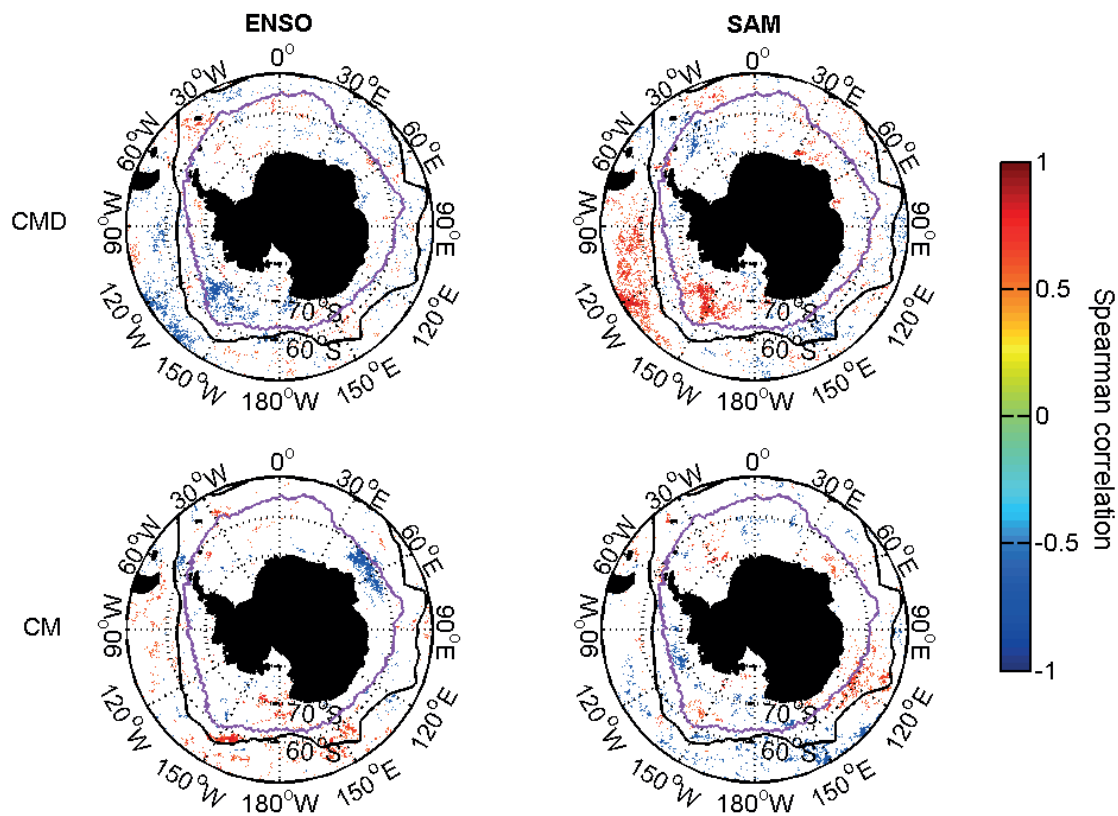
Figure 5.9. Correlation coefficients of the standardized anomalies of date of Dia-Chla maximum (CMD) and Dia-Chla maximum (CM) vs. ENSO (MEI) and SAM (AAO) indices. Only statistically significant trends (p < 0.05) are shown. Black and purple lines indicate the mean position of the Polar Front and maximum sea ice extent over 1997-2012, respectively.

5.3.2.2.2 Composite maps of anomalies

The composite maps of the anomalies of bloom start date, Dia-Chla maximum and bloom duration are shown in Figures 5.10, 5.11 and A6, respectively, and provide insight onto the magnitude of the anomalies during the ENSO and SAM events. In the seasonal ice zone there are two regions with inverse patterns and high anomalies of bloom start date: the Weddell Sea region (white dashed box) and the sector between 120°W and 180°W (white box), north of 70°S. In the Weddell Sea, El Niño/negative SAM years are characterized by later start, shorter duration and slightly higher biomass, which are likely a response of more extensive ice cover in these years (Kwok and Comiso 2002; Lefebvre et al. 2004). In the sector between 120°W and 180°W the pattern is inversed.

Alvain et al. (2013) showed that, on average, the frequency of diatom dominance (derived using the PHYSAT) is higher in positive phases of SAM as a response of more intense winds and nutrient supply. Their spatial pattern of differences between monthly mean diatom frequency dominance during positive and negative SAM events reveal large areas with negative differences as well (see Figure 3a in Alvain et al. 2013). To compare our results with those from Alvain et al. (2013), we calculated the differences between the composite maps of Dia-Chla maximum anomalies during positive SAM and negative SAM phases (not shown). Our spatial pattern is very similar to that presented in their study for most of the region.
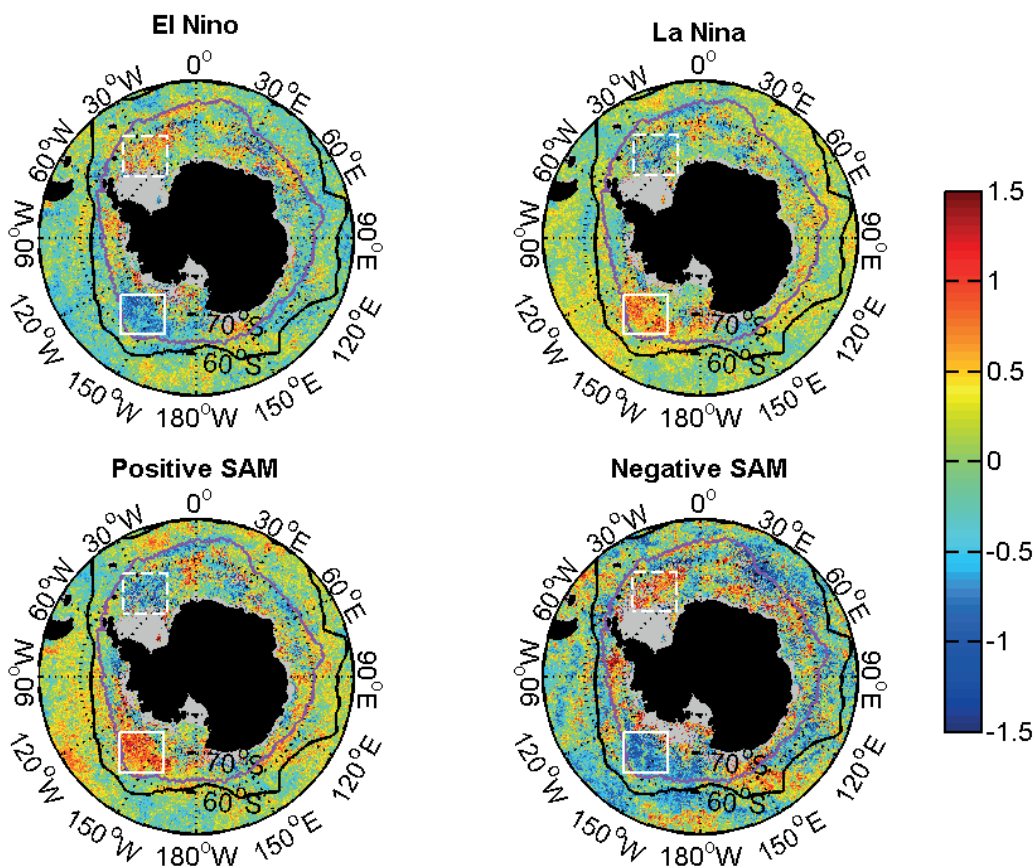
Figure 5.10. Composites of bloom start date (BSD) standardized anomalies during El Niño

(N=6), La Niña (N=8), positive SAM (N=7) and negative SAM (N=4) years. Grey areas represent missing data. Black lines show the mean position of the Polar Front (Sallee et al. 2008) over 1997-2012. Purple line displays the mean position of the maximum sea ice extent (Fetterer et al. 2002) over 1997-2012. The white boxes depict the Weddell Sea region (dashed) and the sector between 120°W and 180°W.
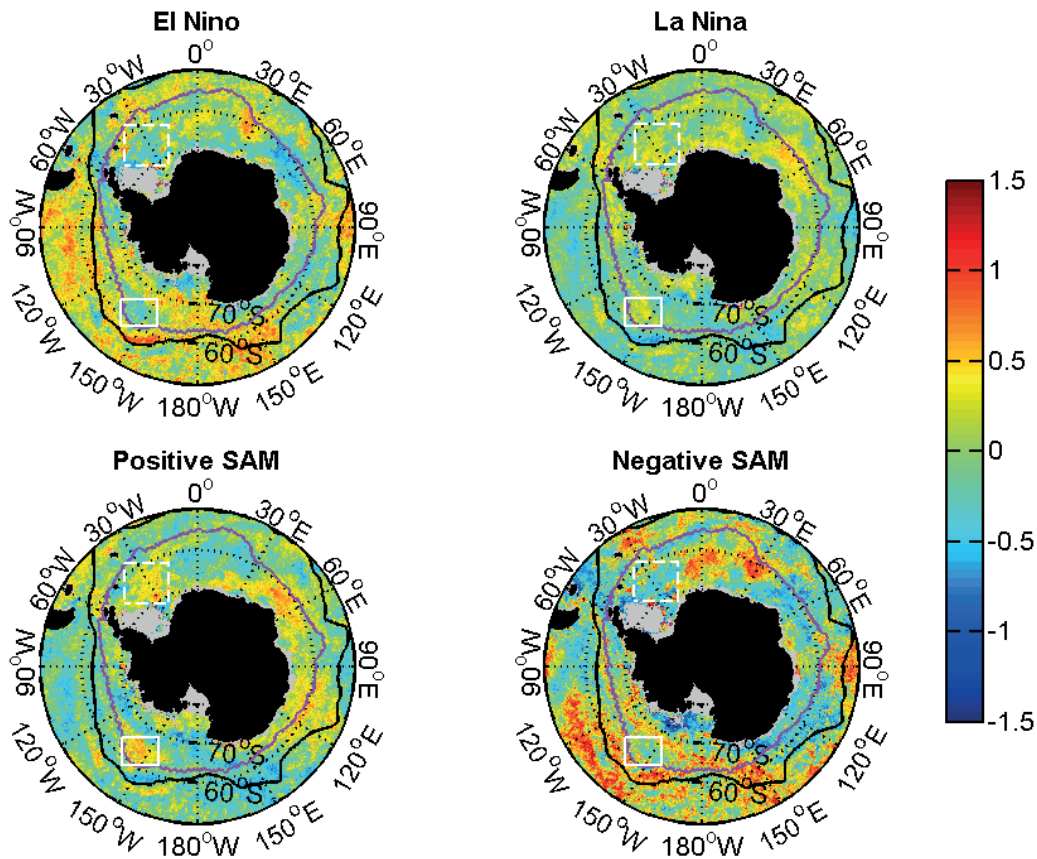
Figure 5.11. Same as Figure 5.10 but for Dia-Chla maximum.

5.3.2.2.2.1 Composite maps of anomalies in amplified years

In addition to these anomalous years influenced by ENSO and SAM, the effect of these oscillations can be amplified when El Niño (La Niña) coincides with negative (positive) phase of SAM. During the period studied, three years (2002/2003, 2003/2004, and 2009/2010) were characterized by El Niño co-occurring with negative phase of SAM, and six years (1998/1999, 1999/2000, 2007/2008, 2008/2009, 2010/2011, 2011/2012) of La Niña and positive phase of SAM (Figure 5.1). The composite maps of bloom start date and Dia-Chla maximum for the amplified years are presented in the appendix (Figure A7). Unfortunately, because of the short length of our time series it was not possible to distinguish between amplified and non-amplified years.

5.4 Concluding remarks

We have used a solid and widely applied method to investigate phytoplankton phenology from ocean colour data (Brody et al. 2013; Henson et al. 2009; Henson and Thomas 2007; Racault et al. 2012; Siegel et al. 2002; Thomalla et al. 2011). This method differs from Behrenfeld (2010), where the bloom starts when the net phytoplankton growth rate becomes positive. Another difference is that Behrenfeld (2010) accounts for the dilution effect; when the mixed layer is deeper than the Z_{eu} the phytoplankton concentration is diluted and that can mask an increase in the net growth rate (Behrenfeld 2010). Although Z_{eu} can be accurately retrieved from satellite data in the SO (Soppa et al. 2013), the uncertainties of the mixed layer depth datasets at weekly or monthly resolution has still to be investigated. In addition, in our analysis the start of the bloom was defined as an increase of Chla over a threshold, after identifying the peak of biomass. An advantage of this method is that it is more suitable for studying the mismatch hypothesis between phytoplankton and higher trophic levels (Brody et al. 2013) because it is based on the timing of the maximum biomass. On the other hand, by this definition there will always be a bloom, even in regions where the amplitude of the Chla is very low, as between 120°E and 150° E (Figure 5.5).

The advantage of using satellite data to study phytoplankton phenology is widely recognized. The high temporal resolution allows investigating the full development of the bloom and the spatial coverage enables to compare different regions simultaneously in time. However, there are still knowledge gaps related to the ocean colour data that can affect the phenology studies and where further investigations are needed. One limitation is that some regions of the SO present a deep Chla maximum (~ 60 - 90 m) which is not seen by the sensor (e.g. southern Indian and Pacific sectors of the SO, Holm-Hansen et al. 2005). This implies that subsurface blooms deeper than the first optical depth are not accounted for in the satellite data. A second limitation is that due to gaps in satellite data the date of the actual Chla maximum, for example, may be missed (Kahru et al. 2011). In fact, Racault et al. (2014) showed that the error in the date of Chla maximum arising from gappy datasets is nearly two months (global average). Data gaps also reduce the length of the times series and the significance of the statistical tests. We have attempted to minimize this error by filling the gaps by linear temporal interpolation and through the use of merged satellite Chla product. For example, in January 2012 the average number of observations in the SO improved by 45% using the merged satellite Chla data than if only using MODIS data. Another way to overcome this issue is to apply techniques such as the Data Interpolating Empirical Functions method (DINEOF, Alvera-Azcarate et al. 2007) to reconstruct the missing data fields. Thus, a future goal is to reprocess the dataset of diatom concentration with the DINEOF to obtain a gap-free dataset and to investigate the impact of missing data to determine the phenological indices. This will make possible to estimate trends for the indices that remained not analyzed because of the lack of gap-free time series and it will possibly increase the significance of the correlations discussed in the section 5.3.2.2.

Phytoplankton blooms phenology has been studied before using satellite Chla data. However, by looking at the total Chla provided by the satellite the contribution of all different PFTs are taken into account. Using satellite-derived diatom concentration, we were able to look specifically at the fraction or concentration of Chla that belongs to diatoms. We investigated the mean patterns

of the diatom phenology, but the most interesting results are related to the interannual variability. We find a clear correspondence between ENSO and SAM and the phenology of diatoms, as revealed by the correlation and the anomaly composite maps. These climate oscillations have different effects among the regions of the SO. It is also evident that different phases in ENSO/SAM have opposite effects in the diatom phenology. These results emphasize the influence of climate oscillations over the SO and in the diatom phenology, which may be enhanced in amplified years. For the first time these findings are described for the SO.

The mechanisms by which ENSO and SAM climate oscillations are associated with diatom phenology will be investigated in a following study. From the literature we obtained the evidence of the complex and strong link between these components through changes in the environment (e.g. sea ice concentration, sea surface temperature, mixing); our next step is to quantify it. This can be performed for example, by examining the composite maps of sea ice concentration during the different phases of ENSO/SAM and also looking at correlations between the sea ice concentration and the phenological indices. Besides that, we did not found a literature which fully covers the period we investigated.

In addition, such investigation needs a comprehensive dataset including not only information on SST and PAR, as usual used in phytoplankton phenology studies since these variables are freely available from remote sensing, but also water column mixing, sea ice concentration, dissolved iron and silicate for example. Combining remote sensing and model data can help to explain the missing link between climate oscillations, environmental anomalies and diatom phenology. A better understanding of diatom phenology also requires a consideration of the grazing pressure, which unfortunately cannot be easily estimated, at least not at the temporal resolution required, and probably for this reason its role on the diatom phenology is not well known.

Last, the knowledge of other PFT forming blooms in the SO, mainly haptophytes, is important to understand phytoplankton community shift and the factors controlling it. *E. huxleyi* are known to occur along the "Great Calcite Belt" in the SO and dense blooms are often observed at the shelf break and off the Patagonian shelf after the spring bloom of diatoms. Moreover, while is generally accepted that diatoms dominate the spring bloom in the SO (Smetacek 1985) this might not be true everywhere as for the case of the spring bloom of *P. antarctica* in the Ross Sea (Smith et al. 2012).

Chapter 6

Synthesis and major outcomes

6   Synthesis and major outcomes

Changes in the SO are occurring, regardless if driven by natural or anthropogenic climate variability. Among the most remarkable changes is the increase in the sea ice cover by 5% per decade in the Ross Sea and the decrease by 7.1% per decade in the Bellingshausen/Amundsen Sea (Comiso 2010). An important question which needs to be addressed in a changing SO is how these changes are reflected in the phytoplankton composition, distribution and NPP and hence in the biogeochemical cycles and ecosystem functioning.

The SO is, like the North Atlantic, a major region for uptake and long term storage of anthropogenic atmospheric CO_2 (Hauck and Völker 2015; Sabine et al. 2004; Takahashi et al. 2012). Part of the uptake is biology-driven. Maier-Reimer et al. (1996) addressed the importance of the marine biological pump in the global atmospheric CO_2 concentrations. Using a coupled ocean-biogeochemical model, they found that without the biological uptake the CO_2 concentration in the atmosphere would rise ~100 ppm in 50 years, which translates to an increase of 213 PgC. For comparison, the preindustrial concentration was 280 ppm in the year 1800 and the current concentration (March 2015) is 400.83 ppm (Dlugokencky and Tans 2015); that is an increase of 120 ppm (255 PgC) in 215 years. The current level is also considerably higher than the concentration of 172-300 ppm for the last 800.000 years measured in ice cores from Antarctica (Luthi et al. 2008).

The projected consequences of increasing anthropogenic atmospheric CO_2 in the SO include strengthening of the westerly winds, ocean acidification, warming and freshening of surface waters, enhanced stratification and decrease in sea ice extent (Bindoff et al. 2011; IPCC 2014). It is argued that the enhanced stratification will reduce the vertical supply of nutrients to the surface and lead to a community shift from large to smaller phytoplankton (Bopp et al. 2005; Finkel et al. 2010). This view is not supported by Kemp and Villareal (2013). The authors argue that diatoms, which are in general medium and large phytoplankton, survive in a wide variety of conditions and may adapt to a more stratified ocean due to their ability to grow in deeper layers under low light conditions, to migrate in the water column by physiologically controlling their buoyancy, thus enhancing the nutrient uptake. Further, open ocean diatoms can reduce their requirement of iron under iron limiting conditions (Armbrust 2009).

Alongside anthropogenic-induced change, much of the variability in the SO has been associated to natural climate oscillations ENSO and SAM (Alvain et al. 2013; Arrigo and van Dijken 2004; Hauck et al. 2013; Kwok and Comiso 2002; Lovenduski 2007; Lovenduski and Gruber 2005). SAM has shown a positive trend towards positive events (Pohl et al. 2010; Sallee et al. 2010; Thompson et al. 2011) and the coupling with ENSO may strengthen the anomalies generated by SAM in the SO (Fogt et al. 2011).

Satellite observations provide the means for monitoring large scale changes in the SO productivity; however, the separation of natural from anthropogenic influence is difficult using ocean colour remote sensing. Short times series are currently available relative to the large interannual variability intrinsic to phytoplankton (Beaulieu et al. 2013; Henson et al. 2010). Henson et al. (2010) have shown that longer times series (~ 40 years) are required to detect climate change trends on the satellite ocean productivity in the SO; a challenging task that

depends on the endurance of the satellite missions. The merging of data from different sensors as performed by the ESA GlobColour and ESA OC CCI projects is a current effort to achieve this aim which depends on simultaneous data acquisition, cross-calibration between sensors and data merging (Beaulieu et al. 2013). Unfortunately, to date, only MODIS-Aqua, launched mid of 2002, and the Visible Infrared Imager Radiometer Suite (VIIRS) launched end of 2011, are operational at global scale, and there is a growing concern on MODIS-Aqua which is experiencing sensor degradation since 2011.

Another important application of ocean colour is data assimilation and validation of marine biogeochemical models (Robinson 2010). Furthermore, the use of satellite data in conjunction with information derived from models can provide a more complete description of the biogeochemical processes in the water column and on the export of carbon to deeper layers. *In situ* data is also certainly very useful, but those are rather sparse and unable to solve the spatial and temporal variability required to study these processes. A promising technology is the Bio-Argo float, which is another way of obtaining continuous ocean optical information. Argo floats have now for 15 years measured profiles of temperature and salinity at daily temporal resolution in the SO and recently, they have been equipped with several sensors to measure bio-optical properties of the oceans (e.g. Chla, PAR, CDOM). These Bio-Argo floats are still experimental but will potentially improve the number of bio-optical observations in the SO and together provide information on the vertical structure of these properties (http://www.euroargo-edu.org/explore/argoeu_2.php).

The synergistic use of ocean colour remote sensing, biogeochemical models and *in situ* observations provide complementary information and they have to walk together towards their improvement. From the ocean colour perspective, it implies that we do not only need sustained and consistent ocean colour observations, but also to understand the typical patterns of phytoplankton community composition and NPP in the SO. To assess the effects of unusual events on ocean biology we need first to understand its natural variability; a baseline against which to compare these events (Henson 2014).

This thesis was set out to investigate ocean colour retrievals and phytoplankton dynamics in the SO and it was developed as a multidisciplinary work using *in situ* and remote sensing data. The studies developed here have moved forward our knowledge of ocean colour in the SO and contributed to a better understanding of the ocean biogeochemical cycle from the ocean colour perspective by adding new information on the uncertainties in the input terms of NPP models, on the estimation of diatoms abundance and on the variability of diatoms phenology.

For the first time uncertainties of ocean colour retrievals of Z_{eu} have been investigated in the SO (Chapter 3; published in Soppa et al. 2013). Two Z_{eu} retrievals (Z_{eu}-Chla and Z_{eu}-IOP) from SeaWiFS and MODIS have been validated with *in situ* measurements of Z_{eu}. The results showed that both methods and sensors provide consistent estimates of satellite Z_{eu}, although satellite retrievals of Chla have substantial uncertainties. Spatial differences between Z_{eu} satellite products have been found and it is likely that these differences were not detected in the validation effort due to the limited and uneven distribution of the *in situ* measurements. Therefore, we reinforce the importance of looking at spatial patterns, together with *in situ* validation for comparing ocean colour data retrieved from different approaches. Thus, the choice of the Z_{eu} product led to substantial differences in the satellite NPP over specific regions of the SO. In addition, a parallel

objective of this study was to examine the uncertainties of satellite a_{ph} as it is an input term in the ABPM NPP model as well. As for Z_{eu}, the validation of satellite a_{ph} was the first efforts to investigate uncertainties in the SO and the results presented here can serve as a reference for future studies.

To which extent one Z_{eu} product leads to improved NPP retrievals in comparison to the other one is a task for future research and could potentially suggest the more appropriate Z_{eu} satellite product for a given NPP model. A similar investigation could be conducted for a_{ph} and, in addition, by examining the combined effect of the uncertainties of different input terms in the NPP estimation, as performed by Saba et al. (2011). However, Z_{eu}, a_{ph} and the ABPM were not considered in their study; neither the use of different algorithms to retrieve the input terms of the NPP models.

Moreover, the skill of satellite NPP models can be improved by separating the contribution of different PFTs. Biogeochemical models (e.g. NOBM - NASA Ocean Biogeochemical Model, Gregg and Casey 2007, PISCES - Pelagic Interaction Scheme for Carbon and Ecosystem Studies, Aumont and Bopp 2006) frequently represent the community structure by including the information of one or more PFTs allowing to investigate their specific contribution to the NPP and biogeochemical cycles. Few ocean colour studies (Uitz et al. 2009a, 2010; Uitz et al. 2009b; Uitz et al. 2012) have so far focused on this topic due to the difficulty in estimating the Chla and the photophysiological properties specific to each phytoplankton group (Uitz et al. 2010), but their importance is acknowledged. There is an increasing effort in the ocean colour community to develop and improve PFTs retrievals using remote sensing. Equally important is the tuning of global satellite PFT approaches to regional application. Today global scale studies and parametrizations usually fail to fully capture important regional differences in the ocean properties which influence the phytoplankton community composition (Brito et al. 2015).

Regarding this limitation, the second study, presented in Chapter 4 and published in Soppa et al. (2014), has identified that the satellite derived diatom abundance using the ABA is underestimated in the SO. This conclusion has been achieved by revising the global ABA with a new *in situ* dataset that included more phytoplankton pigment samples from the SO. It was observed that the global relationship between Chla and the *f*-Diatom is not appropriate for the SO. A new global function that accounts for the relatively high concentration of diatoms in low Chla waters was proposed, improving the retrievals in the SO using the global parametrization, but leading to an overestimation in other regions. Therefore, and for the first time, a regional ABA model for the SO was developed which further improved estimation of the diatom abundance in the region.

Yet, the remoteness of the SO is still a limitation. Research cruises in the SO tend to focus on regions with elevated phytoplankton concentration and close to the continents for logistic reasons and scientific interests (e.g. sea ice, carbon export). Again, the development of new field observation systems as Bio-Argo floats and gliders could help to obtain a better spatial and temporal coverage in the SO. It is a long term aim to obtain a proper *in situ* bio-optical data set of the SO that once achieved will allow to investigate the spatial differences observed in the first study and will improve global and regional parametrizations of the relationship between Chla and diatoms developed in the second study.

With the information of PFTs from satellite, the next stage is to investigate their dynamics. The third study analyzed the diatom bloom phenology over 15-yr (Chapter 5) using the regional model

to retrieve the concentration of diatoms in the SO. Although important, phenology studies focused on diatoms have not been conducted so far. The diatom bloom phenology was investigated using ten indices that described the timing, duration and magnitude of the bloom at different stages. The mean patterns revealed that diatom blooms are spatially and temporally heterogonous and are associated with the position of the SACCF and the maximum sea ice extent. Earlier start and maximum were observed in blooms north of the SACCF - outside the seasonal ice zone. Their duration is also longer than blooms formed in the seasonal ice zone. On the other hand, blooms around Antarctica are more intense blooms, with shorter duration and higher biomass, than blooms outside this region.

In addition to the mean patterns, knowledge was gained in the relationship between large scale climate oscillations (ENSO and SAM) and diatom bloom phenology. The robust signals of ENSO and SAM observed in the phenological indices across different regions of the SO indicated influence of these climate oscillations on the environment and diatom phenology. A follow-up study should address in more detail the underlying mechanisms associated with changes in the diatom phenology, for example, by looking at correlations and composite maps of sea ice concentration or sea surface temperature and diatom phenology during ENSO and SAM events. Once available, a longer time series of data should be employed likewise to examine trends and to better distinguish between ENSO and SAM influence in the region.

If changes in the phytoplankton bloom phenology can be monitored, it may serve as indicator for subsequent changes in the food web, productivity and ocean biogeochemistry. Future research should focus on optimizing the ABA to other PFTs to expand the understanding on their dynamics and interaction with other PFTs. However, since the ABA method is based on the assumption that diatoms dominate at high Chla, it might incorrectly identify other PFTs occurring at high concentrations. A combination with data provided by the PhytoDOAS method applied to hyperspectral data, for example, can lead to a more objective characterization of the PFTs.

Recently the SynSenPFT Project founded by ESA (http://www.awi.de/en/research/young_investigators/helmholtz_university_young_investigators_g roups/phytooptics/projects/synsenpft/), under the Scientific Exploration of Operational Missions Program, has been initiated. One of the main objectives is to develop improved PFT products by the synergistic use of low spatial resolution hyperspectral data with high spatial resolution multispectral data. Satellite retrievals of diatom, coccolithophores and cyanobacteria will be developed using the ABA and PhytoDOAS methods. By the choice of these two methods, the high spatial resolution of the PFTs derived with ABA and the high spectral resolution data used by PhytoDOAS to derive PFTs can be exploited.

Ocean colour remote sensing has proven to be a valuable tool to adequately examine primary production and the phytoplankton composition in a changing SO. In the future, long term high quality time series will be available for further investigations in the topic of this thesis given the continuity of the satellite space programs. The upcoming multispectral and hyperspectral sensors, the Ocean Land and Color Instrument (OLCI) on Sentinel-3 and the Tropospheric Monitoring Instrument (TROPOMI) on Sentinel-5P, are expected to be launched in October 2015 and 2016 respectively, as part of the ESA Sentinels mission. They will support the challenging task of building a long and accurate global data record from ocean colour remote sensing.

Appendix
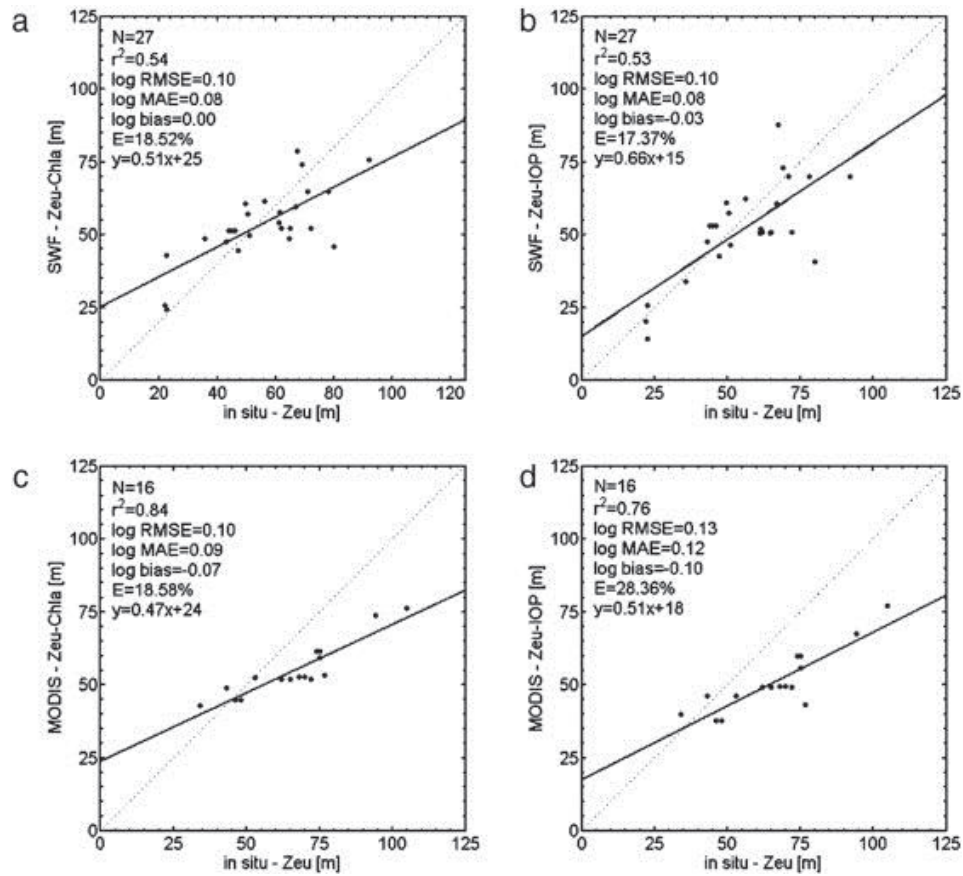
Figure A1. Scatterplots of satellite Z_{eu}-Chla and Z_{eu}-IOP against *in situ* Z_{eu} south of 60°S. The solid line represents the regression and the dotted line represents the 1:1 line as reference.
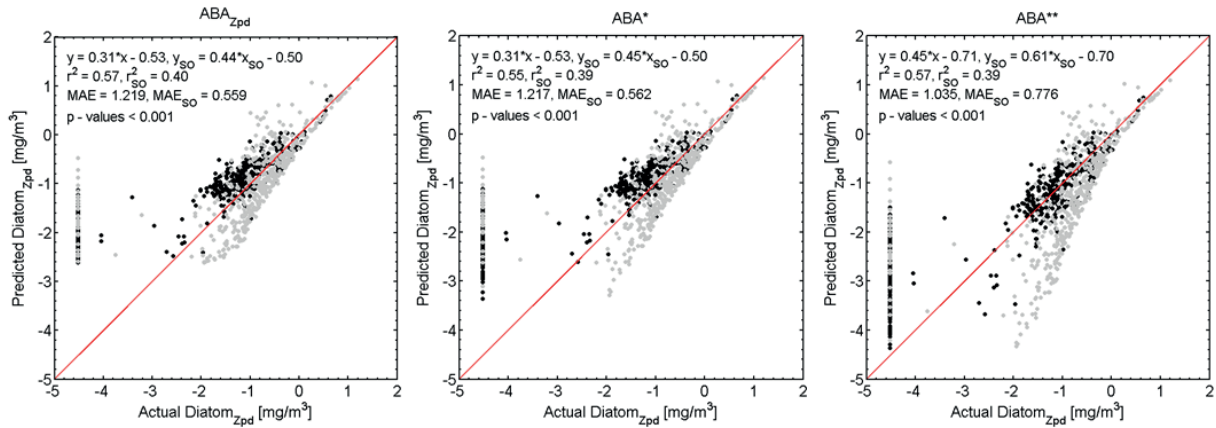
Figure A2. Scatterplot of the validation for the global DP_{Zpd} dataset (N= 1182): **(a)** new model (ABA_{Zpd}), **(b)** model of Hirata et al. (2011) parameterized with the DP_{Zpd} dataset (ABA*) and **(c)** original model and fitting parameters of Hirata et al. (2011) (ABA**). The samples located in the SO are presented in grey (N = 460), together with the statistics of the validation. The red line represents the 1:1 line. The statistics were calculated with $\log_{10}$ transformed data (e.g. $\log_{10}(y+0.00003)$).
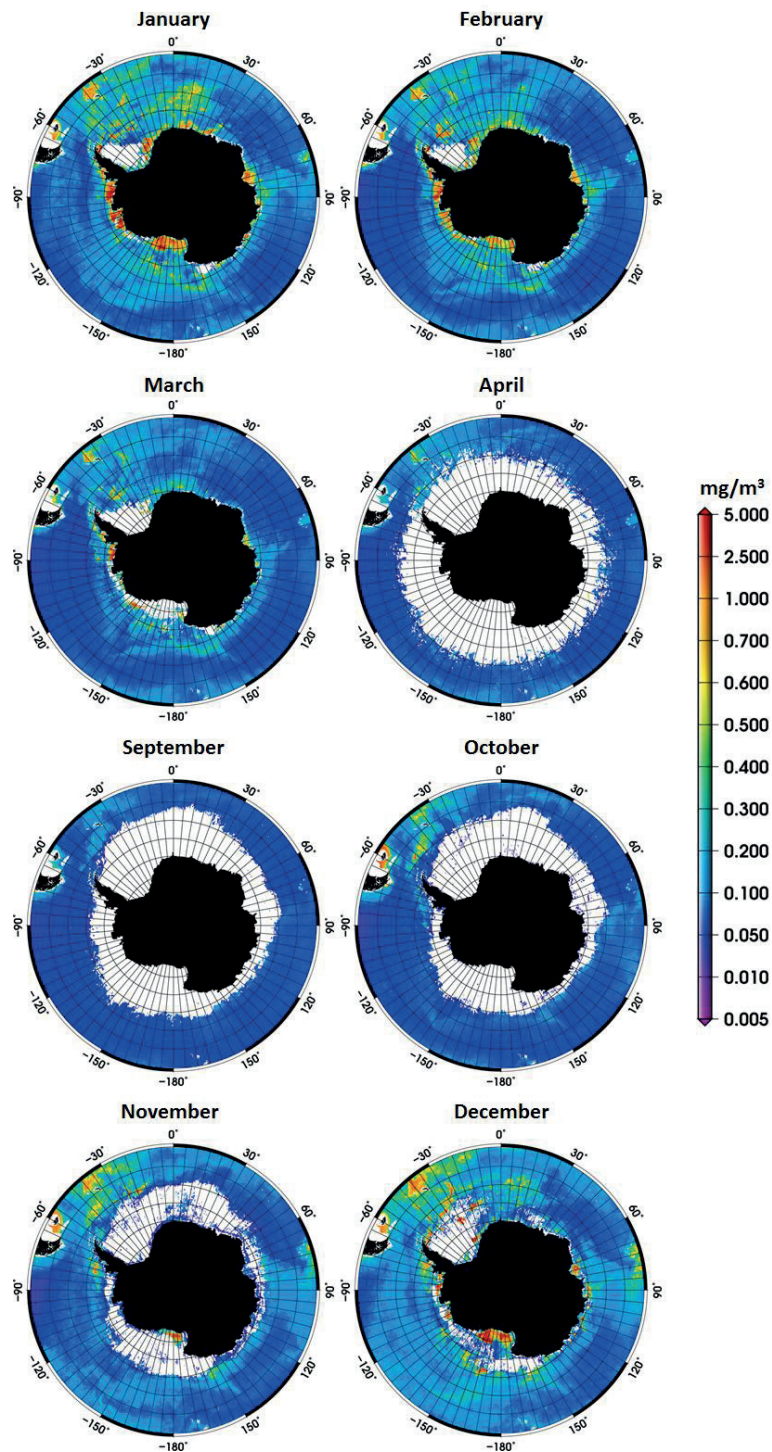
Figure A3. Climatology of TChla$_{Zpd}$ of diatoms (mg m^{-3}) using the regional algorithm for the SO based on 2003-2013 period. The austral winter months of May, June, July and August are not presented due to too few number observations available in these months. White areas correspond to waters with depths shallower than 200 m or without satellite information.
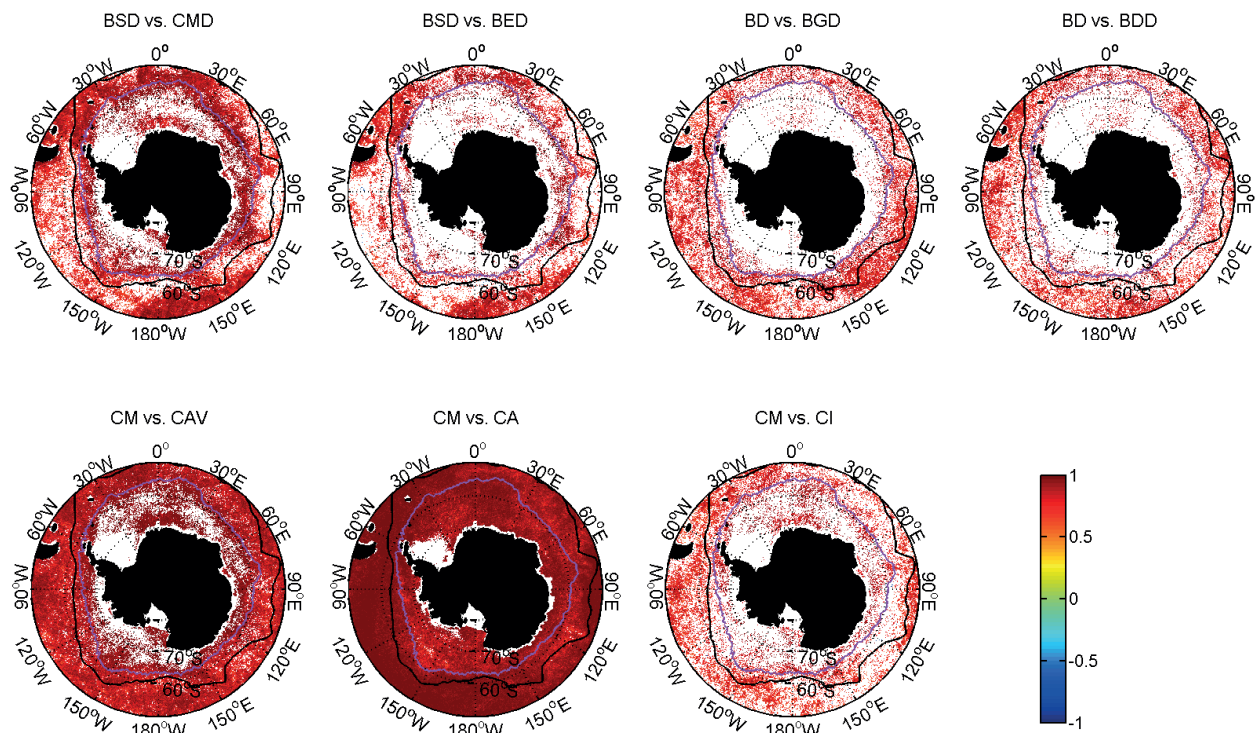
Figure A4. Spearman correlation coefficients between the time series of phenological indices (15-yr, 1997 – 2012): bloom start date (BSD), date of Dia-Chla maximum (CMD), bloom end date (BED), bloom growth duration (BGD), bloom decline duration (BDD), bloom duration (BD), Dia-Chla maximum (CM), Dia-Chla amplitude (CA), Dia-Chla averaged BGD (CAV), Dia-Chla integrated over BGD (CI). Only statistically significant trends (p < 0.05) are shown. White areas correspond to non-significant correlations or missing data. Black and purple lines indicate the mean position of the Polar Front and the mean position of the maximum sea ice extent over 1997-2012, respectively.
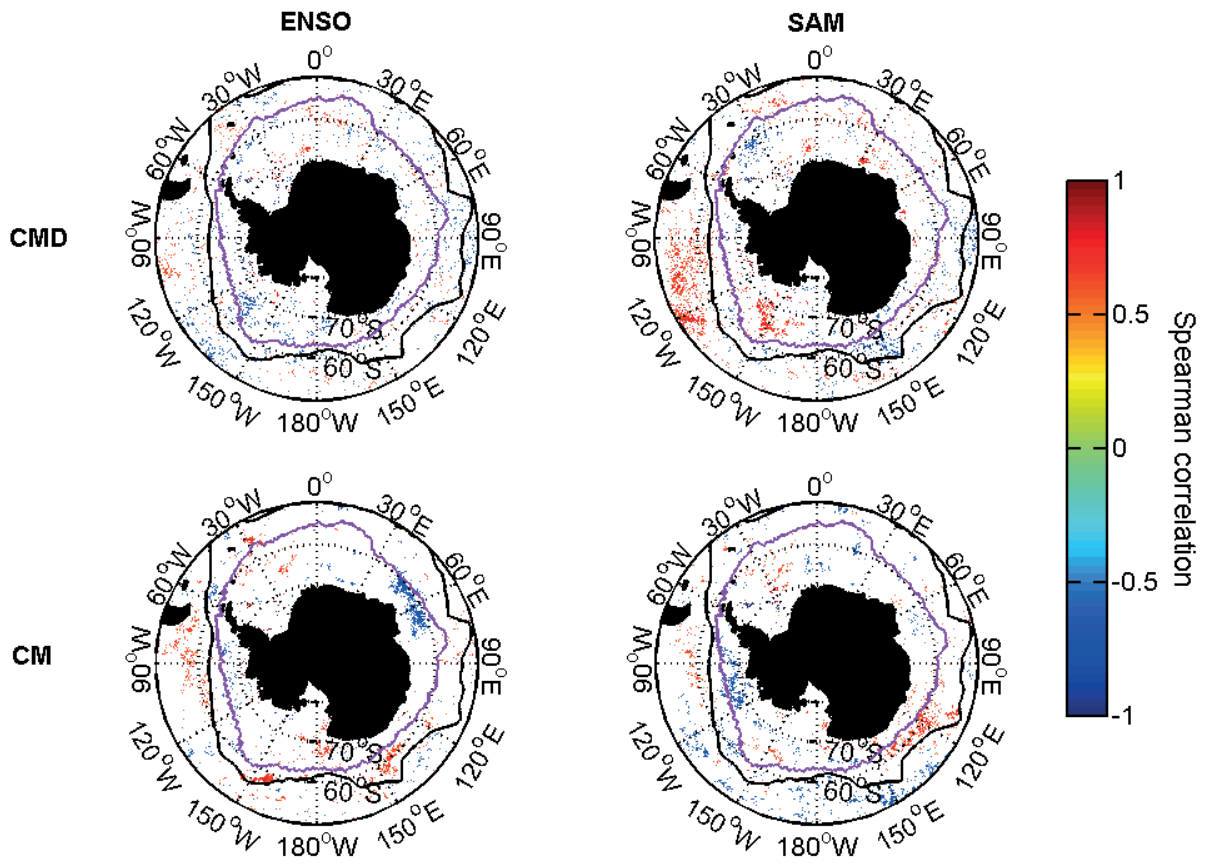
Figure A5. Partial correlation coefficients of the standardized anomalies of date of Dia-Chla maximum (CMD) and Dia-Chla maximum (CM) vs. ENSO (MEI) and SAM (AAO) indices. Only statistically significant trends ($p < 0.05$) are shown. Black and purple lines indicate the mean position of the Polar Front and the mean position of the maximum sea ice extent over 1997-2012, respectively.
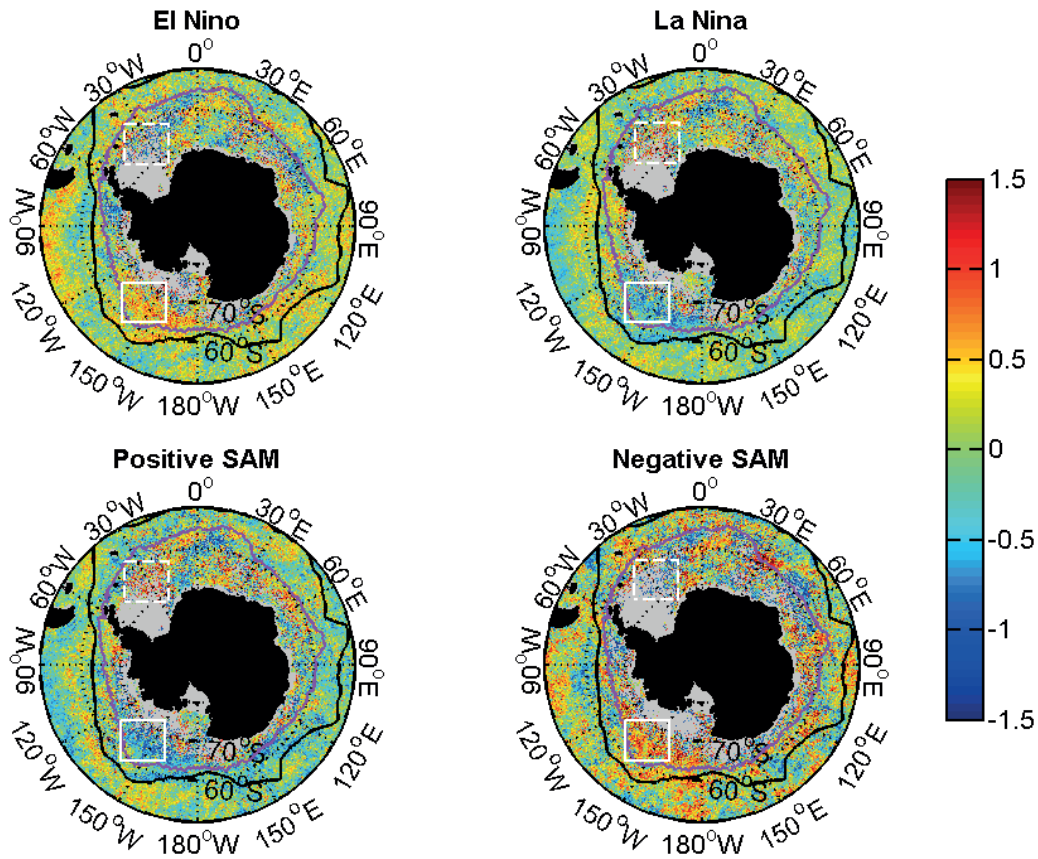
Figure A6. Composites of bloom duration standardized anomalies during El Niño (N=6), La Niña (N=8), positive SAM (N=7) and negative SAM (N=4) years. Grey areas represent missing data. Black lines show the mean position of the Polar Front (Sallee et al. 2008) over 1997-2012. Purple line displays the mean position of the maximum sea ice extent (Fetterer et al. 2002) over 1997-2012. The white boxes depict the Weddell Sea region (dashed) and the sector between 120°W and 180°W.
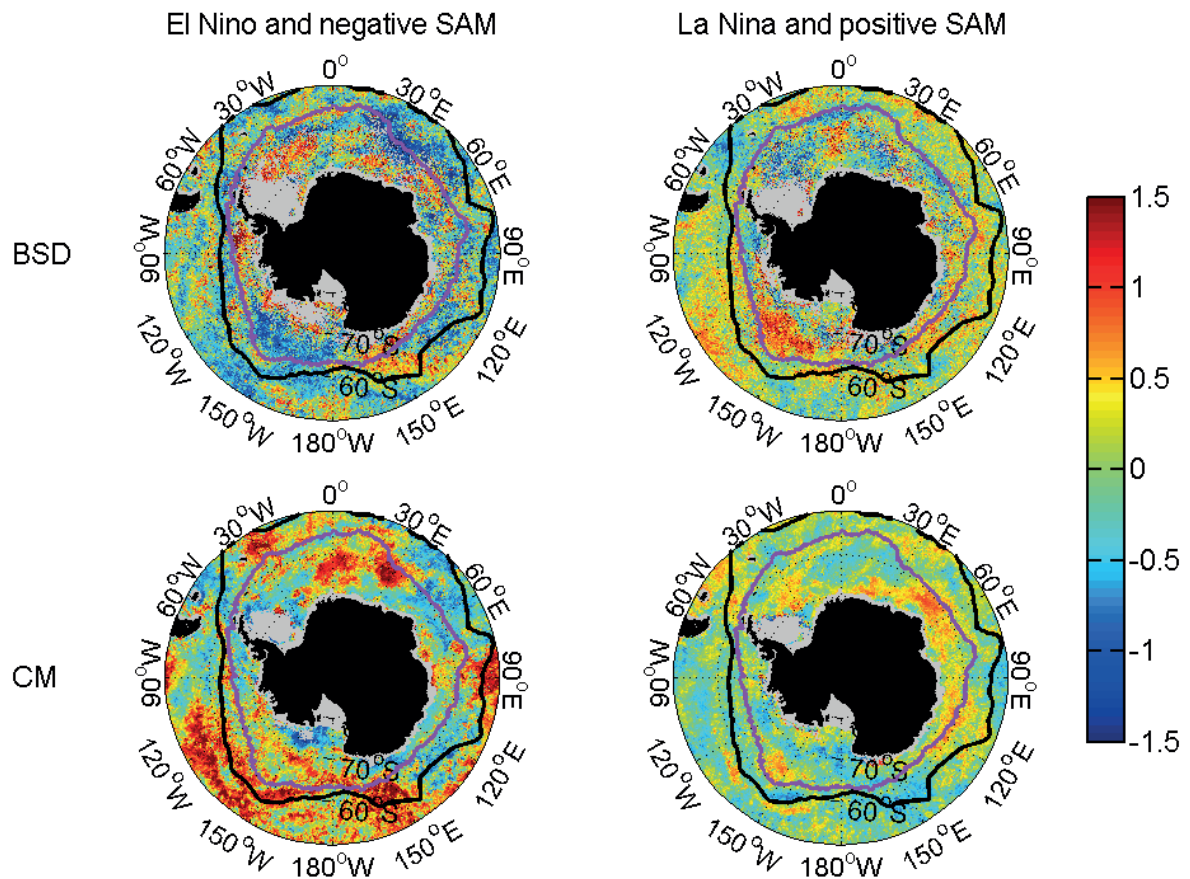
Figure A7. Composites of bloom start date (BSD) and Dia-Chla maximum (CM) standardized anomalies during amplified years. Left plot: El Niño and negative SAM (N=3). Right plot: La Niña and positive SAM (N=6). Grey areas represent missing data. Black and purple lines indicate the mean position of the Polar Front and the mean position of the maximum sea ice extent over 1997-2012, respectively. The white boxes depict the Weddell Sea region (dashed) and the sector between 120°W and 180°W.

References

Alvain, S., Le Quere, C., Bopp, L., Racault, M.F., Beaugrand, G., Dessailly, D., & Buitenhuis, E.T. (2013). Rapid climatic driven shifts of diatoms at high latitudes. *Remote Sensing of Environment, 132*, 195-201

Alvain, S., Moulin, C., Dandonneau, Y., & Breon, F.M. (2005). Remote sensing of phytoplankton groups in case 1 waters from global SeaWiFS imagery. *Deep-Sea Research Part I-Oceanographic Research Papers, 52*, 1989-2004

Alvain, S., Moulin, C., Dandonneau, Y., & Loisel, H. (2008). Seasonal distribution and succession of dominant phytoplankton groups in the global ocean: A satellite view. *Global Biogeochemical Cycles, 22*

Alvera-Azcarate, A., Barth, A., Beckers, J.M., & Weisberg, R.H. (2007). Multivariate reconstruction of missing data in sea surface temperature, chlorophyll, and wind satellite fields (vol 112, art no C03008, 2007). *Journal of Geophysical Research-Oceans, 112*

Amante, C., & Eakins, B.W. (2009). ETOPO1 1 Arc-Minute Global Relief Model: Procedures, Data Sources and Analysis. *NOAA Technical Memorandum NESDIS NGDC-24*: National Geophysical Data Center, NOAA

Arar, E.J., & Collins, G.B. (1997). *In Vitro Determination of Chlorophyll a and Pheophytin a in Marine and Freshwater Algae by Fluorescence*. Cincinnati, Ohio: National Exposure Research Laboratory, Office of Research and Development, U. S. Environmental Protection Agency

Armbrust, E.V. (2009). The life of diatoms in the world's oceans. *Nature, 459*, 185-192

Arrigo, K.R., Lowry, K.E., & van Dijken, G.L. (2012). Annual changes in sea ice and phytoplankton in polynyas of the Amundsen Sea, Antarctica. *Deep Sea Research Part II: Topical Studies in Oceanography, 71–76*, 5-15

Arrigo, K.R., van Dijken, G., & Long, M. (2008). Coastal Southern Ocean: A strong anthropogenic CO2 sink. *Geophysical Research Letters, 35*, L21602

Arrigo, K.R., & van Dijken, G.L. (2004). Annual changes in sea-ice, chlorophyll a, and primary production in the Ross Sea, Antarctica. *Deep-Sea Research Part Ii-Topical Studies in Oceanography, 51*, 117-138

Assmy, P., Smetacek, V., Montresor, M., Klaas, C., Henjes, J., Strass, V.H., Arrieta, J.M., Bathmann, U., Berg, G.M., Breitbarth, E., Cisewski, B., Friedrichs, L., Fuchs, N., Herndl, G.J., Jansen, S., Kragefsky, S., Latasa, M., Peeken, I., Rottgers, R., Scharek, R., Schuller, S.E., Steigenberger, S., Webb, A., & Wolf-Gladrow, D. (2013). Thick-shelled, grazer-protected diatoms decouple ocean carbon and silicon cycles in the iron-limited Antarctic Circumpolar Current. *Proceedings of the National Academy of Sciences of the United States of America, 110*, 20633-20638

Audran, S., Faure, B., Mortini, B., Aumont, C., Tiron, R., Zinck, C., Sanchez, Y., Fellous, C., Regolini, J., Reynard, J., Schlatter, G., & Hadziioanno, G. (2006). Study of dynamical

formation and shape of microlenses formed by the reflow method. *Advances in Resist Technology and Processing Xxiii, Pts 1 and 2, 6153*, U1616-U1625

Beaulieu, C., Henson, S.A., Sarmiento, J.L., Dunne, J.P., Doney, S.C., Rykaczewski, R.R., & Bopp, L. (2013). Factors challenging our ability to detect long-term trends in ocean chlorophyll. *Biogeosciences, 10*, 2711-2724

Behrenfeld, M.J. (2010). Abandoning Sverdrup's Critical Depth Hypothesis on phytoplankton blooms. *Ecology, 91*, 977-989

Behrenfeld, M.J. (2014). Climate-mediated dance of the plankton. *Nature Climate Change, 4*, 880-887

Behrenfeld, M.J., & Boss, E.S. (2014). Resurrecting the Ecological Underpinnings of Ocean Plankton Blooms. *Annual Review of Marine Science, Vol 6, 6*, 167-U208

Behrenfeld, M.J., Doney, S.C., Lima, I., Boss, E.S., & Siegel, D.A. (2013). Annual cycles of ecological disturbance and recovery underlying the subarctic Atlantic spring plankton bloom. *Global Biogeochemical Cycles, 27*, 526-540

Behrenfeld, M.J., & Falkowski, P.G. (1997). Photosynthetic rates derived from satellite-based chlorophyll concentration. *Limnology and Oceanography, 42*, 1-20

Bélanger, S., Ehn, J.K., & Babin, M. (2007). Impact of sea ice on the retrieval of water-leaving reflectance, chlorophyll a concentration and inherent optical properties from satellite ocean color data. *Remote Sensing of Environment, 111*, 51-68

Ben Mustapha, Z., Alvain, S., Jamet, C., Loisel, H., & Dessailly, D. (2014). Automatic classification of water-leaving radiance anomalies from global SeaWiFS imagery: Application to the detection of phytoplankton groups in open ocean waters. *Remote Sensing of Environment, 146*, 97-112

Bidigare, R.R., Ondrusek, M.E., Morrow, J.H., & Kiefer, D.A. (1990). Invivo Absorption Properties of Algal Pigments. *Ocean Optics X, 1302*, 290-302

Bindoff, N.L., Rintoul, A.J., Haward, M., Allison, I., & Press, A.J. (2011). Climate change and the Southern Ocean. *ACE CRC Oceans Position Analysis:* (p. 27). Hobart, Tasmania: The Antarctic Climate & Ecosystems Cooperative Research Centre

Blain, S., Queguiner, B., Armand, L., Belviso, S., Bombled, B., Bopp, L., Bowie, A., Brunet, C., Brussaard, C., Carlotti, F., Christaki, U., Corbiere, A., Durand, I., Ebersbach, F., Fuda, J.L., Garcia, N., Gerringa, L., Griffiths, B., Guigue, C., Guillerm, C., Jacquet, S., Jeandel, C., Laan, P., Lefevre, D., Lo Monaco, C., Malits, A., Mosseri, J., Obernosterer, I., Park, Y.H., Picheral, M., Pondaven, P., Remenyi, T., Sandroni, V., Sarthou, G., Savoye, N., Scouarnec, L., Souhaut, M., Thuiller, D., Timmermans, K., Trull, T., Uitz, J., van Beek, P., Veldhuis, M., Vincent, D., Viollier, E., Vong, L., & Wagener, T. (2007). Effect of natural iron fertilization on carbon sequestration in the Southern Ocean. *Nature, 446*, 1070-U1071

Bopp, L., Aumont, O., Cadule, P., Alvain, S., & Gehlen, M. (2005). Response of diatoms distribution to global warming and potential implications: A global model study. *Geophysical Research Letters, 32*

Borrione, I., Aumont, O., Nielsdottir, M.C., & Schlitzer, R. (2014). Sedimentary and atmospheric sources of iron around South Georgia, Southern Ocean: a modelling perspective. *Biogeosciences, 11*, 1981-2001

Borrione, I., & Schlitzer, R. (2013). Distribution and recurrence of phytoplankton blooms around South Georgia, Southern Ocean. *Biogeosciences, 10*, 217-231

Bracher, A., Vountas, M., Dinter, T., Burrows, J.P., Rottgers, R., & Peeken, I. (2009). Quantitative observation of cyanobacteria and diatoms from space using PhytoDOAS on SCIAMACHY data. *Biogeosciences, 6*, 751-764

Brewin, R.J.W., Sathyendranath, S., Hirata, T., Lavender, S.J., Barciela, R.M., & Hardman-Mountford, N.J. (2010). A three-component model of phytoplankton size class for the Atlantic Ocean. *Ecological Modelling, 221*, 1472-1483

Brewin, R.J.W., Sathyendranath, S., Lange, P.K., & Tilstone, G. (2014). Comparison of two methods to derive the size-structure of natural populations of phytoplankton. *Deep-Sea Research Part I-Oceanographic Research Papers, 85*, 72-79

Brito, A.C., Sa, C., Brotas, V., Brewin, R.J.W., Silva, T., Vitorino, J., Platt, T., & Sathyendranath, S. (2015). Effect of phytoplankton size classes on bio-optical properties of phytoplankton in the Western Iberian coast: Application of models. *Remote Sensing of Environment, 156*, 537-550

Brody, S.R., Lozier, M.S., & Dunne, J.P. (2013). A comparison of methods to determine phytoplankton bloom initiation. *Journal of Geophysical Research-Oceans, 118*, 2345-2357

Campbell, J., Antoine, D., Armstrong, R., Arrigo, K., Balch, W., Barber, R., Behrenfeld, M., Bidigare, R., Bishop, J., Carr, M.E., Esaias, W., Falkowski, P., Hoepffner, N., Iverson, R., Kiefer, D., Lohrenz, S., Marra, J., Morel, A., Ryan, J., Vedernikov, V., Waters, K., Yentsch, C., & Yoder, J. (2002). Comparison of algorithms for estimating ocean primary production from surface chlorophyll, temperature, and irradiance. *Global Biogeochemical Cycles, 16*

Carr, M.E., Friedrichs, M.A.M., Schmeltz, M., Aita, M.N., Antoine, D., Arrigo, K.R., Asanuma, I., Aumont, O., Barber, R., Behrenfeld, M., Bidigare, R., Buitenhuis, E.T., Campbell, J., Ciotti, A., Dierssen, H., Dowell, M., Dunne, J., Esaias, W., Gentili, B., Gregg, W., Groom, S., Hoepffner, N., Ishizaka, J., Kameda, T., Le Quere, C., Lohrenz, S., Marra, J., Melin, F., Moore, K., Morel, A., Reddy, T.E., Ryan, J., Scardi, M., Smyth, T., Turpie, K., Tilstone, G., Waters, K., & Yamanaka, Y. (2006). A comparison of global estimates of marine primary production from ocean color. *Deep-Sea Research Part Ii-Topical Studies in Oceanography, 53*, 741-770

Cheah, W., Taylor, B.B., Wiegmann, S., Raimund, S., Krahmann, G., Quack, B., & Bracher, A. (2013). Photophysiological state of natural phytoplankton communities in the South China Sea and Sulu Sea. *Biogeosciences Discuss., 10*, 12115-12153

Ciasto, L.M., Simpkins, G.R., & England, M.H. (2015). Teleconnections between Tropical Pacific SST Anomalies and Extratropical Southern Hemisphere Climate. *Journal of Climate, 28*, 56-65

Clarke, A.J. (2008). *An Introduction to the Dynamics of El Niño & the Southern*

Oscillation. New York, NY.: Academic Press

Comiso, J. (2010). *Polar Oceans from Space* New York, NY.: Springer Publishing

Cunningham, S.A. (2005). Southern Ocean circulation. *Archives of natural history, 32*, 265-280

Dierssen, H.M. (2010). Perspectives on empirical approaches for ocean color remote sensing of chlorophyll in a changing climate. *Proceedings of the National Academy of Sciences of the United States of America, 107*, 17073-17078

Dierssen, H.M., & Smith, R.C. (2000). Bio-optical properties and remote sensing ocean color algorithms for Antarctic Peninsula waters. *Journal of Geophysical Research: Oceans, 105*, 26301-26312

Dinter, T., Rozanov, V.V., Burrows, J.P., & Bracher, A. (2015). Retrieving the availability of light in the ocean utilising spectral signatures of Vibrational Raman Scattering in hyper-spectral satellite measurements. *Ocean Sci. Discuss., 12*, 31-81

Dlugokencky, E., & Tans, P. (2015). Trends in Atmospheric Carbon Dioxide. In: NOAA/ESRL

Duarte, C.M., & Cebrian, J. (1996). The fate of marine autotrophic production. *Limnology and Oceanography, 41*, 1758-1766

Durand, D. (2007). Full Validation Report. In A. Mangin, & S. Pinnock (Eds.), *GlobCOLOUR : An EO based service supporting global ocean carbon cycle research*

Edwards, M., & Richardson, A.J. (2004). Impact of climate change on marine pelagic phenology and trophic mismatch. *Nature, 430*, 881-884

Falkowski, P.G., Barber, R.T., & Smetacek, V. (1998). Biogeochemical controls and feedbacks on ocean primary production. *Science, 281*, 200-206

Falkowski, P.G., Katz, M.E., Knoll, A.H., Quigg, A., Raven, J.A., Schofield, O., & Taylor, F.J.R. (2004). The Evolution of Modern Eukaryotic Phytoplankton. *Science, 305*, 354-360

Falkowski, P.G., & Ravenm, J.A. (2007). *Aquatic Photosynthesis: Second Edition*. (2 ed.). Princeton, New Jersey: Princeton University Press

Feldman, G.C., & McClain, C.R. (2012). Ocean Color Chlorophyll (OC) v6, Ocean Color WebOcean Color Chlorophyll (OC) v6, Ocean Color Web. In N. Kuring, S.W. Bailey, B.F. Franz, G. Meister, P.J. Werdell, & R.E. Eplee (Eds.): NASA Goddard Space Flight Center

Fetterer, F., Knowles, K., Meier, W., & Savoie, M. (2002). Sea Ice Index. In. Boulder, Colorado USA: National Snow and Ice Data Center

Field, C.B., Behrenfeld, M.J., Randerson, J.T., & Falkowski, P. (1998). Primary production of the biosphere: Integrating terrestrial and oceanic components. *Science, 281*, 237-240

Finkel, Z.V., Beardall, J., Flynn, K.J., Quigg, A., Rees, T.A.V., & Raven, J.A. (2010). Phytoplankton in a changing world: cell size and elemental stoichiometry. *Journal of Plankton Research, 32*, 119-137

Fogt, R., Bromwich, D., & Hines, K. (2011). Understanding the SAM influence on the South

Pacific ENSO teleconnection. *Climate Dynamics, 36*, 1555-1576

Franks, P.J.S. (2014). Has Sverdrup's critical depth hypothesis been tested? Mixed layers vs. turbulent layers. *ICES Journal of Marine Science: Journal du Conseil*

Fujiwara, A., Hirawake, T., Suzuki, K., Imai, I., & Saitoh, S.I. (2014). Timing of sea ice retreat can alter phytoplankton community structure in the western Arctic Ocean. *Biogeosciences, 11*, 1705-1716

Garcia, C.A.E., Garcia, V.M.T., & McClain, C.R. (2005). Evaluation of SeaWiFS chlorophyll algorithms in the Southwestern Atlantic and Southern Oceans. *Remote Sensing of Environment, 95*, 125-137

Garrison, D.L., Gowing, M.M., Hughes, M.P., Campbell, L., Caron, D.A., Dennett, M.R., Shalapyonok, A., Olson, R.J., Landry, M.R., Brown, S.L., Liu, H.-B., Azam, F., Steward, G.F., Ducklow, H.W., & Smith, D.C. (2000). Microbial food web structure in the Arabian Sea: a US JGOFS study. *Deep Sea Research Part II: Topical Studies in Oceanography, 47*, 1387-1422

Gordon, H.R., Brown, O.B., Evans, R.H., Brown, J.W., Smith, R.C., Baker, K.S., & Clark, D.K. (1988). A Semianalytic Radiance Model of Ocean Color. *Journal of Geophysical Research-Atmospheres, 93*, 10909-10924

Gordon, H.R., & Clark, D.K. (1980). Remote-Sensing Optical-Properties of a Stratified Ocean - an Improved Interpretation. *Applied Optics, 19*, 3428-3430

Gordon, H.R., & Mccluney, W.R. (1975). Estimation of Depth of Sunlight Penetration in Sea for Remote-Sensing. *Applied Optics, 14*, 413-416

Gordon, H.R., & Wang, M.H. (1994). Retrieval of Water-Leaving Radiance and Aerosol Optical-Thickness over the Oceans with Seawifs - a Preliminary Algorithm. *Applied Optics, 33*, 443-452

Graham, R.M., & De Boer, A.M. (2013). The Dynamical Subtropical Front. *Journal of Geophysical Research: Oceans, 118*, 5676-5685

Gregg, W.W., & Casey, N.W. (2007). Modeling coccolithophores in the global oceans. *Deep-Sea Research Part Ii-Topical Studies in Oceanography, 54*, 447-477

Hauck, J., & Völker, C. (2015). Rising atmospheric CO2 leads to large impact of biology on Southern Ocean CO2 uptake via changes of the Revelle factor. *Geophysical Research Letters, 42*, 1459-1464

Hauck, J., Völker, C., Wang, T., Hoppema, M., Losch, M., & Wolf-Gladrow, D.A. (2013). Seasonally different carbon flux changes in the Southern Ocean in response to the southern annular mode. *Global Biogeochemical Cycles, 27*, 1236-1245

Henson, S.A. (2014). Slow science: the value of long ocean biogeochemistry records. *Philosophical Transactions of the Royal Society a-Mathematical Physical and Engineering Sciences, 372*

Henson, S.A., Dunne, J.P., & Sarmiento, J.L. (2009). Decadal variability in North Atlantic phytoplankton blooms. *Journal of Geophysical Research: Oceans, 114*, C04013

Henson, S.A., Sanders, R., Madsen, E., Morris, P.J., Le Moigne, F., & Quartly, G.D. (2011). A

reduced estimate of the strength of the ocean's biological carbon pump. *Geophysical Research Letters, 38*

Henson, S.A., Sarmiento, J.L., Dunne, J.P., Bopp, L., Lima, I., Doney, S.C., John, J., & Beaulieu, C. (2010). Detection of anthropogenic climate change in satellite records of ocean chlorophyll and productivity. *Biogeosciences, 7*, 621-640

Henson, S.A., & Thomas, A.C. (2007). Interannual variability in timing of bloom initiation in the California Current System. *Journal of Geophysical Research: Oceans, 112*, C08007

Hirata, T., Aiken, J., Hardman-Mountford, N., Smyth, T.J., & Barlow, R.G. (2008). An absorption model to determine phytoplankton size classes from satellite ocean colour. *Remote Sensing of Environment, 112*, 3153-3159

Hirata, T., Hardman-Mountford, N.J., Brewin, R.J.W., Aiken, J., Barlow, R., Suzuki, K., Isada, T., Howell, E., Hashioka, T., Noguchi-Aita, M., & Yamanaka, Y. (2011). Synoptic relationships between surface Chlorophyll-a and diagnostic pigments specific to phytoplankton functional types. *Biogeosciences, 8*, 311-327

Hirawake, T., Shinmyo, K., Fujiwara, A., & Saitoh, S. (2012). Satellite remote sensing of primary productivity in the Bering and Chukchi Seas using an absorption-based approach. *Ices Journal of Marine Science, 69*, 1194-1204

Hirawake, T., Takao, S., Horimoto, N., Ishimaru, T., Yamaguchi, Y., & Fukuchi, M. (2011). A phytoplankton absorption-based primary productivity model for remote sensing in the Southern Ocean. *Polar Biology, 34*, 291-302

Hoffmann, L.J., Peeken, I., Lochte, K., Assmy, P., & Veldhuis, M. (2006). Different reactions of Southern Ocean phytoplankton size classes to iron fertilization. *Limnology and Oceanography, 51*, 1217-1229

Holm-Hansen, O., Kahru, M., & Hewes, C.D. (2005). Deep chlorophyll a maxima (DCMs) in pelagic Antarctic waters. II. Relation to bathymetric features and dissolved iron concentrations. *Marine Ecology Progress Series, 297*, 71-81

Huisman, J., Arrayás, M., Ebert, U., & Sommeijer, B. (2002). How do sinking phytoplankton species manage to persist? *The American Naturalist, 159*, 245-254

Hyde, K.J.W., O'Reilly, J.E., & Oviatt, C.A. (2007). Validation of SeaWiFS chlorophyll a in Massachusetts Bay. *Continental Shelf Research, 27*, 1677-1691

Iida, T., Saitoh, S.I., Miyamura, T., Toratani, M., Fukushima, H., & Shiga, N. (2002). Temporal and spatial variability of coccolithophore blooms in the eastern Bering Sea, 1998-2001. *Progress in Oceanography, 55*, 165-175

IOCCG (2006). Remote Sensing of Inherent Optical Properties: Fundamentals, TestsofAlgorithms, and Applications. In Z. Lee (Ed.), *Reports of the International Ocean-Colour Coordinating Group*: IOCCG

IOCCG (2014). Phytoplankton Functional Types from Space. In S. Sathyendranath (Ed.), *Reports of the International Ocean-Colour Coordinating Group*. Dartmouth, Canada

IPCC (2014). Synthesis Report. Contribution of Working Groups I, II and III to the Fifth

Assessment Report of the Intergovernmental Panel on Climate Change. In R.K. Pachauri, & L.A. Meyer (Eds.), *Climate Change 2014* (p. 151). Geneva, Switzerland: IPCC

Ito, A. (2011). A historical meta-analysis of global terrestrial net primary productivity: are estimates converging? *Global Change Biology, 17*, 3161-3175

Johnson, R., Strutton, P.G., Wright, S.W., McMinn, A., & Meiners, K.M. (2013). Three improved satellite chlorophyll algorithms for the Southern Ocean. *Journal of Geophysical Research: Oceans, 118*, 3694-3703

Kahru, M., Brotas, V., Manzano-Sarabia, M., & Mitchell, B.G. (2011). Are phytoplankton blooms occurring earlier in the Arctic? *Global Change Biology, 17*, 1733-1739

Kahru, M., & Mitchell, B.G. (2010). Blending of ocean colour algorithms applied to the Southern Ocean. *Remote Sensing Letters, 1*, 119-124

Kemp, A.E.S., & Villareal, T.A. (2013). High diatom production and export in stratified waters - A potential negative feedback to global warming. *Progress in Oceanography, 119*, 4-23

Kirk, J.T.O. (2011). *Light and Photosynthesis in Aquatic Ecosystems*. (3 ed.). New York: Cambridge University Press

Kooistra, W., Gersonde, R., Medlin, L.K., & Mann, D.G. (2007). The origin and evolution of the diatoms: their adaptation to a planktonic existence. *Evolution of primary producers in the sea*, 207-249

Krasemann, H., Belo Couto, A., Brando, V., Brewin, R.J.W., Brockmann, C., Brotas, V., Doerffer, R., Feng, H., Froiun, R., Gould, R., Grant, M., Groom, S., Hooker, S., Jackson, T., Kahru, M., Kratzer, S., Melin, F., Mitchell, G., Morrison, R., Müller, D., Muller-Karger, F., Sathyendranath, S., Sosik, H., Steinmetz, F., Swinton, J., Valente, A., & Voss, K. (2014). Product Validation and Intercomparison Report In J. Swinton, & S. Sathyendranath (Eds.), *Ocean Colour Climate Change Initiative (OC_CCI) - Phase One*. Plymouth Plymouth Marine Laboratory

Kwok, R., & Comiso, J. (2002). Southern Ocean climate and sea ice anomalies associated with the Southern Oscillation. *Journal of Climate, 15*, 487-501

L'Heureux, M.L., & Thompson, D.W. (2006). Observed relationships between the El Nino-Southern Oscillation and the extratropical zonal-mean circulation. *Journal of Climate, 19*, 276-287

Leblanc, K., Arístegui, J., Armand, L., Assmy, P., Beker, B., Bode, A., Breton, E., Cornet, V., Gibson, J., Gosselin, M.P., Kopczynska, E., Marshall, H., Peloquin, J., Piontkovski, S., Poulton, A.J., Quéguiner, B., Schiebel, R., Shipe, R., Stefels, J., van Leeuwe, M.A., Varela, M., Widdicombe, C., & Yallop, M. (2012). A global diatom database – abundance, biovolume and biomass in the world ocean. *Earth Syst. Sci. Data, 4*, 149-165

Lee, Z., Du, K., Arnone, R., Liew, S., & Penta, B. (2005). Penetration of solar radiation in the upper ocean: A numerical model for oceanic and coastal waters. *Journal of Geophysical Research: Oceans, 110*, C09019

Lee, Z., & Hu, C. (2006). Global distribution of Case-1 waters: An analysis from SeaWiFS measurements. *Remote Sensing of Environment, 101*, 270-276

Lee, Z., Lance, V.P., Shang, S., Vaillancourt, R., Freeman, S., Lubac, B., Hargreaves, B.R., Del Castillo, C., Miller, R., Twardowski, M., & Wei, G. (2011). An assessment of optical properties and primary production derived from remote sensing in the Southern Ocean (SO GasEx). *Journal of Geophysical Research: Oceans, 116*, C00F03

Lee, Z., Lubac, B., Werdell, J., & Arnone, R. (2009). *An Update of the Quasi-An alytical Algorithm*.

Lee, Z., Shang, S., Hu, C., Lewis, M., Arnone, R., Li, Y., & Lubac, B. (2010). Time series of bio-optical properties in a subtropical gyre: Implications for the evaluation of interannual trends of biogeochemical properties. *Journal of Geophysical Research: Oceans, 115*, C09012

Lee, Z., Weidemann, A., Kindle, J., Arnone, R., Carder, K.L., & Davis, C. (2007). Euphotic zone depth: Its derivation and implication to ocean-color remote sensing. *Journal of Geophysical Research: Oceans, 112*, C03009

Lee, Z.P., Carder, K.L., & Arnone, R.A. (2002). Deriving inherent optical properties from water color: a multiband quasi-analytical algorithm for optically deep waters. *Applied Optics, 41*, 5755-5772

Lefebvre, W., Goosse, H., Timmermann, R., & Fichefet, T. (2004). Influence of the Southern Annular Mode on the sea ice–ocean system. *Journal of Geophysical Research: Oceans, 109*, C09005

Lovenduski, N.S. (2007). *Impact of the Southern Annular Mode on Southern Ocean Circulation and Biogeochemistry*. ProQuest

Lovenduski, N.S., & Gruber, N. (2005). Impact of the Southern Annular Mode on Southern Ocean circulation and biology. *Geophysical Research Letters, 32*

Luthi, D., Le Floch, M., Bereiter, B., Blunier, T., Barnola, J.-M., Siegenthaler, U., Raynaud, D., Jouzel, J., Fischer, H., Kawamura, K., & Stocker, T.F. (2008). High-resolution carbon dioxide concentration record 650,000-800,000[thinsp]years before present. *Nature, 453*, 379-382

Maheshwari, M., Singh, R.K., Oza, S.R., & Kumar, R. (2013). An Investigation of the Southern Ocean Surface Temperature Variability Using Long-Term Optimum Interpolation SST Data. *ISRN Oceanography, 2013*, 9

MaierReimer, E., Mikolajewicz, U., & Winguth, A. (1996). Future ocean uptake of CO2: Interaction between ocean circulation and biology. *Climate Dynamics, 12*, 711-721

Maksym, T., Stammerjohn, S.E., Ackley, S., & Massom, R. (2012). Antarctic Sea Ice-A Polar Opposite? *Oceanography, 25*, 140-151

Marrari, M., Hu, C., & Daly, K. (2006). Validation of SeaWiFS chlorophyll a concentrations in the Southern Ocean: A revisit. *Remote Sensing of Environment, 105*, 367-375

Martin, S. (2004). *An Introduction to Ocean Remote Sensing*. Cambridge: Cambridge University Press

Mélin, F. (2011). Comparison of SeaWiFS and MODIS time series of inherent optical properties for the Adriatic Sea. *Ocean Sci., 7*, 351-361

Milutinovic, S., & Bertino, L. (2011). Assessment and propagation of uncertainties in input terms through an ocean-color-based model of primary productivity. *Remote Sensing of Environment, 115*, 1906-1917

Mo, K.C. (2000). Relationships between Low-Frequency Variability in the Southern Hemisphere and Sea Surface Temperature Anomalies. *Journal of Climate, 13*, 3599-3610

Mobley, C.D. (1994). *Light and Water: Radiative Transfer in Natural Waters*. Academic Press

Montegut, C.D., Madec, G., Fischer, A.S., Lazar, A., & Iudicone, D. (2004). Mixed layer depth over the global ocean: An examination of profile data and a profile-based climatology. *Journal of Geophysical Research-Oceans, 109*

Montes-Hugo, M.A., Vernet, M., Martinson, D., Smith, R., & Iannuzzi, R. (2008). Variability on phytoplankton size structure in the western Antarctic Peninsula (1997–2006). *Deep Sea Research Part II: Topical Studies in Oceanography, 55*, 2106-2117

Morel, A. (1974). Optical properties of pure water and pure sea water. In N.G. Jerlov, & E.S. Nielsen (Eds.), *Optical Aspects of Oceanography* (p. 24). New York: Academic

Morel, A., Antoine, D., & Gentili, B. (2002). Bidirectional reflectance of oceanic waters: accounting for Raman emission and varying particle scattering phase function. *Applied Optics, 41*, 6289-6306

Morel, A., & Berthon, J.-F. (1989). Surface pigments, algal biomass profiles, and potential production of the euphotic layer: Relationships reinvestigated in view of remote-sensing applications. *Limnology and Oceanography, 34*, 1545-1562

Morel, A., Claustre, H., Antoine, D., & Gentili, B. (2007). Natural variability of bio-optical properties in Case 1 waters: attenuation and reflectance within the visible and near-UV spectral domains, as observed in South Pacific and Mediterranean waters. *Biogeosciences, 4*, 913-925

Morel, A., & Gentili, B. (2004). Radiation transport within oceanic (case 1) water. *Journal of Geophysical Research: Oceans, 109*, C06008

Morel, A., & Maritorena, S. (2001). Bio-optical properties of oceanic waters: A reappraisal. *Journal of Geophysical Research-Oceans, 106*, 7163-7180

Nair, A., Sathyendranath, S., Platt, T., Morales, J., Stuart, V., Forget, M.H., Devred, E., & Bouman, H. (2008). Remote sensing of phytoplankton functional types. *Remote Sensing of Environment, 112*, 3366-3375

NSDC (2015). Cryosphere Glossary. In, *https://nsidc.org/cryosphere/glossary/term/seasonal-ice-zone*

O'Reilly, J.E., Maritorena, S., Siegel, D., O'Brien, M., Toole, D., Mitchell, B.G., Kahru, M., Chavez, F., Strutton, P., Cota, G., Hooker, S., McClain, C., Carder, K., Muller-Karger, F., Harding, L., Magnuson, A., Phinney, D., Moore, G., Aiken, J., Arrigo, K., Letelier, R., & Culver, M. (2000). Ocean color chlorophyll a algorithms for SeaWiFS, OC2, and OC4:

Version 4. In E.R. Firestone, & S.B. Hooker (Eds.), *SeaWiFS Postlaunch Calibration and Validation Analyses, Part 3*. Greenbelt, Maryland: NASA Goddard Space Flight Center

Peloquin, J., Swan, C., Gruber, N., Vogt, M., Claustre, H., Ras, J., Uitz, J., Barlow, R., Behrenfeld, M., Bidigare, R., Dierssen, H., Ditullio, G., Fernandez, E., Gallienne, C., Gibb, S., Goericke, R., Harding, L., Head, E., Holligan, P., Hooker, S., Karl, D., Landry, M., Letelier, R., Llewellyn, C.A., Lomas, M., Lucas, M., Mannino, A., Marty, J.C., Mitchell, B.G., Muller-Karger, F., Nelson, N., O'Brien, C., Prezelin, B., Repeta, D., Jr. Smith, W.O., Smythe-Wright, D., Stumpf, R., Subramaniam, A., Suzuki, K., Trees, C., Vernet, M., Wasmund, N., & Wright, S. (2013). The MAREDAT global database of high performance liquid chromatography marine pigment measurements. *Earth Syst. Sci. Data, 5*, 109-123

Penland, C., Sun, D.-Z., Capotondi, A., & Vimont, D.J. (2013). A Brief Introduction to El Niño and La Niña. *Climate Dynamics: Why Does Climate Vary?* (pp. 53-64): American Geophysical Union

Planquette, H., Statham, P.J., Fones, G.R., Charette, M.A., Moore, C.M., Salter, I., Nedelec, F.H., Taylor, S.L., French, M., Baker, A.R., Mahowald, N., & Jickells, T.D. (2007). Dissolved iron in the vicinity of the Crozet Islands, Southern Ocean. *Deep-Sea Research Part Ii-Topical Studies in Oceanography, 54*, 1999-2019

Pohl, B., Fauchereau, N., Reason, C.J.C., & Rouault, M. (2010). Relationships between the Antarctic Oscillation, the Madden–Julian Oscillation, and ENSO, and Consequences for Rainfall Analysis. *Journal of Climate, 23*, 238-254

Pollard, R.T., Lucas, M.I., & Read, J.F. (2002). Physical controls on biogeochemical zonation in the Southern Ocean. *Deep Sea Research Part II: Topical Studies in Oceanography, 49*, 3289-3305

Pope, R.M., & Fry, E.S. (1997). Absorption spectrum (380?700 nm) of pure water. II. Integrating cavity measurements. *Applied Optics, 36*, 8710-8723

Racault, M.F., Le Quere, C., Buitenhuis, E., Sathyendranath, S., & Platt, T. (2012). Phytoplankton phenology in the global ocean. *Ecological Indicators, 14*, 152-163

Racault, M.F., Sathyendranath, S., & Platt, T. (2014). Impact of missing data on the estimation of ecological indicators from satellite ocean-colour time-series. *Remote Sensing of Environment, 152*, 15-28

Reynolds, R.A., Stramski, D., & Mitchell, B.G. (2001). A chlorophyll-dependent semianalytical reflectance model derived from field measurements of absorption and backscattering coefficients within the Southern Ocean. *Journal of Geophysical Research: Oceans, 106*, 7125-7138

Rintoul, S. (2010). Antarctic Circumpolar Current. *Ocean Currents: A Derivative of the Encyclopedia of Ocean Sciences*, 196

Rintoul, S.R., & Garabato, A.C.N. (2013). Dynamics of the Southern Ocean circulation. In G. Siedler, S. Griffies, J. Gould, & J. Church (Eds.), *Ocean Circulation and Climate: A 21st century perspective* (pp. 471–492): Academic Pres

Rintoul, S.R., Hughes, C., & Olbers, D. (1999). The Antarctic Circumpolar Current System.

Oceans and Climate, G. Siedler and J. Church,(eds.), Academic Press (submitted)

Robinson, I.S. (2010). *Discovering the Ocean from Space*. (1 ed.). Springer-Verlag Berlin Heidelberg

Rousseaux, C.S., & Gregg, W.W. (2014). Interannual Variation in Phytoplankton Primary Production at A Global Scale. *Remote Sensing, 6*, 1-19

Saba, V.S., Friedrichs, M.A.M., Antoine, D., Armstrong, R.A., Asanuma, I., Behrenfeld, M.J., Ciotti, A.M., Dowell, M., Hoepffner, N., Hyde, K.J.W., Ishizaka, J., Kameda, T., Marra, J., Melin, F., Morel, A., O'Reilly, J., Scardi, M., Smith, W.O., Smyth, T.J., Tang, S., Uitz, J., Waters, K., & Westberry, T.K. (2011). An evaluation of ocean color model estimates of marine primary productivity in coastal and pelagic regions across the globe. *Biogeosciences, 8*, 489-503

Sabine, C.L., Feely, R.A., Gruber, N., Key, R.M., Lee, K., Bullister, J.L., Wanninkhof, R., Wong, C.S., Wallace, D.W.R., Tilbrook, B., Millero, F.J., Peng, T.H., Kozyr, A., Ono, T., & Rios, A.F. (2004). The oceanic sink for anthropogenic CO2. *Science, 305*, 367-371

Sadeghi, A., Dinter, T., Vountas, M., Taylor, B.B., Altenburg-Soppa, M., Peeken, I., & Bracher, A. (2012). Improvement to the PhytoDOAS method for identification of coccolithophores using hyper-spectral satellite data. *Ocean Science, 8*, 1055-1070

Sallée, J.B., Speer, K., & Morrow, R. (2008). Response of the Antarctic Circumpolar Current to Atmospheric Variability. *Journal of Climate, 21*, 3020-3039

Sallee, J.B., Speer, K.G., & Rintoul, S.R. (2010). Zonally asymmetric response of the Southern Ocean mixed-layer depth to the Southern Annular Mode. *Nature Geoscience, 3*, 273-279

Sarmiento, J.L., Gruber, N., Brzezinski, M.A., & Dunne, J.P. (2004). High-latitude controls of thermocline nutrients and low latitude biological productivity. *Nature, 427*, 56-60

Schmittner, A., Chiang, J.C.H., & Hemming, S.R. (2013). Introduction: The Ocean's Meridional Overturning Circulation. *Ocean Circulation: Mechanisms and Impacts—Past and Future Changes of Meridional Overturning* (pp. 1-4): American Geophysical Union

Schwartz, M.D. (2013). Introduction. In M.D. Schwartz (Ed.), *Phenology: An Integrative Environmental Science* (pp. 1-5): Springer Netherlands

Shang, S., Dong, Q., Lee, Z., Li, Y., Xie, Y., & Behrenfeld, M. (2011a). MODIS observed phytoplankton dynamics in the Taiwan Strait: an absorption-based analysis. *Biogeosciences, 8*, 841-850

Shang, S., Lee, Z., & Wei, G. (2011b). Characterization of MODIS-derived euphotic zone depth: Results for the China Sea. *Remote Sensing of Environment, 115*, 180-186

Siegel, D.A., Buesseler, K.O., Doney, S.C., Sailley, S.F., Behrenfeld, M.J., & Boyd, P.W. (2014). Global assessment of ocean carbon export by combining satellite observations and food-web models. *Global Biogeochemical Cycles, 28*, 181-196

Siegel, D.A., Doney, S.C., & Yoder, J.A. (2002). The North Atlantic spring phytoplankton bloom and Sverdrup's critical depth hypothesis. *Science, 296*, 730-733

Smetacek, V. (1999). Diatoms and the ocean carbon cycle. *Protist, 150*, 25-32

Smetacek, V., Assmy, P., & Henjes, J. (2004). The role of grazing in structuring Southern Ocean pelagic ecosystems and biogeochemical cycles. *Antarctic Science, 16*, 541-558

Smetacek, V., Klaas, C., Strass, V.H., Assmy, P., Montresor, M., Cisewski, B., Savoye, N., Webb, A., d'Ovidio, F., Arrieta, J.M., Bathmann, U., Bellerby, R., Berg, G.M., Croot, P., Gonzalez, S., Henjes, J., Herndl, G.J., Hoffmann, L.J., Leach, H., Losch, M., Mills, M.M., Neill, C., Peeken, I., Rottgers, R., Sachs, O., Sauter, E., Schmidt, M.M., Schwarz, J., Terbruggen, A., & Wolf-Gladrow, D. (2012). Deep carbon export from a Southern Ocean iron-fertilized diatom bloom. *Nature, 487*, 313-319

Smetacek, V.S. (1985). Role of Sinking in Diatom Life-History Cycles - Ecological, Evolutionary and Geological Significance. *Marine Biology, 84*, 239-251

Smith, R.C., Martinson, D.G., Stammerjohn, S.E., Iannuzzi, R.A., & Ireson, K. (2008). Bellingshausen and western Antarctic Peninsula region: Pigment biomass and sea-ice spatial/temporal distributions and interannual variabilty. *Deep Sea Research Part II: Topical Studies in Oceanography, 55*, 1949-1963

Smith, W.O., Sedwick, P.N., Arrigo, K.R., Ainley, D.G., & Orsi, A.H. (2012). The Ross Sea in a Sea of Change. *Oceanography, 25*, 90-103

Sokolov, S., & Rintoul, S.R. (2007). On the relationship between fronts of the Antarctic Circumpolar Current and surface chlorophyll concentrations in the Southern Ocean. *Journal of Geophysical Research-Oceans, 112*

Soppa, M.A., Dinter, T., Taylor, B.B., & Bracher, A. (2013). Satellite derived euphotic depth in the Southern Ocean: Implications for primary production modelling. *Remote Sensing of Environment, 137*, 198-211

Soppa, M.A., Hirata, T., Silva, B., Dinter, T., Peeken, I., Wiegmann, S., & Bracher, A. (2014). Global Retrieval of Diatom Abundance Based on Phytoplankton Pigments and Satellite Data. *Remote Sensing, 6*, 10089-10106

Sournia, A., Chretiennotdinet, M.J., & Ricard, M. (1991). Marine-Phytoplankton - How Many Species in the World Ocean. *Journal of Plankton Research, 13*, 1093-1099

Steinmetz, F., Deschamps, P.Y., & Ramon, D. (2011). Atmospheric correction in presence of sun glint: application to MERIS. *Optics Express, 19*, 9783-9800

Sverdrup, H.U. (1953). On Conditions for the Vernal Blooming of Phytoplankton. *Journal du Conseil, 18*, 287-295

Szeto, M., Werdell, P.J., Moore, T.S., & Campbell, J.W. (2011). Are the world's oceans optically different? *Journal of Geophysical Research: Oceans, 116*, C00H04

Tagliabue, A., Sallee, J.B., Bowie, A.R., Levy, M., Swart, S., & Boyd, P.W. (2014). Surface-water iron supplies in the Southern Ocean sustained by deep winter mixing. *Nature Geoscience, 7*, 314-320

Takahashi, T., Sutherland, S.C., Wanninkhof, R., Sweeney, C., Feely, R.A., Chipman, D.W., Hales, B., Friederich, G., Chavez, F., Sabine, C., Watson, A., Bakker, D.C.E., Schuster, U.,

Metzl, N., Yoshikawa-Inoue, H., Ishii, M., Midorikawa, T., Nojiri, Y., Kortzinger, A., Steinhoff, T., Hoppema, M., Olafsson, J., Arnarson, T.S., Tilbrook, B., Johannessen, T., Olsen, A., Bellerby, R., Wong, C.S., Delille, B., Bates, N.R., & de Baar, H.J.W. (2009). Climatological mean and decadal change in surface ocean pCO(2), and net sea-air CO2 flux over the global oceans (vol 56, pg 554, 2009). *Deep-Sea Research Part I-Oceanographic Research Papers, 56*, 2075-2076

Takahashi, T., Sweeney, C., Hales, B., Chipman, D.W., Newberger, T., Goddard, J.G., Iannuzzi, R.A., & Sutherland, S.C. (2012). The Changing Carbon Cycle in the Southern Ocean. *Oceanography, 25*, 26-37

Talley, L.D. (2013). Closure of the Global Overturning Circulation Through the Indian, Pacific, and Southern Oceans: Schematics and Transports. *Oceanography, 26*, 80-97

Tassan, S., & Ferrari, G.M. (1995). An alternative approach to absorption measurements of aquatic particles retained on filters. *Limnology and Oceanography, 40*, 1358-1368

Taylor, B.B., Torrecilla, E., Bernhardt, A., Taylor, M.H., Peeken, I., Röttgers, R., Piera, J., & Bracher, A. (2011). Bio-optical provinces in the eastern Atlantic Ocean and their biogeographical relevance. *Biogeosciences, 8*, 3609-3629

Taylor, M.H., Losch, M., & Bracher, A. (2013). On the drivers of phytoplankton blooms in the Antarctic marginal ice zone: A modeling approach. *Journal of Geophysical Research: Oceans, 118*, 63-75

Thomalla, S.J., Fauchereau, N., Swart, S., & Monteiro, P.M.S. (2011). Regional scale characteristics of the seasonal cycle of chlorophyll in the Southern Ocean. *Biogeosciences, 8*, 2849-2866

Thompson, D.W.J., Solomon, S., Kushner, P.J., England, M.H., Grise, K.M., & Karoly, D.J. (2011). Signatures of the Antarctic ozone hole in Southern Hemisphere surface climate change. *Nature Geoscience, 4*, 741-749

Uitz, J., Claustre, H., Gentili, B., & Stramski, D. (2009a). Phytoplankton Class-Specific Primary Production in the World's Oceans: An Estimate Based on Seawifs Time Series (1998-2007). *Phycologia, 48*, 134-134

Uitz, J., Claustre, H., Gentili, B., & Stramski, D. (2010). Phytoplankton class-specific primary production in the world's oceans: Seasonal and interannual variability from satellite observations. *Global Biogeochemical Cycles, 24*

Uitz, J., Claustre, H., Griffiths, F.B., Ras, J., Garcia, N., & Sandronie, V. (2009b). A phytoplankton class-specific primary production model applied to the Kerguelen Islands region (Southern Ocean). *Deep-Sea Research Part I-Oceanographic Research Papers, 56*, 541-560

Uitz, J., Claustre, H., Morel, A., & Hooker, S.B. (2006). Vertical distribution of phytoplankton communities in open ocean: An assessment based on surface chlorophyll. *Journal of Geophysical Research-Oceans, 111*

Uitz, J., Stramski, D., Gentili, B., D'Ortenzio, F., & Claustre, H. (2012). Estimates of phytoplankton class-specific and total primary production in the Mediterranean Sea from

satellite ocean color observations. *Global Biogeochemical Cycles, 26*

Vidussi, F., Claustre, H., Manca, B.B., Luchetta, A., & Marty, J.C. (2001). Phytoplankton pigment distribution in relation to upper thermocline circulation in the eastern Mediterranean Sea during winter. *Journal of Geophysical Research-Oceans, 106*, 19939-19956

Vountas, M., Dinter, T., Bracher, A., Burrows, J.P., & Sierk, B. (2007). Spectral studies of ocean water with space-borne sensor SCIAMACHY using differential optical absorption Spectroscopy (DOAS). *Ocean Science, 3*, 429-440

Wang, M., & Shi, W. (2009). Detection of Ice and Mixed Ice-Water Pixels for MODIS Ocean Color Data Processing. *Geoscience and Remote Sensing, IEEE Transactions on, 47*, 2510-2518

Werdell, P.J., Bailey, S.W., Fargion, G.S., Pietras, C., Knobelspiesse, K.D., Feldman, G.C., & McClain, C.R. (2003). Unique data repository facilitates ocean color satellite validation. *EOS Trans. AGU, 84*, 377

Westberry, T., Behrenfeld, M.J., Siegel, D.A., & Boss, E. (2008). Carbon-based primary productivity modeling with vertically resolved photoacclimation. *Global Biogeochemical Cycles, 22*, GB2024

Willmott, C.J., & Matsuura, K. (2005). Advantages of the mean absolute error (MAE) over the root mean square error (RMSE) in assessing average model performance. *Climate Research, 30*, 79-82

Wolter, K., & Timlin, M.S. (1993). Monitoring ENSO in COADS with a seasonally adjusted principal component index. In, *Proc. of the 17th Climate Diagnostics Workshop* (pp. 52-57)

Wright, S.W., & van den Enden, R.L. (2000). Phytoplankton community structure and stocks in the East Antarctic marginal ice zone (BROKE survey, January-March 1996) determined by CHEMTAX analysis of HPLC pigment signatures. *Deep-Sea Research Part Ii-Topical Studies in Oceanography, 47*, 2363-2400

Yao, X., & Schlitzer, R. (2013). Assimilating water column and satellite data for marine export production estimation. *Geoscientific Model Development, 6*, 1575-1590

Yeo, S.-R., & Kim, K.-Y. (2015). Decadal changes in the Southern Hemisphere sea surface temperature in association with El Niño–Southern Oscillation and Southern Annular Mode. *Climate Dynamics*, 1-16

Yuan, X. (2004). ENSO-related impacts on Antarctic sea ice: a synthesis of phenomenon and mechanisms. *Antarctic Science, 16*, 415-425

Zaneveld, J.R.V. (1995). A Theoretical Derivation of the Dependence of the Remotely-Sensed Reflectance of the Ocean on the Inherent Optical-Properties. *Journal of Geophysical Research-Oceans, 100*, 13135-13142

Zibordi, G., Melin, F., & Berthon, J.F. (2006). Comparison of SeaWiFS, MODIS and MERIS radiometric products at a coastal site. *Geophysical Research Letters, 33*